Universitat Politècnica de Catalunya
Applied Physics Department

Modelling the dynamics of large scale shoreline sand waves

PhD thesis presented by

Niels van den Berg

for the degree of DOCTOR

Director:

Prof. Albert Falqués Serra
Universitat Politècnica de Catalunya

Co-director:

Dr. Francesca Ribas Prats
Universitat Politècnica de Catalunya

Barcelona, March 2012

Contents

Abstract

Shoreline sand waves are shoreline undulations with a length scale of several kilometres and a time scale of years to decades. They occur on many coasts, migrating in the direction of the dominant littoral drift and they introduce a variability into the shoreline position that can be greater than the long term coastal trend. The objective of this thesis is to provide more insight into the formation and dynamics of shoreline sand waves and, in particular, to explore the role of the so called high angle wave instability. Previous studies showed that the shoreline can be unstable under very oblique wave incidence. This high angle wave instability develops due to the feedback of shoreline changes and the associated changes in the bathymetry into the wave field. Wave propagation over this perturbed bathymetry leads to specific gradients in the alongshore transport that can cause the growth and migration of shoreline sand waves.

In this thesis a quasi 2D non-linear morphodynamical model is improved and used to explore high angle wave instability and predict the formation and evolution of shoreline sand waves. The model assumes that the large scale and long term shoreline dynamics is controlled by the wave driven alongshore transport so that the details of the surfzone morphodynamics are not resolved. It overcomes some of the limitations of previous modelling studies on high angle wave instability. The wave field is computed with a simple wave module over the evolving bathymetry and an empirical formula is used to compute the alongshore transport. Cross-shore dynamics is described in a parameterized way and the model is capable of describing shoreline perturbations with a finite and dynamic cross-shore extent.

The conditions under which shoreline instability can lead to the formation of shoreline sand waves are refined. Generic simulations with constant wave conditions and random initial perturbations show that the shoreline becomes unstable when the wave incidence angle at the depth of closure (i.e., the most offshore extent of the shoreline perturbations) is larger than a critical angle of about 42° and shoreline sand waves develop in unison. The cross-shore dynamics plays an essential role because it determines the offshore extent of the shoreline perturbations. Using default model parameters, wave conditions and cross-shore profile, the sand waves develop with wavelengths between 2 and 5 km, the time scale for their formation is between 5 and 10 years and they migrate downdrift at about 0.5 km/yr. Simulations with a localized large scale perturbation trigger the formation of a downdrift sand wave train. Larger wave obliquity, higher waves and shorter wave periods strengthen the shoreline instability. A more realistic wave climate, with alternating high and low angle wave incidence reduces the potential for shoreline instability. A percentage of about 80% of high angle waves is required for sand wave formation. It is demonstrated that the range of low wave angles that can occur on

a coast is larger than the range of high wave angles, and that the stabilizing effect produced by low angle waves (causing diffusion) is bigger than the destabilizing effect produced by high angle waves (causing growth and migration). Even if high angle waves are not dominant, the instability mechanism might still play a role in the persistence and downdrift migration of large scale shoreline perturbations. The model results are in qualitative agreement with observations of shoreline sand waves.

The quasi 2D approach provides new insight into the physical mechanisms behind high angle wave instability and the occurrence of a minimal and optimal length scale for sand wave formation. Essential physical processes are wave energy dispersion due to wave refraction, wave energy focusing near the crest of a sand wave and the monotonic decrease of the gradients in alongshore transport for increasing length scales.

RESUM

Les ones de sorra a la línia de costa són ondulacions de la línia de costa amb una escala espacial de kilòmetres i una escala temporal d'anys a dècades. Ocorren a moltes costes, migren en la direcció del transport litoral dominant i introdueixen una variabilitat a la línia de costa que pot ser major que la seva tendència a llarg termini. L'objectiu d'aquesta tesi és estudiar amb més profunditat la formació i la dinàmica de les ones de sorra i, més concretament, explorar el rol de l'anomenada inestabilitat d'angle gran d'onades. Estudis previs van demostrar que la línia de costa pot ser inestable en cas d'onades obliqües que incideixen amb un angle gran. Aquesta inestabilitat d'angle gran es produeix degut a la retroalimentació entre els canvis a la línia de costa (i els que conseqüentment ocorren a la batimetria) i els canvis al camp d'onades. La propagació de les onades sobre la batimetria pertorbada crea gradients del transport de sediment longitudinal que causen el creixement i la migració de les ones de sorra.

En aquesta tesi s'ha millorat un model morfodinàmic quasi 2D i no lineal per usar-lo per explorar la inestabilitat d'angle gran i predir la formació i evolució de les ones de sorra. El model assumeix que la dinàmica a gran escala i llarg termini està dominada pel transport de sediment longitudinal produït per les onades de manera que els detalls de la morfodinàmica de la zona de rompents no es descriuen. S'han superat algunes de les limitacions dels estudis anteriors de modelat de la inestabilitat d'angle gran. El camp d'onades es calcula amb un mòdul senzill de propagació d'onades sobre la batimetria canviant i el transport longitudinal s'estima usant una fórmula empírica. La dinàmica transversal es parametritza i el model pot descriure pertorbacions de la línia de costa amb una extensió transversal finita i dinàmica.

S'han refinat les condicions sota les quals la inestabilitat d'angle gran produeix la formació d'ones de sorra. Les simulacions genèriques amb condicions constants d'onades i pertorbacions inicials aleatòries mostren que la línia de costa esdevé inestable quan l'angle d'incidència a la profunditat de tancament és major que un angle crític d'uns 42° i les ones de sorra es desenvolupen a l'unísson. La dinàmica transversal té un rol essencial al determinar l'extensió transversal de les pertorbacions. Usant els valors per defecte dels paràmetres del model, les ones de sorra tenen espaiats d'entre 2 i 5 km, escales temporals de creixement d'entre 5 i 10 anys, i migren en la direcció del transport a uns 0.5 km/any. Les simulacions també mostren que una pertorbació inicial localitzada desencadena la formació d'un tren d'ones de sorra. Com més obliqües i grans són les onades i com menor és el seu període major és la inestabilitat. Un clima d'onatge més realista, alternant onades d'angle d'incidència gran i petit, redueix el potencial de la inestabilitat d'angle gran. Calen almenys un 80% d'onades d'angle gran perquè es formin ones de sorra. El rang d'onades d'angle petit que poden succeir en una costa és major que el d'onades

d'angle gran, i l'efecte estabilitzador de les onades d'angle petit (que produeix difusió) és més important que l'efecte desestabilitzador de les onades d'angle gran (que produeix creixement i migració). Fins i tot si les onades d'angle gran no dominen, el mecanisme d'inestabilitat pot tenir un paper important en la persistència i migració de pertorbacions a gran escala de la línia de costa. Els resultats del model s'assemblen qualitativament a les observacions d'ones de sorra.

L'enfocament quasi 2D permet estudiar més detalls del mecanisme físic que hi ha darrere de la inestabilitat d'angle gran i del fet que existeixin longituds d'ona mínima i òptima per la formació d'ones de sorra. Els processos físics essencials són la dispersió de l'energia de l'onatge degut a la refracció, la concentració d'energia de les onades a les crestes de les ones de sorra i el decreixement monòton del transport litoral quan augmenta l'escala espacial.

Chapter 1

Introduction

1.1 Motivation

Sandy shorelines are rarely smooth and alongshore undulations are episodically or persistently found on many coasts. These undulations occur at different spatial and temporal scales. Beach cusps are relatively short features O(10^1 m), which occur at short time scales (hours-days) and they are related to swash zone processes. Mega cusps have larger length scales O(10^2 m) and are commonly related to rhythmic nearshore bar patterns and rip channels with time scales of days to months (Short, 1999). Figure 1.1 shows an example of rhythmic oblique bars with the corresponding mega cusps on the shoreline of Silt Island in Germany. The formation and dynamics of short to intermediate scale rhythmic patterns have been explained as a self-organized behavior of the morphodynamic system (Coco & Murray, 2007).

In this study we will focus on shoreline undulations at a length scale of several kilometres O(10^3 m) and a time scale of years to decades. These large scale undulations have been observed on various sandy coasts around the world (Bruun, 1954; Verhagen, 1989; Thevenot & Kraus, 1995; Guillen *et al.*, 1999; Gravens, 1999; Ruessink & Jeuken, 2002; Davidson-Arnott & van Heyningen, 2003; Kaergaard *et al.*, 2011; Ryabchuk *et al.*, 2011). Here they will be referred to as large scale shoreline sand waves or simply shoreline sand waves. Shoreline sand waves have cross-shore amplitudes of tens to hundreds of meters and on most coasts they migrate in the downdrift direction, with a celerity of the order of hundreds of meters per year. In general, the sand waves maintain their volume and shape while migrating or they grow slowly in amplitude and wavelength. On some coasts they can be clearly seen on aerial or satellite images and on other coast they are subtle features which can be identified by periodic accretion or erosion of the shoreline. Figure 1.1 shows an example of shoreline sand waves with a wavelength of about 5 km and amplitude of about 200 m on the coast of Namibia.

The variability of the shoreline due to the migrating sand waves can be greater than the long term coastal trend and can therefore be of great importance for coastal managers and engineers. Alongshore variations in the shoreline position imply erosional stretches (hotspots) and the resulting decreased beach width increases dune vulnerability (Ruessink & Jeuken, 2002) and reduces the recreational area. Shoreline sand waves have been observed to traverse groin fields (Verhagen, 1989) and their downdrift migration introduces an additional volume to the net alongshore sediment transport. This natural variability of the shoreline should be taken into account in nourishment planning (Stive *et al.*, 2002) and it remains unclear if human intervention in the coastal system could lead to unforeseen interactions with the sand wave dynamics. This leads to the following general research questions. *Due to what mechanism and under what conditions do shoreline sand waves form and what processes control their dynamics?*

In some studies it has been suggested that shoreline sand waves are related to alongshore non-uniformity in the nearshore bar system (Bruun, 1954; Guillen *et al.*, 1999) but in general they are believed to be unrelated to surfzone dynamics because they occur at a greater spatial and temporal scale. In several studies it was reported that the occurrence of shoreline sand waves can be related to intermittent sediment input, e.g., the discharge of river sediments (Inman, 1987), artificial injection of a large quantity of sand (Grove *et al.*, 1987), the welding of an ebb-tidal shoal due to periodic inlet opening (Thevenot & Kraus, 1995) and the welding of the inner bar to the beach (Davidson-Arnott & van Heyningen, 2003). However, even if the occurrence of shoreline sand waves is related to a site specific intermittent sediment input, their dynamics remain unexplained.

The next section gives an introduction to shoreline modelling. After this we will discuss the so called 'high angle wave instability' as a possible mechanism for sand wave formation and in the last section we will formulate the specific research questions and explain the structure of this dissertation.

Figure 1.1: Rhythmic oblique bars with the corresponding mega cusps on the shoreline of Silt Island in Germany. The spacing of the undulations is between $200 - 400$ m (Yoyoki *et al.*, 2002).

Figure 1.2: Large scale shoreline sand waves on the coast of Namibia in Conception Bay. Notice that the length scale of the undulations is much bigger than the width of the surfzone. The horizontal line indicates 5 km and the north is in the right of the image (source: Google Earth).

1.2 Shoreline modelling

The increasing understanding of nearshore dynamics has led to the development of detailed process-based models. These models however still have a low skill in predicting shoreline dynamics (Capobianco *et al.*, 2002). Furthermore, they require detailed field data for calibration and they are computationally demanding. Therefore, simple one-line shoreline change models are commonly used for long term and large scale simulations. These models are based on the assumption that shoreline changes at this scale are caused by gradients in the wave driven alongshore transport and that the detailed surfzone dynamics can be neglected (Larson & Kraus, 1991; Komar, 1998; Dean, 2002). In this approach it is assumed that the cross-shore profile attains an equilibrium shape and, by applying sediment conservation in each cross-shore section, gradients in alongshore transport lead to a shift of the whole profile from the shoreline up to the depth of closure. Shoreline retreat results from a positive gradient and its advance results from a negative gradient:

$$\frac{\partial x_s}{\partial t} = -\frac{1}{D_c}\frac{\partial Q}{\partial y}, \tag{1.1}$$

where the y axis corresponds to the initially rectilinear shoreline, Q is the total sediment transport rate ($\mathrm{m}^3/\mathrm{s}^{-1}$) in the y direction, t is time, $x_s(y,t)$ is the shoreline position and D_c is the depth of closure. Q is commonly computed with the empirical CERC formula, which relates the alongshore transport rate with the root mean square wave height at breaking, H_b, and the angle between the wave fronts at breaking and the shoreline orientation, $\alpha_b = \theta_b - \phi$:

$$Q = K_1 H_b^{5/2} \sin(2\alpha_b), \tag{1.2}$$

where K_1 is an empirical parameter which depends mainly on the sediment grain size (Komar, 1998). By assuming that the changes in the shoreline position are small, the angle ϕ can be approximated by $\partial x_s/\partial y$ and the following equation can be derived by linearlisation (Falqués, 2003):

$$\frac{\partial x_s}{\partial t} = \epsilon \frac{\partial^2 x_s}{\partial y^2}. \tag{1.3}$$

This is a diffusion equation for the shoreline position, which was first presented by Pelnard-Considère (1956). The diffusivity coefficient in this equation is given by:

$$\epsilon = -\frac{1}{D_c}\frac{\partial Q}{\partial \phi}, \tag{1.4}$$

Traditional analytical one-line shoreline models assume that θ_b and H_b are constant along a perturbed coastline, i.e. refraction and shoaling take place over a rectilinear and unperturbed bathymetry. This means that θ_b and H_b are not a function of ϕ and the diffusivity coefficient now becomes (Falqués, 2003):

$$\epsilon_{clas} = \frac{2K_1}{D_c} H_b^{5/2} \cos(2\theta_b). \tag{1.5}$$

This diffusivity coefficient is always greater than zero and therefore the traditional one-line models always predict a stable shoreline and the diffusion of shoreline undulations.

Downdrift migration is sometimes described by extending the diffusion equation with an empirical advection term (Larson & Kraus, 1991; Thevenot & Kraus, 1995; Dean, 2002),

$$\frac{\partial x_s}{\partial t} + V\frac{\partial x_s}{\partial y} = \epsilon\frac{\partial^2 x_s}{\partial y^2}, \tag{1.6}$$

where the migration speed, V, is an empirical constant.

However, a perturbation of a rectilinear shoreline will be associated to a perturbation of the bathymetry up to a certain water depth. Wave refraction over this perturbed bathymetry will lead to lower wave incidence angles at breaking. Dean (2002) showed that this effect of wave refraction on shoreline diffusivity can be approximated analytically and that this can reduce the diffusivity significantly. A similar correction for wave refraction over curvilinear contour lines was included by Thevenot & Kraus (1995) in a numerical model. They found that including the feedback of the shoreline into the wave field through the contour correction reduced the diffusion rate of shoreline sand waves and led to a slight asymmetry in the sand wave shape. Nevertheless, these one-line shoreline change models are not capable of predicting the growth or persistence of shoreline sand waves and do not provide a physical mechanism for their downdrift migration. Inman (1987) described in a conceptual way how accretion/erosion waves propagate along a coast. They explained that an initial bump on a coastline leads to refraction and diffraction which locally modifies the alongshore transport. Wave convergence at the bump leads to a decreasing alongshore transport downdrift of the crest, causing deposition and downdrift migration. Further downdrift, the alongshore transport increases and an erosion wave develops. However, to the authors knowledge, this concept has never been implemented in a modelling study.

1.3 High angle wave instability

1.3.1 Theory and physical mechanism

Zenkovitch (1959) studied the formation of cuspate spits on lagoon shores and argued that their formation is related to the high angle wave incidence on these shores. He stated that for a certain wave incidence angle, the alongshore transport is maximum and that under these conditions an initially straight shoreline could be unstable. Due to this maximum of the transport an initial irregularity on the shoreline can lead to a decrease of the alongshore transport, leading to deposition and growth of the perturbation. It was argued that this could lead to the formation of cuspate spits growing in downdrift direction, parallel to the maximizing wave angle.

Looking at equation (1.2) it can be seen that a maximum in Q occurs for $\alpha_b = 45°$. Grijm (1960) explored the effect of this maximizing angle for alongshore transport on the shoreline shape using a mathematical approach. Such large wave angles are however unlikely at breaking and the possibility for shoreline instability has for long been disregarded. Wang & LeMehaute (1980) were the first to demonstrate, in the context

of shoreline modelling, that a shoreline can potentially be unstable for high incidence angles at deep water, while the incidence angles at breaking are relatively small. In their approach Q is again a function of θ_b and H_b but they recognized that both are related to the deep water waves through refraction. They defined θ_b as a function of θ_∞ by applying linear wave theory and they used an empirical relation to include the dependence of H_b on θ_∞. This method describes in a simplified way how a shoreline perturbation affects the wave field due to refraction over the associated perturbed bathymetry, which leads to alongshore gradients in θ_b and H_b. They obtained a maximum in alongshore transport for $\theta_\infty \approx 42°$, while the related values of θ_b ranged between $2° - 25°$ (depending on the wave steepness). Instability is possible above this critical angle and they also found an upper limit for the potential of instability at $\theta_\infty \approx 63°$; but this is the spurious result of a singularity in their solution. Without this upper limit, the maximum angle is 90°, at which the waves crests are perpendicular to the coast and the wave driven alongshore transport becomes zero.

Ashton *et al.* (2001) demonstrated the potential for shoreline instability for deep water wave incidence angles greater than 42° in a more clear way. They described Q in terms of the wave height and the wave angle at the base of the shoreface, H_∞ and θ_∞. This is the depth before nearshore refraction and shoaling takes place (the wave base) and in general they are referred to as 'deep water waves'. The deep water waves are not affected by the shoreline perturbations and they are therefore independent of ϕ and they are constant in alongshore direction. Ashton *et al.* (2001) transformed the CERC equation to a deep water version by applying linear wave theory and assuming refraction from deep water until breaking over depth contours that are locally parallel to the shoreline:

$$Q = K_2 H_\infty^{\frac{12}{5}} T_p^{\frac{1}{5}} \cos^{\frac{6}{5}}(\theta_\infty - \phi) \sin(\theta_\infty - \phi), \tag{1.7}$$

where T_p is the wave period, K_2 is a constant, the ratio between K_2 and K_1 is

$$K_2 = \left(\frac{\sqrt{g\gamma}}{2\pi} \right)^{\frac{1}{5}} K_1, \tag{1.8}$$

g is the gravity acceleration and γ is the breaking index (ratio between wave height and water depth for wave breaking). Figure 1.3b shows Q as a function of $\theta_\infty - \phi$ and shows that a maximum of Q is indeed present at $\theta_\infty - \phi = 42°$. Ashton & Murray (2006*b*) showed that other alongshore sediment transport formulations resulted into a similar curve for Q but the critical angle (for the maximum Q) ranged between 35° and 50°.

The consequence of the maximum of Q for the evolution of a shoreline undulation is illustrated in a schematized way in the lower two panels of figure 1.3. The offshore wave incidence angle is constant in alongshore direction and the magnitude of Q changes only due to variations in ϕ along the shoreline undulation. The magnitude of Q at different points along the undulation is indicated with symbols on the curve of the relative Q. In case of low wave incidence angles, the alongshore transport increases along the crest of the shoreline undulation (figure 1.3c). The transport gradient is negative updrift of the inflection point on the updrift flank, which leads to deposition. The gradient becomes positive along the crest until the inflection point on the downdrift flank, which leads to erosion. Downdrift of this inflection point the gradient is negative again, which leads

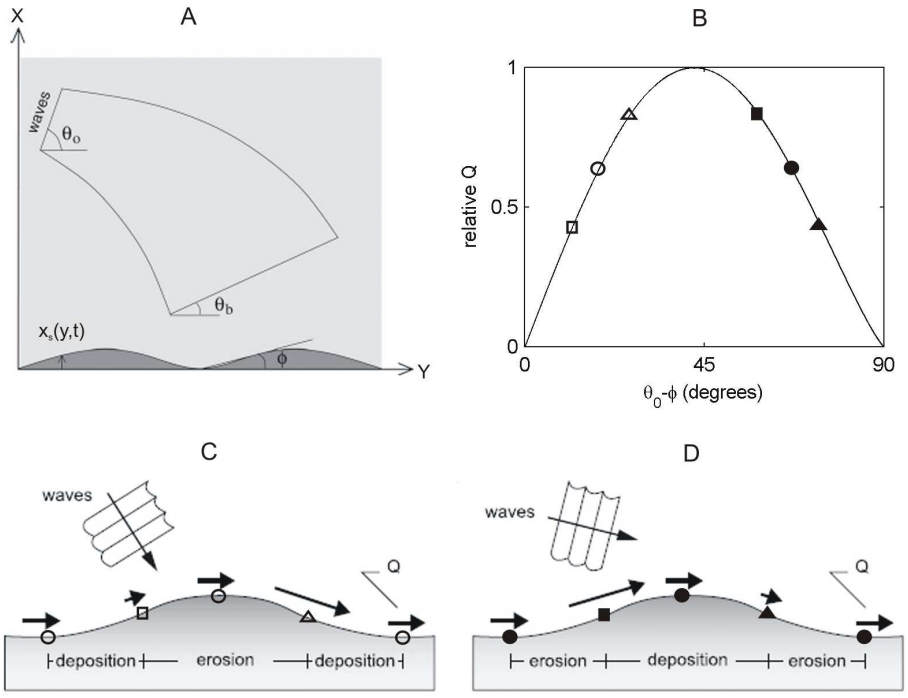

Figure 1.3: (a) Sketch of the nearshore region in plan view with the coordinate system and variables. The wave crests and the corresponding energy dispersion due to the stretching of the crest are indicated (Falqués *et al.*, 2011). (b) The relative alongshore sediment transport, Q, as a function of $\theta_\infty - \phi$ (equation 1.7). The alongshore transport pattern indicating zones of erosion and deposition for (c) low wave incidence angles (diffusion) and (d) high wave incidence angles (growth). The symbols indicate the relative magnitude of Q on the curve of panel b (adapted from Ashton & Murray, 2006*a*).

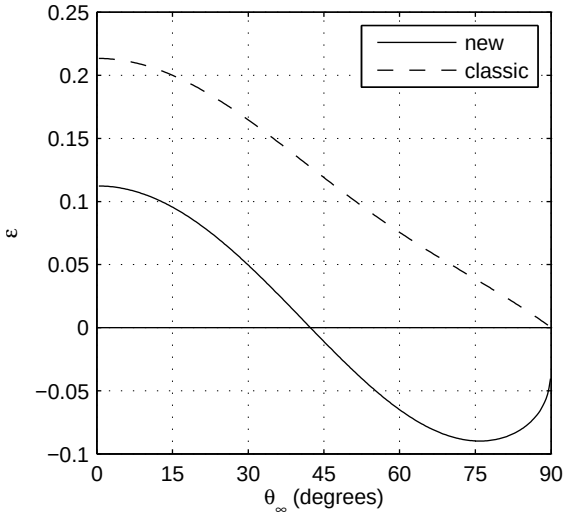

Figure 1.4: The shoreline diffusivity as a function of the deep water wave angle. The dashed line is computed with the classic approach and the solid line is computed numerically taking into account the dependance of θ_b and H_b on ϕ (Falqués, 2003).

to deposition. This pattern in alongshore transport leads to diffusion of the shoreline undulation just as the traditional one-line shoreline models predict. Figure 1.3d shows the situation for a high wave incidence angle and illustrates how the alongshore transport increases on the updrift flank and decreases at the crest and downdrift flank. The transport gradient is positive until the inflection point on the updrift flank (erosion) and becomes negative until the inflection point on the downdrift flank (deposition). Further downdrift it becomes positive again (erosion) and this pattern leads to the growth of the undulation and shoreline instability. This instability of the coastline will be referred to as 'high angle wave instability' (HAWI). In a less idealized situation the unstable pattern is usually shifted a bit in the downdrift direction, which results in growth and downdrift migration instead of pure growth.

The computation of the shoreline diffusivity, presented in the previous section, can be revised by inserting the deep water version of the CERC formula (equation 1.7) into equation (1.4) (see Ashton & Murray, 2006*a*). This revised shoreline diffusivity is lower than the classic one and, most importantly, it becomes negative above an angle of 42°. This was demonstrated previously by Falqués (2003), who solved the dependance of the θ_b and H_b on θ_∞ numerically by applying the Snell law, energy conservation and dispersion relation. Figure 1.4 shows the classic and the revised shoreline diffusivity as a function of θ_∞. The negative diffusivity indicates that a shoreline is potentially unstable for high wave incidence angles and that shoreline perturbations can grow.

The physical mechanism behind HAWI is the feedback of shoreline changes and the associated changes in the bathymetry into the wave field. If an undulation is present in

Figure 1.5: Wave refraction around a large scale shoreline undulation at Conception Bay in Namibia. Notice the decrease in wave energy in the surfzone at the downdrift flank due to wave energy dispersion. The horizontal line indicates 5 km and the north is in the right of the image (source: Google Earth).

the shoreline, the bathymetric lines follow this curvature up to a certain water depth. Refraction and shoaling over this undulating bathymetry leads to alongshore gradients in θ_b and due to stretching of the wave crests also to gradients in H_b (wave energy dispersion). Figure 1.5 shows how waves refract around the crest and the downdrift flank of a large scale shoreline undulation at Conception Bay in Namibia. Notice how the wave energy in the surfzone decreases at the downdrift flank. Wave energy dispersion is stronger on the downdrift flank and this leads to a relatively high H_b at the updrift flank and a relatively low H_b at the downdrift flank.

Instead of using the deep water version of the CERC formula of Ashton *et al.* (2001) we can use the CERC formula directly by computing the actual wave field over the evolving bathymetry and determining the values of θ_b and H_b. Equation (1.2) shows that the relative magnitude of Q is a function of $H_b^{5/2}$ and $\sin(2\alpha_b)$. Figure 1.6 shows both terms as a function of α_∞ and it can be seen that $\sin(2\alpha_b)$ increases up to high values of α_∞. The decrease of Q above 42° is therefore the result of the decrease of $H_b^{5/2}$ with α_∞. This illustrates that wave energy dispersion is the essential physical mechanism behind the occurrence of a maximum in Q and shoreline instability (Falqués, 2003; Ashton & Murray, 2006*a*; Falqués & Calvete, 2005; Falqués *et al.*, 2011). In addition, it can be seen that $\sin(2\alpha_b)$ decreases for very high relative incidence angles. This is the consequence of strong energy dispersion which leads to low waves, which break at a small water depth at which the waves have refracted to small incidence angles (Falqués *et al.*, 2011).

The role of the wave height and relative wave angle at breaking is clarified further in figure 1.7, which shows the gradients of Q, H_b and α_b $(\theta_b - \phi)$ along a shoreline

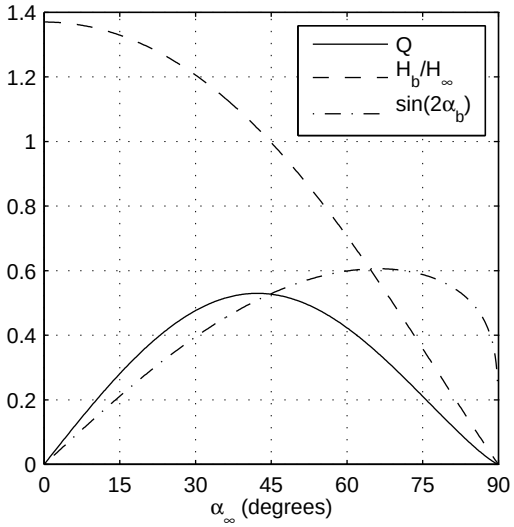

Figure 1.6: Non-dimensional alongshore sediment transport, $Q = (H_b/H_\infty)^{5/2}\sin(2\alpha_b)$, as a function of the relative wave angle in deep water, α_∞, the term depending on the wave height at breaking $(H_b/H_\infty)^{5/2}$ and the term depending on the wave angle at breaking, $\sin(2\alpha_b)$. Waves with $H_\infty = 1$ m and $T_p = 6$ s have been used, but other values give qualitatively similar results (Falqués *et al.*, 2011).

undulation. For low wave incidence angles, the angle term is dominant for Q and the alongshore gradients of the angle term result into a diffusional alongshore transport pattern. For high angle wave incidence, the wave height term becomes more important and its alongshore gradients result into an anti-diffusional transport pattern (growth and migration) (Falqués, 2003; Ashton & Murray, 2006*a*; Falqués & Calvete, 2005; Falqués *et al.*, 2011).

1.3.2 Previous modelling studies and their limitations

Ashton *et al.* (2001) explored HAWI with a non-linear cellular model, based on the one-line modelling approximation where the changes in shoreline position are simply governed by the gradients in the alongshore transport (equation 1.7). The model uses periodic boundary conditions and they found that small perturbations on a rectilinear coastline can grow and migrate if the incidence angle of the offshore waves is higher than the critical value. Non-linear effects like merging and wave shadowing, led to the coarsening of shoreline features and they reproduced large scale coastal patterns resembling shoreline sand waves, cuspate features and spits (Ashton & Murray, 2006*a*). The development of these patterns is the result of the feedback between the shoreline changes and the wave field via sediment transport. In this sense it is a self-organized process, similar to the formation of rhythmic patterns on a surfzone scale (Coco & Murray, 2007).

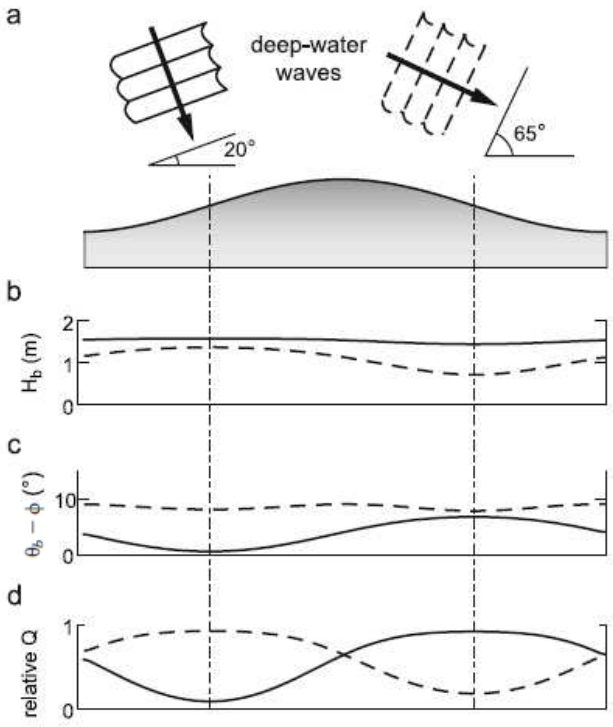

Figure 1.7: Variations in wave angle and height at breaking along an undulating shoreline and the resulting relative alongshore sediment transport: (a) non-exaggerated plot of a shoreline with deep water waves approaching from low angles (20°) and from high angles (65°), (b) wave height at breaking (H_b), (c) relative wave angle at breaking ($\theta_b - \phi$) and (d) relative sediment transport (Q). The solid lines indicate low angle and the dashed lines high angle waves. The values were computed for $H_\infty = 1$ m, $T_p = 10$ s (Ashton & Murray, 2006*b*).

Ashton & Murray (2006*b*) used their expression for shoreline diffusivity to analyze for several coasts if the net effect of the wave climate would result into diffusion or instability, indicating if HAWI could potentially play a role in the shoreline evolution. They concluded that HAWI could play a role in the formation of sand waves on Long Point spit in Lake Erie, USA and the formation of the Carolina Capes, USA. Other studies that analyzed the potential role of HAWI in shoreline evolution were Ashton *et al.* (2003); Falqués (2006); Slott *et al.* (2006); Medellín *et al.* (2009); Alves (2009); Caballeria *et al.* (2011); Falqués *et al.* (2011).

In the approach of Ashton & Murray (2006*a*), a crucial step is the computation of H_b and θ_b as a function of H_∞, θ_∞, wave period, T_p, and the nearshore bathymetry. They used linear wave theory and refracted the waves from the base of the shoreface (the wave base) over depth contours locally parallel to the shoreline, i.e. the value of $H_b(y)$ and $\theta_b(y)$ is computed by refracting the deep water waves over a rectilinear

bathymetry and the wave angle at deep water is $\theta_\infty - \phi(y)$. This simple wave refraction method does not account for the effect of the curvature of the actual bathymetry and therefore the convergence and divergence of wave rays at headlands and embayments is not described. Moreover, it implicitly assumes that shoreline undulations extend into the bathymetry up to deep water (the wave base). In addition the model assumes, just as one-line models, that the cross-shore profile retains a constant shape and that any gradient in alongshore transport leads to an instantaneous shift of the shoreline position and the whole cross-shore profile. Ashton & Murray (2006*a*) described their model as an exploratory model and stated that the underlying model assumptions prescribe a spatial scale below which the results should not be compared to nature. However, it remains unclear what this minimal spatial scale is. Disregarding the curvature of the bathymetric lines and implicitly assuming that shoreline features extend up to the wave base only seems valid for very large scale features and it remains unclear if HAWI can correctly predict the initial growth of shoreline perturbations and if it is a valid mechanism for the dynamics of shoreline sand waves, which are relatively subtle features.

Falqués & Calvete (2005) developed a one-line model which takes into account refraction over curvilinear bathymetric lines and uses a finite extension of the perturbations in the cross-shore direction. They used linear stability analysis to explore the HAWI mechanism. The complex growth rates of small amplitude perturbations gave information on the shoreline diffusivity and migration rates. They found that shoreline instability developed for high wave incidence angles, provided that the offshore extension of the perturbations in the bathymetry (a free parameter) was large enough. This enlightens the importance of cross-shore profile dynamics for the HAWI mechanism. Furthermore, the range of unstable angles was significantly reduced for long period waves. Thus, the critical angle proposed by Ashton *et al.* (2001), $\theta_\infty = 42^\circ$, is actually a lower bound and instability in general requires larger angles and short wave periods. A very important output of the linear stability analysis was a wavelength selection for the initial development of the shoreline sand waves ($\lambda \sim 3 - 15$ km) and they found a typical initial growth time of $1 - 10$ yr. Since this study used a linear approach it is only valid for small amplitude perturbations and it only gives information on the initial tendency to diffusion/growth and migration. A second limitation is that the cross-shore extent of the perturbation was fixed in time and the model is still based on the assumption of an instantaneous reaction of the shoreline and the cross-shore profile to gradients in alongshore transport.

In a similar way, Uguccioni *et al.* (2006) also used a linear stability analysis to investigate HAWI. They included irregular waves and dissipation due to wave breaking into their model and computed the integrated alongshore transport from the current field using the energetics based sediment transport of Bailard. It was found that including the inertia of the alongshore current and a delay in sediment entrainment, led to slightly larger wavelengths. They also recognized that the development of instability was very sensitive to the cross-shore extent of the shoreline perturbations. This study shares the limitations of Falqués & Calvete (2005), which were mentioned in the previous paragraph.

List & Ashton (2007) confirmed that a shoreline can potentially be unstable for high angle wave conditions by modelling initial transport gradients along a shoreline undulation with the use of a fully 2DH process-based wave, circulation and sediment

transport model. They used two methods to compute the alongshore transport gradients: i) the CERC formula using H_b and θ_b computed with a spectral wave model and ii) integration of alongshore component of the total transport computed with the process-based model. Both approaches gave similar results and it was shown that the approach of Ashton *et al.* (2001) seems to overpredict shoreline instability. They used different length scales for the undulations and their results suggest that a minimal length scale is required for instability. Even when the transport gradients did not indicate growth of the perturbation (due to a small length scale or inadequate wave conditions), the transport pattern was never pure diffusive and predicted downdrift migration. The main limitation of this study is that it did not compute the morphological evolution and doing so would lead to a very long computation time.

1.4 Research objectives and outline

The main objective of this study is *to provide more insight into the formation and dynamics of shoreline sand waves and, in particular, to explore the role of high angle wave instability.* Previous modelling studies used several simplifications and approximations and in this study it is explored how this affects the model predictions. To this end, a non-linear morphodynamic model for large scale shoreline dynamics is used. This model, called Q2D-morfo, is an extension of the one-line model used by Falqués & Calvete (2005) and it overcomes some of the limitations of the previous studies. First of all it overcomes the inherent limitations of the linear stability analysis of Falqués & Calvete (2005); Uguccioni *et al.* (2006). It can describe non-linear effects and large amplitude shoreline perturbations. Second, it computes the wave field over the evolving bathymetry and therefore takes into account refraction over curvilinear depth contours, a process which was not included by Ashton & Murray (2006*a*). Third, the cross-shore extension of the shoreline perturbations is finite and dynamic due to the inclusion of cross-shore dynamics. This provides an improvement with respect to: i) the instantaneous adaptation of the cross-shore profile assumed by Ashton & Murray (2006*a*); Falqués & Calvete (2005); Uguccioni *et al.* (2006), ii) the assumption of Ashton & Murray (2006*a*) that shoreline perturbations extended up to the deep water (wave base) and iii) the fixed cross-shore extent of shoreline perturbations used by Falqués & Calvete (2005); Uguccioni *et al.* (2006). Moreover, the quasi 2D approach allows us to look directly at gradients of the alongshore sediment transport, wave height and wave angle, in combination with morphological evolution. This is expected to provide more insight into the physical mechanism behind HAWI and the occurrence of a characteristic length scale for sand wave formation. A preliminary version of the Q2D-morfo model was presented in Falqués *et al.* (2008) but for the present study various improvements were made. The main objective of this study is pursued by answering the following research questions:

1. Does the Q2D-morfo model predict the formation of shoreline sand waves due to high angle wave instability?
2. If so, under what conditions and what are the characteristics of the shoreline sand waves?

3. What role do cross-shore dynamics play in high angle wave instability and the dynamics of shoreline sand waves?
4. What is the effect of variable wave incidence angles on the formation and dynamics of shoreline sand waves?
5. What is the physical mechanism behind high angle wave instability?
6. Does the Q2D-morfo model predict an optimal wavelength for sand wave formation and what is the underlying physical mechanism?
7. How do the predictions of the Q2D-morfo model compare to previous modelling studies and to what extent do the simplifications and approximations of the previous studies affect their predictions?
8. How do the predictions of the Q2D-morfo model compare to existing observations of shoreline sand waves?

This dissertation is divided into 8 chapters. *Chapter 2* describes the Q2D-morfo model and the governing equations. Details of the numerics and discretization are discussed and some improvements that were made for this study are indicated.

In *chapter 3* the formation of sand waves from random initial perturbations is studied. The sensitivity to the wave incidence angle, wave height and wave period is examined and the role of the cross-shore dynamics is explored. The chapter is concluded with an assessment of the sensitivity to numerics and boundary conditions.

In *chapter 4* the formation of sand waves from a localized initial perturbation is studied. The sensitivity to the wave incidence angle and the dimension of the perturbation is examined. In this chapter special attention is payed to the implications of HAWI for shore nourishment.

Chapter 5 focuses on the effect of variable wave incidence angles on the formation of sand waves from both random and a localized perturbation. Simulations are done with different fractions of high and low wave incidence angles and with fractions of waves coming from opposite directions.

In *chapter 6* the physical mechanisms behind HAWI are studied. The gradients in alongshore transport, wave height and wave angle are analyzed in order to explain the shoreline evolution. Simulations are done to find the optimal length scale for sand wave formation and the physical mechanism behind wavelength selection is studied. The chapter is concluded with a discussion on the model limitations, finite amplitude behaviour and the bathymetry of shoreline sand waves.

In *chapter 7* the model results are compared qualitatively with observations of sand waves from existing literature. In addition, some shoreline sand wave fields on the southwest coast of Africa are studied with the use of satellite images and the results are compared with model simulations using the conditions of this coast. The chapter is concluded with a discussion on the uncertainties that remain on the role of HAWI in the formation and dynamics of the observed sand waves.

Chapter 8 gives an overview of the most important conclusions of this study and gives some suggestions for future research.

Chapter 2

Model

The Q2D-morfo model is a non-linear morphodynamic model for large scale shoreline dynamics on a medium to long term time scale. Just as traditional one-line models, it is based on the assumption that on this spatial and time scale the shoreline dynamics is controlled by gradients in the alongshore transport. However, instead of integrating the alongshore transport in the cross-shore direction and limiting morphological evolution to an instantaneous shift of the whole cross-shore profile and the corresponding shoreline position, the model describes the alongshore transport with a cross-shore distribution and uses a parameterized description of the cross-shore transport. The model therefore computes sediment transport in two dimensions and the convergence or divergence of the transport results into morphological changes. The wave field is computed over the evolving bathymetry but the nearshore hydrodynamics is not computed. The alongshore transport is computed directly from the wave field with the CERC formula and the cross-shore dynamics is described by a diffusive transport. These simplifications reduce the computational cost compared to full 2DH models but limits the application to large spatial scales and consequently surfzone morphodynamics, as rip currents and nearshore sand bar dynamics, can not be reproduced. Hence the Q in the model name, which stands for 'quasi'. A first version of the model was presented in Falqués *et al.* (2008). The present version includes some improvements in the discritization and the boundary conditions. First the general model formulations are presented and finally the details of the discritization is discussed.

2.1 Grid, equilibrium profile and bathymetry

A Cartesian frame with horizontal coordinates x, y and upward vertical coordinate z is used, where y runs along the initial mean shoreline orientation and x represents the cross-shore direction. The nearshore region is represented by a rectangular domain, $0 < x < L_x$ and $0 < y < L_y$, and a staggered grid is used (figure 2.1). The bed level is

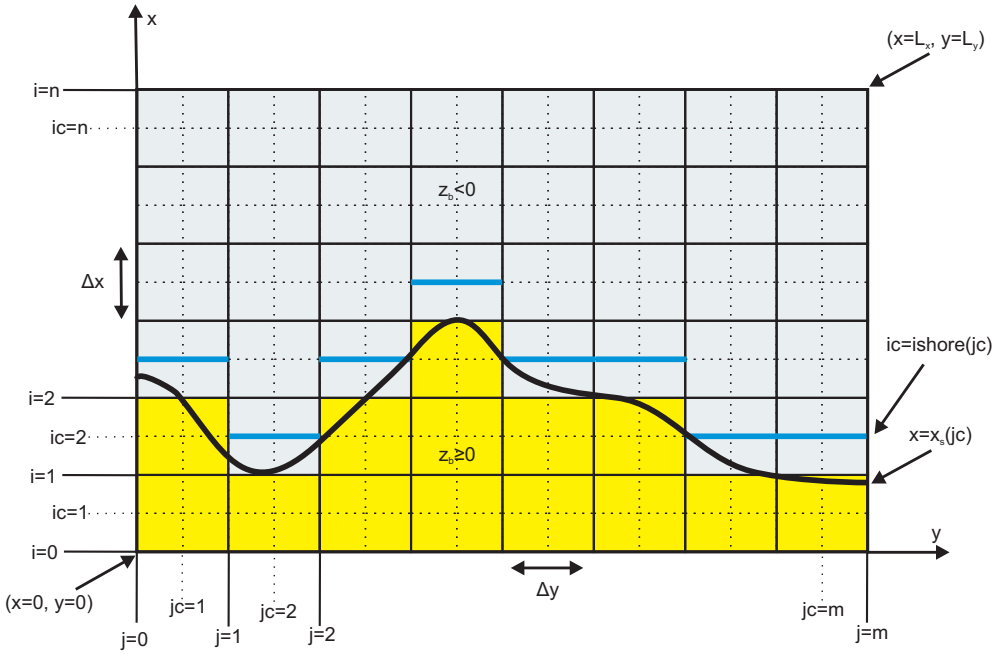

Figure 2.1: Geometry of the modeling domain and the staggered grid.

defined by $z_b(x, y)$. The shoreline position $x_s(y)$ is determined by interpolating in cross-shore direction between the last dry cell ($z_b \geq 0$) and first wet cell ($z_b < 0$, indicated by $ishore(y)$).

An equilibrium cross-shore profile needs to be defined. It can be read from an external file or an analytical profile, like a Dean shape profile, can be used. The initial bathymetry, z_b, can be defined from an external file or it can be constructed as an alongshore repetition of a cross-shore profile. In general it is recommended to define the initial bathymetry as a repetition of the equilibrium profile or to define the equilibrium profile as the average cross-shore profile of the bathymetry. Various initial perturbations can be added to the bathymetry (e.g., random small scale perturbations, alongshore rhythmic perturbations, a localized large scale perturbation).

2.2 Bed evolution and sediment transport

The dynamical equation for the bed level, $z_b(x, y, t)$, is sediment mass conservation,

$$\frac{\partial z_b}{\partial t} + \frac{\partial q_x}{\partial x} + \frac{\partial q_y}{\partial y} = 0, \tag{2.1}$$

where $\vec{q} = (q_x, q_y)$ is the depth integrated sediment flux (Soulsby, 1997). The bed porosity factor is included for convenience in $\vec{q}$ as $1/(1-p)$.

The depth integrated sediment flux is decomposed as

$$\vec{q} = \vec{q}_L + \vec{q}_C + \vec{q}_D. \tag{2.2}$$

The first term, $\vec{q}_L$, represents the alongshore transport, which is due to the alongshore current driven by the breaking waves in case of oblique wave incidence. The second term, $\vec{q}_C$, is a parameterization of cross-shore sediment transport processes and the third term, $\vec{q}_D$, is an alongshore diffusive transport that suppresses the growth of small scale noise.

2.2.1 Wave driven alongshore transport

The wave driven alongshore transport is evaluated by first computing the total sediment transport rate, i.e., cross-shore integrated flux with an extended version of the CERC formula (Komar, 1998). The formula has been adapted to include a second term introduced by Ozasa & Brampton (1980), which represents the contribution of alongshore gradients in wave height to the alongshore transport,

$$Q = \mu H_b^{5/2} \left(\sin(2\alpha_b) - \frac{2r}{\beta} \cos(\alpha_b) \frac{\partial H_b}{\partial y} \right), \tag{2.3}$$

where $H_b(y)$ is the root mean square wave height at breaking, $\alpha_b = \theta_b(y) - \phi(y)$ is the angle between wave fronts at breaking and the local average coastline orientation and β is the mean surfzone slope. The constant μ controls the magnitude of the transport and is proportional to the empirical parameter K_1 of the original CERC formula, which depends mainly on the sediment grain size. As a default value we use $K_1 = 0.7$ (grain size $D_{50} = 0.3$ mm), which roughly corresponds to $\mu = 0.2$ m$^{1/2}$s^{-1} (considering a sediment density of 2650 kg/m^3, a water density of 1020 kg/m^3 and a breaking index of 0.5). The constant r is equal to K_2/K_1, where K_2 is the empirical parameter of the second term. The default value of $r = 1$ is used which is equivalent to $K_2 = K_1$. Then, the sediment flux is computed by multiplying the total transport rate by a normalized shape function $f(x)$, qualitatively based on the cross-shore profile of the alongshore current (Komar, 1998),

$$\vec{q}_L = f(x - x_s(y))Q(y)(\sin\phi(y), \cos\phi(y)), \tag{2.4}$$

with

$$f(x) = \frac{4}{\sqrt{\pi}L^3} x^2 e^{-(x/L)^2}, \tag{2.5}$$

where $L = 0.7X_b(y)$ and $X_b(y) = x_b(y) - x_s(y)$ is the width of the surfzone. The point of breaking, $x_b(y)$, is the most offshore point where $H(x, y) \geq \gamma_b D(x, y)$. D is the water depth and and γ_b is the breaking index. The local average coastline orientation , ϕ, is represented by the mean orientation of the bathymetric contours in the surf zone with respect to the y axis rather than the orientation of the coastline itself. This seems more appropriate because is this orientation that actually effects the waves at breaking. It is computed as

$$\sin\phi(y) = \overline{\frac{\partial z_b}{\partial y}} \Big/ \sqrt{\left(\overline{\frac{\partial z_b}{\partial x}}\right)^2 + \left(\overline{\frac{\partial z_b}{\partial y}}\right)^2}, \tag{2.6}$$

where the average is computed within a rectangular box with the size of the surfzone.

Care must be taken when the empirical CERC formula is used for quantitative predictions of alongshore transport and the resulting shoreline change (Cooper & Pilkey, 2004). In this study we only look at the qualitative behavior and the use of CERC formula therefore seems valid. Ashton & Murray (2006*a*) explored other formulas for breaking-wave-driven transport and found that all formulas show the potential for shoreline instability but that they may predict somewhat different shoreline responses under the same conditions. An interesting study by List & Ashton (2007) demonstrated that the cross-shore integrated alongshore transport computed with a process-based wave, circulation, and sediment transport model showed patterns along an undulating shoreline similar to the transport computed directly from the wave field with the CERC formula. Even though they did not compute morphological evolution, the process based model predicted the potential for high angle wave instability, confirming that the present simplified approach using the CERC formula is valid.

2.2.2 Diffusive cross-shore transport

The second term in equation (2.2) is a parameterization of cross-shore sediment transport processes, which redistributes sediment between the dry beach, the surf zone and the shoaling zone. Several parametrizations could be used (e.g. Bailard, 1981; Plant *et al.*, 2001) but here use the assumption that, on a relatively long time scale, these processes drive the cross-shore profile to an equilibrium profile z_{be}, so that

$$\vec{q}_C = -\gamma_x \left(\frac{\partial (z_b - z_{be})}{\partial x} \, , \, 0 \right), \tag{2.7}$$

where $z_{be}(x, y) = Z(x - x_s(y))$ is the assumed equilibrium profile and γ_x is a cross-shore diffusivity coefficient.

The physical basis for the coefficient γ_x is the diffusivity caused by wave breaking. Thereby, it depends on the wave energy dissipation and its order of magnitude has been estimated by using the expression for momentum mixing due to wave breaking (Battjes, 1975),

$$\nu_t = M(\mathcal{D}/\rho)^{1/3} H, \tag{2.8}$$

where M is a non-dimensional constant ($O(1)$), $\mathcal{D}$ is the wave energy dissipation per time and area unit, ρ is the water density and H is the root mean square wave height. We assume that γ_x scales with ν_t, with $H = H_b$ in equation (2.8). The order of magnitude of $\mathcal{D}$ can be estimated as the total energy flux entering the surfzone divided by the cross-shore length,

$$\mathcal{D} \sim \frac{1}{8} \rho g H_b^2 \frac{c_{gb}}{X_b}, \tag{2.9}$$

where g is the gravity acceleration and c_{gb} is the group celerity at breaking, computed with the shallow water assumption ($c_g \simeq \sqrt{gD}$). An estimation for the morphodynamic diffusivity is therefore,

$$\gamma_x(x, y) = \epsilon_x \, \gamma_b^{-1/6} \, g^{1/2} H_b^{11/6} X_b^{-1/3} \, \psi(x - x_s(y)), \tag{2.10}$$

where ϵ_x is a non-dimensional constant. The shape function,

$$\psi(x) = \frac{1 + b + \tanh((X_1 - x)/L_d)}{1 + b + \tanh(X_1/L_d)}, \tag{2.11}$$

has a cross-shore distribution with a maximum in the surf zone and it decays to almost zero at the depth of closure, D_c. The parameter X_1 depends on the width of the surfzone ($factor \cdot X_b$) and it controls the position of D_c. The parameter L_d controls the length scale of the decay until X_1 and offshore of this point the shape function tends to a residual value controlled by b.

Notice that the cross-shore equilibrium profile is assumed to be perpendicularly to the y axis instead of perpendicular to the evolving local shoreline orientation. Consequently, the flux given by equation (2.7) is assumed to be in the direction of the x axis. The inaccuracy introduced by this approximation is not significant if the amplitude of the shoreline variations are relatively small, i.e., if the changes in shoreline orientation are small.

2.2.3 Diffusive alongshore transport

The third term in equation (2.2) is an alongshore diffusive transport that suppresses the growth of small scale noise,

$$\vec{q}_D = -\gamma_y \left(\frac{\partial z_b}{\partial x} \sin\phi + \frac{\partial z_b}{\partial y} \cos\phi \right) (\sin\phi, \cos\phi). \tag{2.12}$$

The coefficient $\gamma_y(x, y)$ is computed in a similar way as $\gamma_x(x, y)$ in the previous section but with a coefficient ϵ_y. Notice that just as the wave driven alongshore transport, this diffusive transport is parallel to the average local coastline orientation, ϕ.

2.2.4 Boundary conditions

The boundary condition

$$\vec{q}_s = \gamma_s \left(\frac{\partial z_b}{\partial x} \cos\phi_s - \frac{\partial z_b}{\partial y} \sin\phi_s - \beta_s \right) (\cos\phi_s, -\sin\phi_s), \tag{2.13}$$

is assumed at the shoreline, where ϕ_s is the local angle between the shoreline and the y axis ($\tan(\phi_s(y)) = \partial x_s(y)/\partial y$). This means that the swash zone slope relaxes to an equilibrium slope β_s. If the swash slope is smaller than the equilibrium slope, sediment is transported from the wet cells to the dry cells and the shoreline advances seaward. If the swash slope is steeper, the dry beach is eroded and the shoreline retreats. The coefficient γ_s is related to the relaxation time T_s by $\gamma_s \sim (\Delta x)^2/T_s$, where Δx is the grid size and T_s is of the order of a few hours.

At the offshore boundary, $x = L_x$, it is assumed that the bathymetry relaxes to the equilibrium bathymetry within a certain decay distance λ_x from the boundary,

$$\frac{\partial(z_b - z_{be})}{\partial x} = -\lambda_x^{-1}(z_b - z_{be}), \tag{2.14}$$

which, according to equation (2.7), can also be written as

$$(q_C)_x = \gamma_x \lambda_x^{-1}(z_b - z_{be}). \tag{2.15}$$

At the lateral boundaries ($y = 0, L_y$) the diffusive transport is assumed to be zero and the sediment flux is only controlled by the wave driven alongshore transport (equation 2.3). In this sense, open boundary conditions are used, so that sediment is not necessarily conserved within the domain and the bathymetry can evolve freely. The wave driven alongshore transport depends on the local values of H_b, θ_b and ϕ. The value of ϕ at the lateral boundaries is however not obvious because it is the average surfzone orientation within a rectangle and the bathymetry outside the domain is unknown. If ϕ is determined by only using interior cells a positive feedback between the surfzone orientation and gradients in Q can arise, leading to a numerical instability that causes strong artificial accretion or erosion at the boundary. To avoid this, the following boundary condition is used,

$$\frac{\partial \phi}{\partial y} = \pm(\lambda_y)^{-1}\phi \qquad , y = 0, L_y. \tag{2.16}$$

This is consistent with an exponential decay to zero of ϕ far from the domain. The e-folding length of the decay is set to $\lambda_y = 500$ m and this has proven to lead to realistic behavior at the boundaries.

2.3 Waves

2.3.1 Wave field computation

The computation of the sediment transport requires the wave height and angle at the breaking point, $x_b(y)$. The internal wave module computes the wave field, $H(x, y)$ and $\theta(x, y)$, within the domain using the wave height, period and angle given at the offshore boundary. Applying linear wave theory (Holthuijsen, 2007) gives the dispersion relation,

$$\omega^2 = gk \tanh(kD), \tag{2.17}$$

the equation for wave number irrotationality,

$$\frac{\partial(k \sin\theta)}{\partial x} = \frac{\partial(-k \cos\theta)}{\partial y}, \tag{2.18}$$

and the wave energy conservation,

$$\frac{\partial}{\partial x}(-c_g H^2 \cos\theta) + \frac{\partial}{\partial y}(c_g H^2 \sin\theta) = 0. \tag{2.19}$$

Here $\omega = 2\pi/T_p$ is the radian frequency, T_p is the peak period, $\vec{k} = (k_x, k_y) = k(-\cos\theta, \sin\theta)$ is the wave number vector, D is the water depth, c_g is the group celerity,

$$c_g = \frac{1}{2}\left(1 + \frac{2kd}{\sinh(2kD)}\right)\sqrt{\frac{g}{k}\tanh(kD)}, \tag{2.20}$$

and θ is the angle of the wave crest with respect to the y-axis. This approach takes into account refraction and shoaling but it neglects diffraction and dissipation by bottom shear stresses. Dissipation by wave breaking is not included because the wave field is only needed up to the point of breaking. The wave field is computed every time-step Δt_w.

There is also an option to compute the wave field with the combined refraction-diffraction model Ref/Dif1 (Kirby & Dalrymple, 1994). This model uses the parabolic mild slope equation and includes diffraction and dissipation by bottom shear stresses. The model is however computationally more demanding and, most importantly, numerical errors develop for very oblique wave incidence.

2.3.2 Realistic range of wave angles

In theory, any wave angle is possible in infinitely deep water. However, the angle between wave fronts and coastline decreases as water depth decreases because of wave refraction. This poses an upper bound on the wave angles that are realistic at the offshore boundary of the model domain. Wave refraction depends on the wave period and shorter wave periods allow for larger angles at a given water depth.

For any wave period the maximum allowed wave angle can be determined by assuming $\theta = \theta_\infty$ at an offshore water depth, D_∞, and refracting the waves up to the water depth of the offshore boundary, $D_0 = D(L_x)$. The angle θ_0 is found by solving equations (2.17) and (2.18). The latter reduces to the Snell law, $k_o \sin\theta_0 = k_\infty \sin\theta_\infty$, by assuming rectilinear and parallel depth contours. Taking, for example, $D_\infty = 250$ m, and $\theta_\infty \to 90°$, the angle θ_0 at D_0 gives the maximum incidence angle allowed at such depth. The results for the maximum angle as a function of wave period and D_0 are shown in figure 2.2. Larger water depths in deep water, D_∞, give the same results for a wave period not larger than about 20 s.

2.4 Numerics and discretization

The set of equations is discretized in space by standard finite differences on the staggered grid shown in figure 2.1. The grid is defined as:

$$\begin{aligned} x(i) &= i\Delta x \qquad i = 0, 1, ...n \\ y(j) &= j\Delta y \qquad j = 0, 1, ...m \end{aligned} \tag{2.21}$$

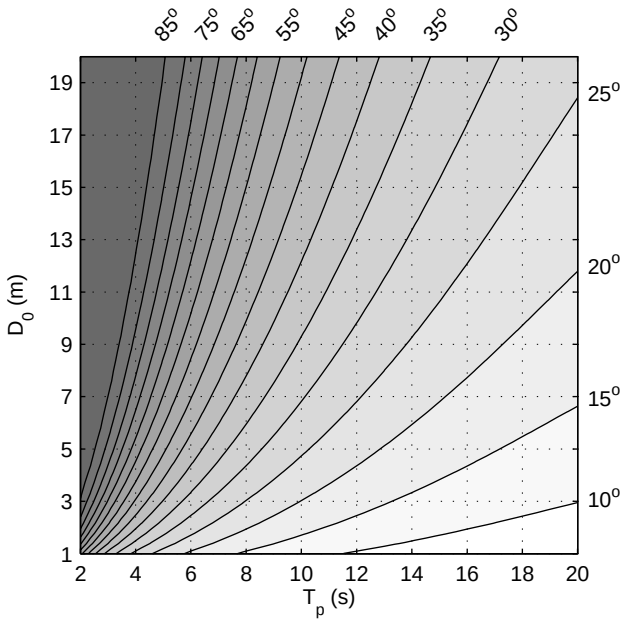

Figure 2.2: Maximum allowed wave angle at water depth D_0 as a function of wave period, T_p. A deep water angle $\theta_\infty = 89.9°$ is assumed at a water depth $D_\infty = 250$ m.

$$\begin{aligned} x(ic) &= x(i) - \Delta x/2 \qquad i = ic \qquad ic = 1, 2, ...n \\ y(jc) &= y(j) - \Delta y/2 \qquad j = jc \qquad jc = 1, 2, ...m \end{aligned} \tag{2.22}$$

where $\Delta x = L_x/n$ and $\Delta y = L_y/m$. The instantaneous time is descretized as $t(k) = t_0 + k\Delta t$, where $k = 0, 1..., n_t$ is the time index and t_0 is the initial time and n_t is the final time.

2.4.1 Sediment mass conservation

The sediment mass conservation (equation 2.1) is discretized in time by a second order Adam-Bashforth explicit method.

$$zb^k_{ic,jc} = zb^{k-1}_{ic,jc} - (\frac{3}{2}\, div^{k-1}_{ic,jc} - \frac{1}{2}\, div^{k-2}_{ic,jc})\, \Delta t \tag{2.23}$$

$$div^k_{ic,jc} = \frac{q_x(i,jc)^k - q_x(i-1,jc)^k}{\Delta x} + \frac{q_y(ic,j)^k - q_y(ic,j-1)^k}{\Delta y} \tag{2.24}$$

Here, q_x is the sum of the cross-shore diffusive transport (equation 2.7), the cross-shore components of the wave driven and diffusive alongshore transport and the transport at the shoreline (equations 2.4, 2.12 and 2.13). The term q_y is the sum of the alongshore components of the wave driven and diffusive alongshore transport and the transport at

the shoreline. The use of an explicit method gives a Courant-Friedrichs-Lewy stability condition (Smith, 1985) of the type

$$\Delta t < cH^{-3/2}\frac{(min\{\Delta x, \Delta y\})^2}{max\{\epsilon_x, \epsilon_y\}}, \tag{2.25}$$

which is based on the morphological diffusivity that is roughly proportional to $H^{3/2}$. Numerical experiments show that $c \sim 0.13$ m$^{-1/2}$ s.

2.4.2 Sediment transport

An important improvement with respect to the previous version of the model, is the introduction of the variable $celltype(ic, jc)$. This variable distinguishes between wet cells and dry cells and for each wet cell it is evaluated if the cell is bordered by wet or dry cells or a boundary. The *celltype* is determined during the first time step in the whole domain and subsequently it is only updated within a window around the shoreline because changes only occur there. This approach allows for a dynamic shoreline with large amplitude variations and the possibility to introduce coastal structures.

For each *celltype*, we defined which sediment flux has to be computed (figure 2.3). For each wet cell the wave driven and diffusive alongshore transport (equations 2.4 and 2.12) are computed at ic, j if the adjacent cell is also wet. At the lateral boundaries ($j = 0, j = m$) only the wave driven transport is computed (see section 2.2.4). The cross-shore diffusive transport (equation 2.7) is evaluated at i, jc and the offshore boundary condition (equation 2.15) is used at $i = n$. The cross-shore components of the alongshore transport need to be added to the cross-shore transport. Because they are not defined at the same node, the average of the four surrounding nodes, $\overline{q_{Lx}} + \overline{q_{Dx}}$ is computed and added to q_x.

The $celltype(ic, jc)$ that is a wet cell neighbored by a dry cell on the landward side, indicates the shoreline boundary ($ic = ishore$). In the previous version of the model there was no sediment flux between the wet and dry cells and shoreline evolution was done by an iterative process after the updating of the bathymetry. The process moved sand in cross-shore direction between a wet cell and a dry cell in order to adjust to the equilibrium swash slope β_s. In the present version, a sediment flux is computed at the shoreline ($\vec{q}_s(i, jc)$), with cross-shore and alongshore components (equation 2.13). The alongshore of $\vec{q}_s$ component however needs to be implemented at ic, j. If the angle of the shoreline ($\alpha_s(jc)$) is positive and $z_b(ic - 1, jc - 1) < 0$ it is implemented at $(ic - 1, j = jc - 1)$ (see figure 2.3). If the angle of the shoreline ($\alpha_s(jc)$) is negative and $z_b(ic - 1, jc + 1) < 0$ it is implemented at $(ic - 1, j = jc)$. There is no alongshore component of $\vec{q}_s$ at the lateral boundaries, $jc = 1$ and $jc = m$.

The sum of the alongshore components of $\vec{q}_L$, $\vec{q}_D$ and $\vec{q}_s$ give q_y and the sum of the $\vec{q}_C$, the cross-shore component of $\vec{q}_s$ and $\overline{q_{Lx}} + \overline{q_{Dx}}$ give q_x. Finally the divergence of $\vec{q}$ and the resulting changes in $z_b(ic, jc)$ are computed with equation (2.24).

When the coastline is parallel to the y axis, $ic = ishore(j) =$ constant. However, when

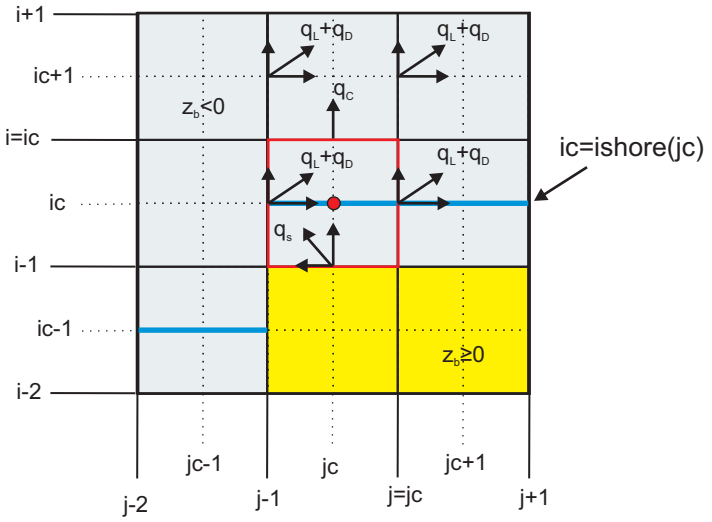

Figure 2.3: Example of the definition of the sediment fluxes relevant for the cell (red square) at the node ic, jc (red dot). q_s is the cross-shore transport flux at the shoreline and it is decomposed in an alongshore and cross-shore component. q_C is the cross-shore diffusive transport flux. q_L is the alongshore wave driven transport flux and q_D is the diffusive transport flux and they are decomposed in an alongshore and cross-shore component.

the shoreline orientation deviates from that, jumps occur in $ic = ishore(j)$. Simulations show that if these jumps become bigger than 2 units ($|ishore(j+1) - ishore(j)| > 2$, the sediment transport does not correctly distribute the sediment between the surf zone and the shoreline, leading to erosion at the shoreline and an artificial increase of the jumps in the shoreline. This gives an approximate limitation on the shoreline angle and consequently also on the amplitude of the shoreline variations: $|\tan\phi_s| \lesssim 2\Delta x/\Delta y$.

2.4.3 Waves

The wave field is computed by first determining the modulus of the wavenumber $k(ic, jc)$ using equation (2.17). Then, the wave angle $\theta(ic, jc)$ can be determined with equation (2.18) and finally, solving equation (2.19) gives the wave height $H(ic, jc)$. The offshore boundary conditions are given at the points (ic, jc) with $ic = n$.

2.4.3.1 Wave number and angle

Equation (2.17) is solved with a Newton-Raphson iterative scheme, progressing onshore from the offshore boundary until a limiting water depth (see section 2.4.3.3).

Once $k(ic, jc)$ is known, $\theta(ic, jc)$ can be computed by solving equation 2.18 for the unknown $\xi = k_y = k \sin\theta$,

$$\frac{\partial \xi}{\partial x} = -\frac{\partial}{\partial y}\sqrt{k^2 - \xi^2} \tag{2.26}$$

In case of positive offshore angles this equation is discretized with a backward scheme in the direction of the y axis, from $y = 1$ until $y = m$ and from the seaward boundary until a limiting water depth,

$$\xi_{ic-1,jc} = \xi_{ic,jc} + \frac{\Delta x}{\Delta y}\sqrt{k^2_{ic,jc} - \xi^2_{ic,jc}} - \sqrt{k^2_{ic,jc-1} - \xi^2_{ic,jc-1}}. \tag{2.27}$$

For negative angles, a forward scheme is used,

$$\xi_{ic-1,jc} = \xi_{ic,jc} + \frac{\Delta x}{\Delta y}\sqrt{k^2_{ic,jc+1} - \xi^2_{ic,jc+1}} - \sqrt{k^2_{ic,jc} - \xi^2_{ic,jc}}. \tag{2.28}$$

At the upwave lateral boundary we consider that the bathymetric lines that affect the waves (outside the domain) are rectilinear and that ξ is therefore constant. At the downwave boundary the waves are affected by the bathymetry within the domain and ξ is computed with the corresponding scheme.

In the previous version of the model the backward or forward scheme was simply chosen by looking at the offshore wave angle and for normal wave incidence the backward scheme was used. However, for normal waves a centered scheme should be used. Moreover, for normal wave incidence or small angles, the angle of a wave ray may change direction due to refraction and the scheme can not be chosen by only looking at the offshore wave angle. In the present version a centered scheme is added,

$$\xi_{ic-1,jc} = \xi_{ic+1,jc} + \frac{\Delta x}{\Delta y}\sqrt{k^2_{ic,jc+1} - \xi^2_{ic,jc+1}} - \sqrt{k^2_{ic,jc-1} - \xi^2_{ic,jc-1}}, \tag{2.29}$$

and the angle at the seaward cell is evaluated to be able to choose the correct scheme. The centered scheme can not be applied at the lateral boundaries. If the wave incidence is shore normal, ξ is considered constant at both lateral boundaries. At the seaward boundary, $x = n$, θ is given by the offshore wave angle and at $x = n - 1$ the centered scheme can not be used and a first order scheme is used instead. Once $\xi(x, y)$ is known, $\theta(x, y)$ can be found from $\sin\theta = \xi/k$

2.4.3.2 Wave height

To obtain $H(ic, jc)$, equation (2.19) is written as

$$\nabla \cdot (H^2 \vec{c_g}) = 0 \qquad \Rightarrow \tag{2.30}$$

$$\vec{c_g} \nabla \cdot (H^2) + H^2 \nabla \cdot \vec{c_g} = 0 \qquad \Rightarrow \tag{2.31}$$

$$c_g \frac{\partial (H^2)}{\partial s} + H^2 \nabla \cdot \vec{c_g} = 0 \tag{2.32}$$

where $\partial/\partial s$ is the derivative along the wave ray. By defining

$$\mathcal{E} = \ln(H^2) \tag{2.33}$$

and

$$\Phi = \frac{-(\nabla \cdot \vec{c_g})}{c_g}. \tag{2.34}$$

we obtain:

$$\frac{\partial \mathcal{E}}{\partial s} = \Phi \tag{2.35}$$

The variable $\mathcal{E}(ic, jc)$ is computed at the offshore boundary using equation (2.33). $\mathcal{E}$ and Φ are computed analytically at the lateral boundaries (using the equilibrium profile and the Snell law). Then, $\mathcal{E}$ can be computed from the seaward boundary until the limiting water depth by the discretized version of equation (2.35).

$$\frac{\mathcal{E}_{ic,jc} - \mathcal{E}_{ic+1}(y_a)}{\Delta s} = \Phi_{i=ic}(y_b) \tag{2.36}$$

where y_a is the intersection of the wave ray at $ic+1$ and y_b is the intersection with $i = ic$ and Δs is the distance along the wave ray between the points y_a and (ic, jc) (figure 2.4). The previous version of the model was only capable of computing the wave height for positive incidence angles. The present version works for all wave incidence angles and, just as for the computation of θ, the angle at the offshore cell is evaluated to see which scheme should be used. It is essential that the scheme is consistent with the direction of the wave ray to avoid the introduction of numerical errors. A backward scheme is used in case of positive angles (figure 2.4),

$$\mathcal{E}_{ic+1}\,(ya) = \mathcal{E}_{ic+1,jc} - \frac{\mathcal{E}_{ic+1,jc} - \mathcal{E}_{ic+1,jc-1}}{\Delta y}\,(\Delta x \tan\theta)\,. \tag{2.37}$$

A forward scheme is used in case of negative angles,

$$\mathcal{E}_{ic+1}\,(ya) = \mathcal{E}_{ic+1,jc} + \frac{\mathcal{E}_{ic+1,jc+1} - \mathcal{E}_{ic+1,jc}}{\Delta y}\,(-\Delta x \tan\theta)\,. \tag{2.38}$$

A centered scheme is used in case of shore normal incidence,

$$\mathcal{E}_{ic+1}\,(ya) = \mathcal{E}_{ic+1,jc} - \frac{\mathcal{E}_{ic+1,jc+1} - \mathcal{E}_{ic+1,jc-1}}{2\Delta y}(\Delta x \tan\theta). \tag{2.39}$$

Finally, $\phi_{i=ic}\,(yb)$ can be computed with a centered scheme.

$$\Phi_{i=ic}\,(yb) = \Phi_{ic,jc-1} + \frac{\Phi_{ic,jc} - \Phi_{ic,jc-1}}{2\Delta y}\,(\Delta y - \Delta x \tan\theta)\,. \tag{2.40}$$

Because Φ is needed at the intersection of the wave ray with $i = ic$ (point y_b), the value of Φ is needed at the points $(i = ic, j = jc - 1)$ and $(i = ic, j = jc)$ (point a and b in figure 2.4). These values are obtained by computing the mean of the derivatives of the four surrounding points. Subsequently $\mathcal{E}(ic, jc)$ is computed with equation (2.36) and the wave height is obtained from equation (2.33).

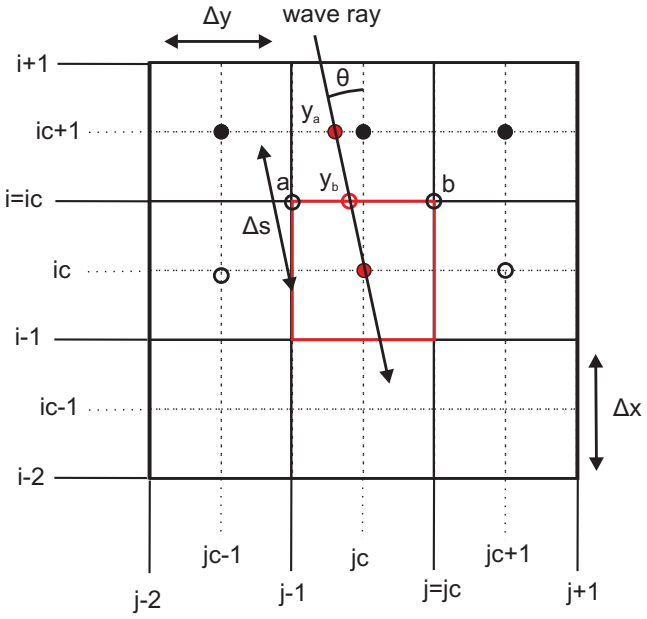

Figure 2.4: Example of the discretization of equation (2.36), which is used to determine the wave height. The unknown is $\mathcal{E}(ic, jc)$ (solid red dot). The wave angle is positive and a backward scheme is used to determine $\mathcal{E}_{ic+1}(y_a)$ (equation 2.37). $\Phi_{i=ic}(y_b)$ is determined by a centered scheme using points a and b (equation 2.40) and the value at these two points is computed as the mean of the derivatives of the four surrounding points.

For the computation of the wave height the domain is extended because the lateral boundary conditions lead to small gradients in H close to the boundary. This is caused by the small differences between the analytical solution at the boundary and the numerical solution in the rest of the domain. Due to the numerical scheme this effect at the boundary propagates in the direction of the waves while marching onshore. The amount of cells added at each lateral boundary, mx, is equal to the amount of cells between the offshore boundary and the limiting water depth. The bathymetry is extended by simply copying the profile at the lateral boundaries.

2.4.3.3 Limiting water depth

The wave field is computed up to a limiting water depth, with the related cross-shore position $ic = itol(jc)$,

$$D = \frac{0.8 H_b(jc)}{\gamma_b}. \tag{2.41}$$

Shoreward of this position ($ic < itol(jc)$) the seaward values are simply copied and ξ and $\mathcal{E}$ remain constant. If the bathymetric lines are not straight, $itol(jc)$ may not be

uniform in alongshore direction and it is possible that the value of ξ and $\mathcal{E}$ at $jc-1$ or $jc+1$ are not known (it is just a copied value). If the angle in the seaward cell is equal to zero and $ic < itol(jc-1)$ or $ic < itol(jc+1)$, a forward or backward scheme is used, respectively, instead of the centered scheme. If $ic < itol(jc-1)$ and $ic < itol(jc+1)$ the seaward value is simply copied. If the angle in the seaward cell is greater (backward scheme) or smaller (forward scheme) than zero and $ic < itol(jc-1)$ or $ic < itol(jc+1)$, respectively, the seaward value is simply copied.

2.4.3.4 Constraint on the grid

Since the wave propagation equations are of a hyperbolic type, it is required that a wave ray entering a cell from its offshore boundary does not exit trough a lateral boundary. This results in a constraint on the grid size, which is opposite to that based on shoreline angle (see section 2.4.2): $\Delta x/\Delta y < (\tan\theta)^{-1}$. It is numerically found that $\Delta x/\Delta y = 1$ can be used for $\theta_0 < 55^o$ and that $\Delta x/\Delta y = 0.25$ is safe up to $\theta_0 \simeq 89^o$.

Chapter 3

Formation of sand waves: random initial perturbations*

3.1 Introduction

In this chapter the spontaneous formation of sand waves due to high angle wave instability is studied. Small scale random perturbations were added to the initial rectilinear bathymetry. These initial conditions were chosen so that the system was not forced with a specific length-scale. The objective of this chapter is to find out to what extent the predictions of Ashton *et al.* (2001); Ashton & Murray (2006*a*) and Falqués & Calvete (2005) depend on their idealizations. It is expected that the current non-linear quasi 2D approach will provide new insight in the formation of sand waves due to shoreline instability. In particular, we look at the sensitivity to the wave incidence angle, the important role of cross-shore transport and the influence of wave height and period.

3.2 Setup of the default experiment

For the default experiment we used a 30 km long rectilinear coastline and constant wave conditions, $H_s = 1.41$ m, $\theta_0 = 60°$ and $T_p = 6$ s, which represent mean annual conditions that favor the development of HAWI. The size of the simulation domain was $L_x = 1.2$ km by $L_y = 30$ km, including a dry beach of 400 m width. A Dean-type profile was considered as the equilibrium profile:

$$Z(x) = -A((x+d)^{2/3} - d^{2/3}), \tag{3.1}$$

*This chapter is largely based on van den Berg *et al.* (2011*b*): van den Berg, N., Falqués, A. & Ribas, F. 2011b. Modelling large scale shoreline sand waves under oblique wave incidence. J. Geophys. Res. Under review.

Table 3.1: Parameter settings for the default experiment

H_s	offshore significant wave height	1.4 m
T_p	offshore peak wave period	6 s
θ_0	offshore wave angle	60°
γ_b	breaking index	0.5
ϵ_x	cross-shore diffusivity coefficient	0.05
ϵ_y	alongshore diffusivity coefficient	0.05
γ_s	swash zone diffusivity	0.001 $m^2 s^{-1}$
X_1	decay location cross-shore transport	$2X_b$
L_d	decay distance cross-shore transport	$0.5X_1$
Δx	cross-shore grid size	6 m
Δy	alongshore grid size	50 m
Δt	time step	0.001 days

where d introduces a small shift to avoid an infinite slope at the shoreline. The constants d and A were chosen by prescribing the swash slope ($\beta_s = 0.03$) and the water depth, $D_{ref} = 10$ m, at the offshore distance, $x_{ref} = 700$ m. The initial bathymetry was constructed as an alongshore repetition of this equilibrium profile. The resulting water depth at the offshore boundary was $D_0 = 10.9$ m so that, according to section 2.3.2, $\theta_0 = 60°$ is the maximum allowed wave angle for a wave period $T_p = 6$ s. Random perturbations with an amplitude of $|\Delta z_b| = 0.1$ m were superimposed on the initial bathymetry. The other parameters used for this experiment can be found in table 3.1. According to section 2.4.2, the maximum angle of the shoreline with respect to the y-axis allowed by the grid is about 13° ($\tan \phi_s = 2\Delta x/\Delta y = 0.24$, i.e. $\phi_s = 13°$).

3.3 Shoreline evolution of the default experiment

The initial random perturbations in the bathymetry caused small fluctuations in the shoreline position at $t = 0$ with an amplitude of about 0.5 m (figure 3.1 left panel). This is the result of the linear interpolation between the last dry cell and the first wet cell, which is used to determine the shoreline position. A Fourier analysis of the shoreline, $x_s(y, t)$, provides more information on the alongshore length scales involved in the evolution of the perturbations. The initial shoreline showed a low spectral density, spread over all length scales (figure 3.1 right panel).

During the first simulation days the small scale noise in the bathymetry got smoothed out and shoreline fluctuations with a small amplitude (1 m) but larger alongshore length scale (1 km) developed. This does not represent a physical process as the model is not capable of describing morphodynamics at this small scale and it can be considered as a numerical way of generating random perturbations at a larger length scale. After this larger length scale was reached, the simulation realistically described the morphodynamics. From this moment on the undulations amplified non uniformly. When the spacing between adjacent crests or troughs was larger, the corresponding shoreline undulation developed faster. After 25 days a clear spectral peak developed at $\lambda = 2$ km and after one year wavelengths between 3 and 4 km became dominant and the amplitude of the undulations increased to about 3 m (figure 3.1).

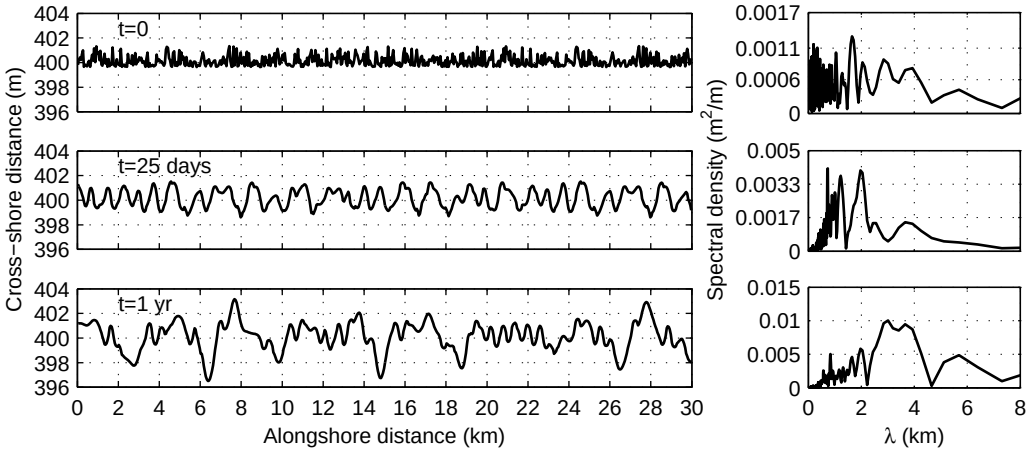

Figure 3.1: Shoreline evolution for the default experiment during the first year, showing the initial development of shoreline instability (left panels) and the corresponding Fourier analysis of the shoreline (right panels). The waves come from the left in the plot and the cross-shore distance is exaggerated by a factor of 600.

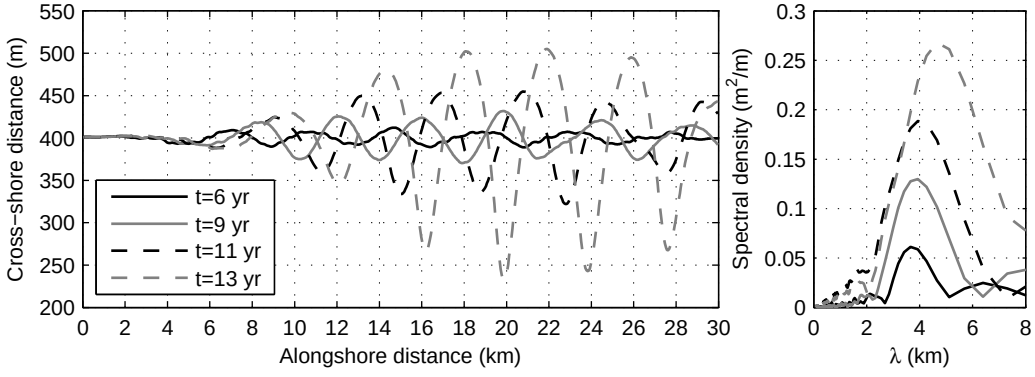

Figure 3.2: Shoreline evolution between 6 and 13 years, showing the growth and migration of a regular sand wave field (left panel) and the corresponding Fourier analysis of the shorelines (right panel). The waves come from the left and the cross-shore distance is exaggerated by a factor of 40.

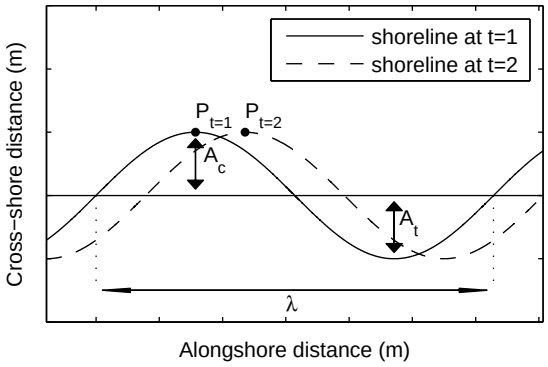

Figure 3.3: Definition sketch of a shoreline sand wave, where A_c is the amplitude of the crest, A_t is the amplitude of the trough, λ is the wavelength and P_t is the position of the crest. The mean amplitude is $\bar{A} = (A_c + A_t)/2$ and the migration celerity is $v = (P_{t=2} - P_{t=1})/\triangle t$.

During the following years these undulations developed into a regular sand wave field (figure 3.2 left panel). In order to quantify the dimensions and evolution of the sand waves we use the definitions presented in figure 3.3. The growth rate of the amplitude of the largest sand wave, σ can be estimated by assuming an exponential growth. The slope of a linear fit of $\log(\bar{A}(t)/\bar{A}(0))$ plotted against t gives σ (yr^{-1}). At $t = 6$ yr, six sand waves were present within the domain with a mean amplitude, $\bar{A}$, of about 9 m. Although the small scale undulations were still present they did not grow further and a wavelength of about 3.6 km became dominant. This length scale is similar to the lower range of the predictions by Falqués & Calvete (2005) ($\lambda = 4-15$ km). The other shorelines in the left panel of figure 3.2 show the growth and migration of the sand waves until $t = 13$ yr and the right panel shows the corresponding Fourier analysis of the shorelines. The amplitude of the sand waves increased until 121 m at a growth rate of about 0.36 yr^{-1}. Consistently the spectral density increased and at the same time the peak moved to $\lambda = 4.6$ km. The latter illustrates the slow increase of the wavelength of the sand waves. The sand waves migrated downdrift at a rate of about 550 m/yr. Figure 3.4 shows the corresponding bathymetry at $t = 13$ yr. The shoreline undulations extended into the bathymetry up to a depth of about 8 m and the fully developed sand waves tended to be slightly asymmetric in shape, so that the angle between the bathymetric lines and the mean shoreline was larger at the downdrift slope of the crest. Interestingly the sand wave at the updrift side of the sand wave field (located at about $y = 10$ km for $t = 13$ yr) developed much slower. Its amplitude merely increased from 21 m until 42 m ($\sigma = 0.24$ yr^{-1}), its wavelength was longer (5 km) and its migration celerity was lower (340 m/yr).

Eventually all the sand waves would propagate downdrift and if no new bathymetric perturbations are introduced, the stable boundary condition would lead to a rectilinear bathymetry. This was already the case for the first four kilometres of the domain. However, the limitation on the shoreline angle, $|\phi_s| \leq 2\Delta x/\Delta y \sim 13°$, was exceeded after approximately $t = 13$ yr. After this, the predictions of the model were not reliable.

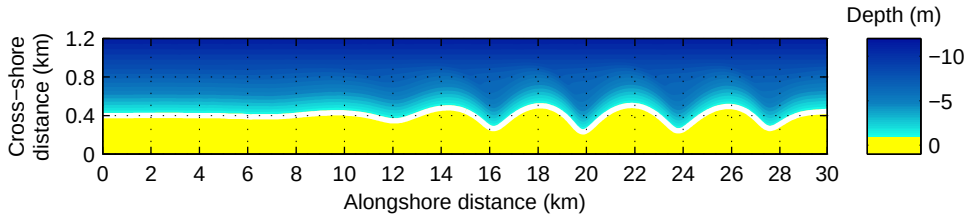

Figure 3.4: Contour plot for the default experiment showing the bathymetry after 13 years. The cross-shore distance is exaggerated by a factor of 4 and the waves come from the left.

3.4 Sensitivity to wave incidence angle

The maximum realistic offshore wave angle of 60° was used in the default simulation. In this section we look at the sensitivity of the results to the offshore wave angle. To this end, simulations were done with $\theta_0 = 0°, 20°, 40°$, 50° and 55°. After 13 simulation years the shoreline for $\theta_0 = 0$ and $\theta_0 = 20°$ became straight and the bathymetric perturbations simply diffused. For $\theta_0 = 40°$, the diffusion rate was lower and a few small undulations of about 0.5 m remained from the initial noise. The behavior changed for $\theta_0 = 50°$. The initial perturbations grew and formed small undulations of about 1.5 m amplitude with a wavelength between 3 and 4 km (figure 3.5 top panel). For $\theta_0 = 55°$ undulations developed with $\bar{A} = 8$ m and $\lambda = 4.5$ km, in contrast to the default simulation where $\bar{A}$ reached 121 m (see figure 3.2 bottom panel). It therefore seems that instability develops around $\theta_0 = 50°$ and that the growth rate increases rapidly with the wave angle. To confirm this we look at longer simulations with $\theta_0 = 50°$ and 55° and, after about 30 years, the amplitude of the latter simulation reached about the same magnitude as in the default simulation. The growth rate was 0.17 yr^{-1} compared to 0.36 yr^{-1} for the default simulation and the migration celerity was lower, at about 365 m/yr. The simulation with $\theta_0 = 50°$ seems to really be on the limit of instability because the sand waves were consistent but hardly grew in amplitude. Even after 70 simulation years the amplitude was only about 7 m. During these years the small amplitude sand waves showed a complex behavior of migration and merging and eventually $\lambda = 10$ km became dominant.

Notice that we have been looking at the wave incidence angle at the offshore boundary, where the water depth is $D = 10.9$ m. As will be discussed in next section, the relevant angle for HAWI is the angle at the depth of closure. According to the offshore extent of the bathymetric signal of the sand waves in the default experiment, we can assume that the depth of closure was about 8 m. For $\theta_0 = 50°, 55°$ and 60° the angle at the depth of closure was about 44°, 48° and 52°, respectively. The first value is very close to the critical angle of 42° found by Ashton *et al.* (2001) and this can explain why the instability developed around $\theta_0 = 50°$.

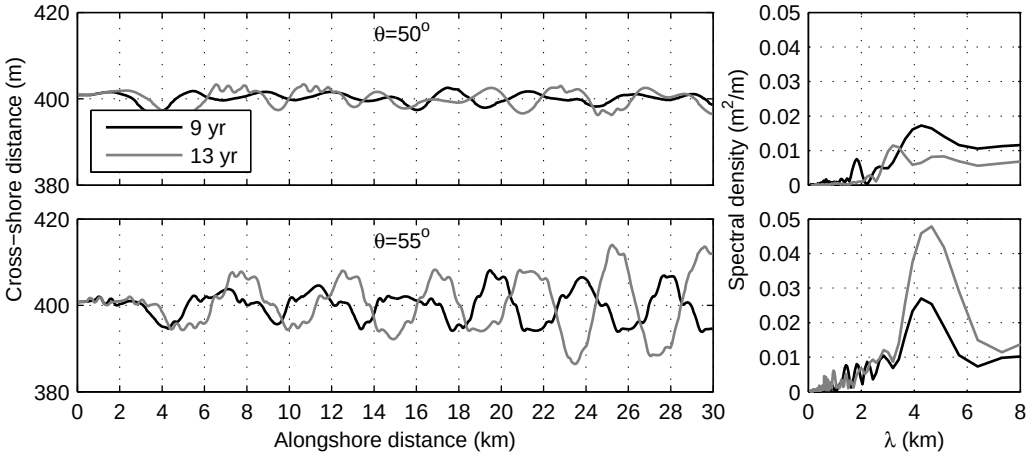

Figure 3.5: The shoreline at $t = 9$ and 13 yr for $\theta_0 = 50°$ and $55°$ (left panels) with the corresponding Fourier analysis of the shorelines (right panels). The shorelines can be compared to the default experiment with $\theta_0 = 60°$ in figure 3.2.

3.5 Role of the cross-shore transport and a criterion for HAWI

In the Q2D-morfo model the cross-shore transport is represented by a diffusive transport that drives the cross-shore profile to the equilibrium profile. The cross-shore transport redistributes sediment between the dry beach, the surfzone and the shoaling zone and it is mainly governed by the non-dimensional coefficient ϵ_x. This coefficient defines the magnitude of the diffusivity between the shoreline and the distance X_1, where the diffusivity sharply drops to a very small residual value. To investigate how cross-shore transport affects the instability, two series of experiments were done.

In the first series of experiments, the effect of ϵ_x was investigated. Because the value $\Delta t = 0.001$ days of the default experiment was already close to the Courant stability condition, Δt had to be reduced for higher values of ϵ_x. The shoreline instability developed faster with increasing cross-shore diffusivity, i.e. for a faster adaptation of the cross-shore profile. The values $\epsilon_x = 0.01, 0.05$ (default) and 0.2 resulted in a growth rate of $\sigma = 0.22, 0.36$ and 0.46 yr^{-1} respectively. Just as for the exploration of the sensitivity to the wave incidence angle, the migration celerity increased with the growth rate. A very high value of ϵ_x would be equivalent to an instantaneous adaptation of the profile as used in previous studies and this would lead to an overestimation of the growth rate and the migration celerity of the shoreline sand waves.

In the second series of experiments, the influence of the offshore extension of the cross-shore diffusivity profile was examined. The diffusivity profiles corresponding to different values of the ratio X_1/X_b can be seen in figure 3.6a. The growth rate of the largest

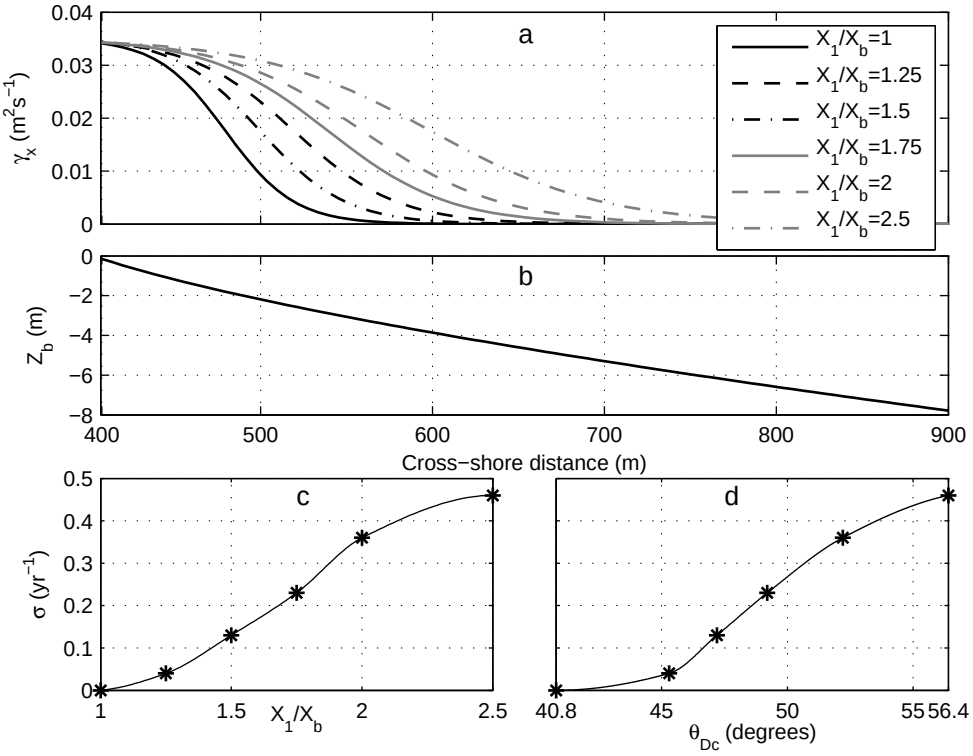

Figure 3.6: (a) Cross-shore diffusivity profiles as a function of X_1/X_b ratio, (b) equilibrium beach profile, (c) Growth rate of the shoreline sand waves as a function of X_1/X_b and (d) growth rate as a function of the wave angle at the depth of closure corresponding to each diffusivity profile.

sand wave is also plotted as a function of X_1/X_b. For $X_1/X_b = 1$ only some irregular small scale undulations remained from the initial perturbations and no instability seemed to develop (after 27 simulated years). For an increasing offshore extension, instability developed and the growth rate of the sand waves increased with X_1/X_b (figure 3.6c).

The offshore extension of the cross-shore diffusivity profile can be related to the depth of closure, D_c, because the ratio X_1/X_b determines the depth at which the cross-shore diffusivity becomes negligible and almost no sediment transport occurs. The default experiment with $X_1/X_b = 2$ showed that almost no transport took place below about 8 m water depth. The diffusivity at this point was a factor 10^4 smaller than the value close to the shoreline and we use this as a criterion for D_c. With this criterion, D_c was determined for the different values of X_1/X_b and it ranged between 4.7 and 9.4 m. The wave incidence angle at these depths, θ_{Dc}, could be determined and the growth rate was plotted as a function of θ_{Dc} (figure 3.6d). It is enlightening to see that the growth rate starts to increase around 45°. It therefore seems that the critical angle required for instability should be evaluated at the depth of closure (i.e. at the most offshore extent

of the bathymetric perturbation) and not in deep water as suggested by Ashton *et al.* (2001) nor at breaking as has been considered in traditional literature. This is in line with the exploration of the wave incidence angle in section 3.4 and with previous studies by Falqués & Calvete (2005); Uguccioni *et al.* (2006); List & Ashton (2007), who recognized that waves must be above a critical angle at the most offshore extent of the perturbed depth contours for HAWI to occur. Of course there is some uncertainty in this criterion because the determination of D_c is not exact. Moreover, this criterion depends on the beach conditions and the alongshore transport formula used in the model.

3.6 Sensitivity to wave height and period

Results from numerical experiments with different values for H_s and T_p suggest that shoreline instability is stronger for increasing wave height and for decreasing wave period. This is the result of at least three different effects.

First, instability depends on the wave angle at the depth of closure, θ_{Dc} and both an increase in wave height and a decrease in wave period lead to larger θ_{Dc}, hence to stronger instability. Wave refraction from deep water to nearshore is less intense for small wave periods so that θ_{Dc} is larger. In case of larger wave heights, D_c increases so that there is less refraction from deep water to D_c with the result that θ_{Dc} is larger. These simple physics can be used to derive a non-dimensional parameter that approximately governs the dependence of HAWI on H_s and T_p. This parameter should express the ratio between H_s and T_p that is required to keep θ_{Dc} constant for a given θ_∞. Applying the Snell Law between deep water and D_c shows that a fix ratio between θ_∞ and θ_{Dc}, requires a constant ratio k_{Dc}/k_∞. From the dispersion relation we have,

$$\frac{4\pi^2}{T_p^2} = gk_{Dc}\tanh(k_{Dc}D_c) = gk_\infty.\tanh(k_\infty D_\infty) \simeq gk_\infty \tag{3.2}$$

This means that a fixed ratio k_{Dc}/k_∞ implies that $k_{Dc}D_c$ is constant. After multiplying the left equality in equation (3.2) by D_c it follows that D_c/T_p^2 must be constant. By assuming that D_c is roughly proportional to H_s and after dividing by g to make it non-dimensional, we conclude that θ_{Dc} is approximately constant if H_s and T_p vary while H_s/gT_p^2 is constant. This parameter should govern the strength of HAWI, with larger values leading to a stronger instability. In order to validate the relation between this parameter and HAWI, the growth rate of the sand waves was plotted as a function of H_s/gT_p^2 and it resulted into a reasonable correlation ($R^2 = 0.84$, not shown). Because of the large amount of simulations the growth rate was computed here by using the root mean square shoreline deviation (σ_δ) instead of the amplitude of the largest sand wave.

Second, H_s has a direct effect on the strength of the instability. For higher waves there is more energy available and a potential instability would develop faster. According to the CERC formula (2.3), the sediment transport rate, Q, increases with $H_b^{2.5}$ so that by applying the one-line sediment conservation (equation 1.1), the time evolution should also increase with a factor $H_b^{2.5}$. However, D_c also increases with H_s and if we roughly

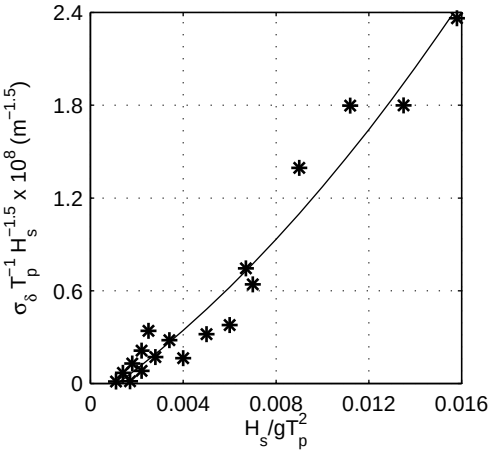

Figure 3.7: The initial growth rate of the shoreline sand waves (σ_δ), scaled with $T_p H_s^{1.5}$, as a function of H_s/gT_p^2. The solid line is a second order polynomial fit with $R^2 = 0.96$.

assume a linear relationship between D_c and H_s, the growth rate should be scaled with $H_s^{1.5}$. After performing this scaling, the correlation between σ_δ and H_s/gT_p^2 increased ($R^2 = 0.91$, not shown).

Finally, T_p also has a direct effect on the strength of the instability. The instability is a result of alongshore gradients in wave height produced by the differences in energy spreading between the updrift and the downdrift sides of a sand wave. The dependence of wave energy spreading on shoreline orientation is more pronounced for increasing wave period (Falqués, 2003). Therefore, for a given angle at the depth of closure, θ_{Dc}, i.e., for a given value of H_s/gT_p^2, large wave periods should result into a stronger instability. This effect can be taken into account by rescaling the growth rates with a power of T_p. Figure 3.7 shows $\sigma_\delta \, T_p^{-1} H_s^{-1.5}$ as a function of H_s/gT_p^2. This later dependance shows the best correlation with $R^2 = 0.96$.

Summarizing, the instability depends on H_s and T_p in a complex manner through at least three processes: i) refraction up to the depth of closure, governed by H_s/gT_s^2, ii) accelerated dynamics for increasing wave energy and iii) stronger dependence of wave energy spreading on shoreline orientation in case of high wave periods. Since the polynomial fit in figure 3.7 is almost linear, we simplify the dependence as $\sigma_\delta \sim H_s^{2.5}/T_p$. Notice, that this dependence has been obtained for a particular wave angle at the offshore boundary, $\theta_0 = 60°$, and a particular cross-shore profile.

Falqués & Calvete (2005) found with their linear approach that relatively short and low waves favored instability. The effect of T_p in that study is similar to the dominant effect of T_p described in the present study (see point i above). The effect of H_s on shoreline instability is however opposite to the findings of the present study. This discrepancy comes from the fact that Falqués & Calvete (2005) used a fixed value for D_c, which was independent of H_s, and the perturbation always extended up to this depth. Therefore,

θ_{Dc} was independent on H_s and low values of H_s merely led to a smaller depth of breaking and therefore a longer distance over which the waves shoaled and refracted, which favored instability. However, for predictions on a long time scale (assuming average wave conditions with a constant value for H_s), it seems more reasonable to assume that D_c depends on H_s and therefore the effect of H_s described in the present study seems more appropriate. Ashton & Murray (2006*a*) wrote that H_s and T_p have little effect on the occurrence of shoreline instability and only play a role in the time scaling. This is a consequence of their assumption that the perturbations reach into the bathymetry up to the wave base and the fact that they do not take into account the curvature of the bathymetric lines. The present study shows that H_s and T_p do not only effect the time scaling but that together with θ_0 they determine if instability can occur.

3.7 Sensitivity to numerics and boundary conditions

Several tests have been done to assess the sensitivity to the numerical parameters and to check the reliability of the discretization. Results were almost insensitive to changes in Δt, Δt_w and Δx. In contrast, they were quite sensitive to changes in Δy. Changing from $\Delta y = 50$ m to $\Delta y = 25$ m, however, had an acceptable small effect and therefore $\Delta y = 50$ m was chosen as a compromise between accuracy and computational cost.

The default simulation has was also carried out with the parameter $r = 0$ in equation (2.3). This sets the second term that was added to the CERC formula to zero. This showed that this term had little effect on the shoreline evolution, with only a small difference in amplitude and migration rate. Without further investigation on the role of this term and calibration with field data it is recommended to simply not include this term in future applications of the model (see also List *et al.*, 2008).

The model has been developed to describe shoreline sand wave formation and propagation along an open unbounded coast. Since the computation domain is necessarily bounded, a sensitivity analysis with respect to the boundary conditions is highly recommended. Experiments were done with the wave conditions of the default experiment ($\theta_0 = 60°$, $H_s = 1.4$ m and $T_p = 6$ s) and with initial random perturbations only between 5 km $\leq y \leq$ 25 km for four different domains: A) 5 km $\leq y \leq$ 25 km, B) $0 \leq y \leq$ 25 km, C) 5 km $\leq y \leq$ 30 km, D)$0 \leq y \leq$ 30 km. Simulation A is similar to the default experiment and for B,C and D the bathymetry is extended without perturbations updrift, downdrift and on both sides respectively. The simulations are compared at $t = 10$ yr. As can be seen in figure 3.8, simulations A and C led to an almost identical shoreline in the central stretch, 5 km $\leq y \leq$ 25 km. The same can be observed for simulations B and D and this shows that extending the domain downdrift did not affect the sand wave growth and propagation. The sand waves traversed freely the downdrift boundary and behaved as they would for an unbounded open coast. However, extending the domain updrift resulted into quite significant differences (compare simulations A/C with B/D). The differences were smaller at the downdrift side of the domain and the wavelength and the overall qualitative behaviour was similar. An explanation for the influence of the updrift boundary on the shoreline evolution can be the following. Adding a section

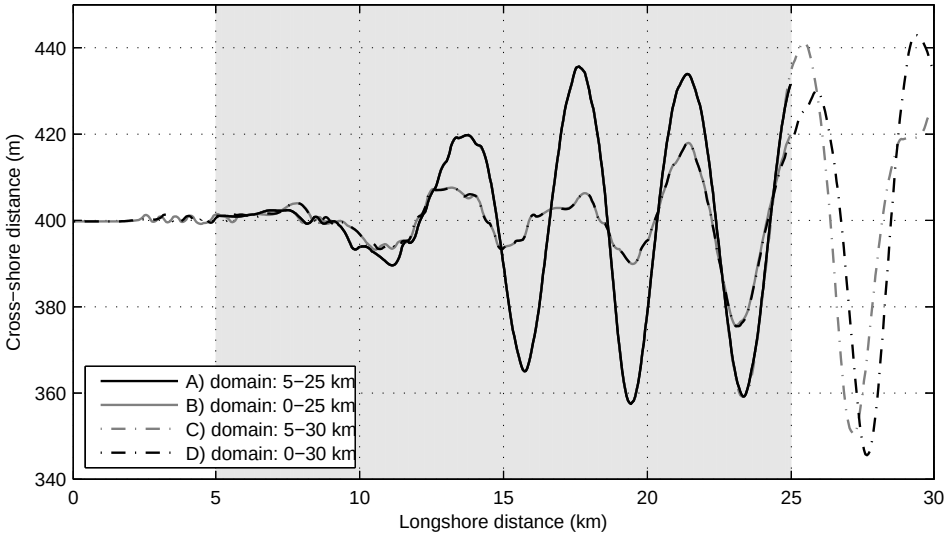

Figure 3.8: Sensitivity to the size of the computational domain for $t = 10$ yr. Initial random perturbations were only added in the central stretch, 5 km $\leq y \leq$ 25 km, indicated with gray overlay.

without random perturbations at the updrift side can be considered as using different initial perturbations. At the transition between the clean and perturbed bathymetry the average surf zone orientation is determined within a rectangle. This changes the initial small scale shoreline undulations in the left of the domain because the perturbations are smoothed out and leads to a different evolution of the emerging sand waves. This effect does not play a role for a downdrift extension of the domain because the perturbations propagate downdrift and leave the domain.

3.8 Conclusions

A quasi 2D morphodynamic model for large scale shoreline dynamics was used to study shoreline instability and the spontaneous formation of shoreline sand waves.

Simulations with constant high angle wave incidence show that shoreline sand waves can develop in unison from small random perturbations on a rectilinear coastline. Consistently with the modeling studies of Ashton *et al.* (2001) and Falqués & Calvete (2005), the minimum incidence angle that led to high angle wave instability was about 42° but it is shown here that this angle is required at the depth of closure (i.e., the most offshore reach of shoreline perturbations) and not at deep water. The refinement of this criterion reduces the potential for the occurrence of high angle wave instability on natural coasts.

The growth rate of the shoreline sand waves increased strongly with angles above the threshold value and instability was favored by a mean wave climate with high waves and short wave periods, with the growth rate being roughly proportional to $H_s^{2.5}/T_p^{-1}$. This is in contrast to Falqués (2006), who found with their linear approach that instability was favored by low wave height.

In the numerical experiments shoreline sand waves developed with wavelengths between 2 and 5 km. These values are similar to the lower end of the range of length scales predicted by Falqués (2006) (4-15 km). The time scale for the sand wave formation was in the order of several years. The amplitude of the sand waves increased exponentially due to the positive feedback between morphological changes and the wave field. After 13 simulated years the amplitude reached up to 121 m and the sand waves migrated downdrift at a rate of about 0.5 km/yr.

Cross-shore dynamics play an important role in the feedback between shoreline perturbations and the wave field. It determines if a perturbation reaches into the bathymetry up to a depth where the wave angle is greater than the threshold value. The assumption that perturbations extend into the bathymetry up to deep water (Ashton *et al.*, 2001) therefore leads to an overestimation of the potential for shoreline instability. Simulations showed that faster cross-shore dynamics led to higher growth rates.

Chapter 4

Formation of sand waves: localized initial perturbation

4.1 Introduction

Various studies suggest that the presence of shoreline sand waves is related to a large (periodic) input of sediment, e.g. the discharge of river sediments (Inman, 1987), the periodic inlet opening (Thevenot & Kraus, 1995), the artificial injection of a large quantity of sand (Grove *et al.*, 1987) and the welding of shoals or oblique bars on to the shore (Davidson-Arnott & van Heyningen, 2003). It is expected that these large scale perturbations are very efficient in triggering shoreline instability. Even if the instability is weak, the large scale perturbations would maintain their volume and migrate downdrift. This could explain why most observations of shoreline sand waves are on coast where a large periodic input of sediment is present. Traditional shoreline models are unable to predict the persistence or growth of these large scale perturbations and they can only describe downdrift migration by including an empirical advection term (Dean, 2002; Larson & Kraus, 1991; Thevenot & Kraus, 1995). In this chapter we study the effect of HAWI on a rectilinear coast with a localized large scale shoreline perturbation. Special attention is payed to the implications of HAWI for shore nourishment.

4.2 Setup of the default experiment

The simulations were set up similar to the simulation with random perturbations in the previous chapter (see section 3.1), using a constant offshore wave incidence $\theta_0 = 60$. A Gaussian shaped perturbation with an alongshore width of about 2 km was added to the initial rectilinear coastline at the 5 km alongshore position (figure 4.1a). The

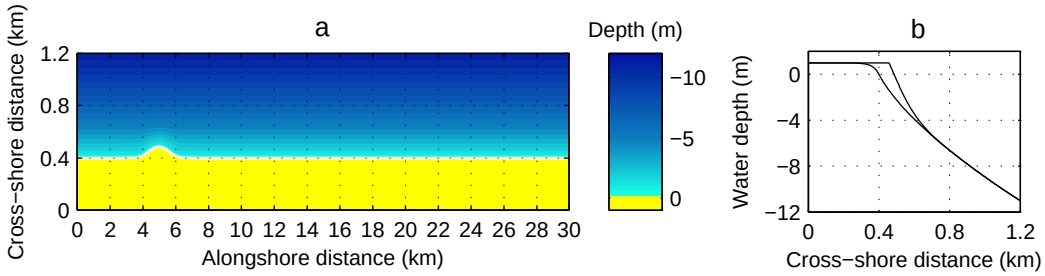

Figure 4.1: (a) The initial bathymetry of the default simulation with a Gaussian shaped perturbation at the 5 km position. Notice that the cross-shore distance in the bathymetric plot is exaggerated by a factor 8. (b) The cross-shore equilibrium profile and the cross-shore profile at the 5 km position showing the perturbation.

alongshore width was determined at a tenth of the maximum amplitude of the Gaussian. The cross-shore shape of the perturbation can be seen in figure (figure 4.1b). It advances the shoreline about 85 m at the crest and the perturbation reaches into the bathymetric lines until a depth of about 5 m. The cross-shore slope at the crest of the perturbation is steeper than the equilibrium slope. The mean slope from the shoreline to the foot of the perturbation is 0.027, compared to 0.018 for the equilibrium profile. The perturbation has a volume of about 0.7 Mm^3.

4.3 Shoreline evolution of the default experiment

4.3.1 Initial evolution of the perturbation

During the first month, the perturbation diffused rapidly, mainly in the cross-shore direction (figure 4.2). Sand was transported from the upper to the lower part of the profile and the shoreline retreated about 40 m. The perturbation maintained more or less the same amplitude during the following 2 years. During this period the perturbation migrated downdrift at a rate of 600 m/yr and became more asymmetrical. The transition from the initial strong diffusion to migration implies that HAWI already played a role and this is plausible because after 1 month the foot of the perturbation reached a depth of 6 m where the incidence angle was close to the critical angle of about 45° (see section 3.5. Even though the amplitude of the undulation at the shoreline did not increase during these 2 years, it got spread further offshore in the bathymetry until the actual depth of closure of about 8 m was reached where $\theta = 52°$ (figure 4.2b). The cross-shore profile reached a new equilibrium and from this moment on a net input of sediment caused an offshore shift of the whole profile, leading to an increase in amplitude of the shoreline undulation and strengthening of the HAWI.

Downdrift of the perturbation, an erosional zone (trough) started to developed after

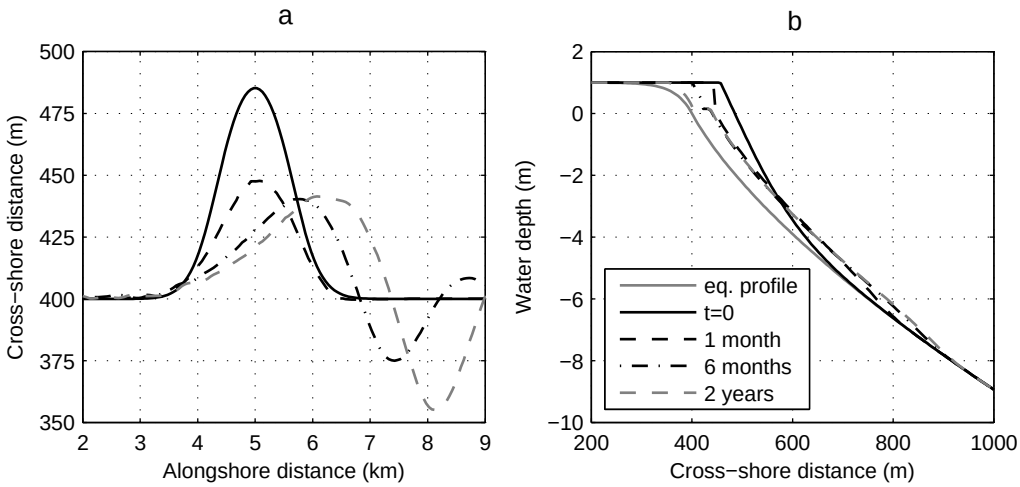

Figure 4.2: The initial evolution of the Gaussian shaped perturbation: (a) the shoreline position and (b) the cross-shore profile.

2 months. It grew during the first 2 years until an amplitude of 42 m (figure 4.2a). Together with the erosional zone the perturbation can be seen as a single shoreline sand wave with a wavelength of about 5 km. The development of a downdrift erosional zone is consistent with the study of Inman (1987).

4.3.2 Spatial-temporal instability

Figure 4.3 shows the evolution of the shoreline over a period of 9 years. It can be seen that the initial perturbation migrated further downdrift and grew in amplitude. Intriguingly, a series of sand waves formed downdrift of the initial single sand wave. These sand waves did not grow in unison from small scale perturbations but were triggered by the initial sand wave. Downdrift of the trough of the first sand wave, sediment was deposited and a new perturbation grew. This perturbation developed into a second sand wave and so on. Each new sand wave developed with a initial wavelength of about 2 km. The growth of the sand wave field in this simulation can be seen as spatial-temporal instability, i.e., the growth of a perturbation in both space and time. This is a well known process in fluid dynamics but spatial-temporal instabilities have, to the author's knowledge, not been described previously in coastal morphodynamics. An example from river morphodynamics can be found in Federici & Seminara (2003), who studied the generation of large scale bedforms in rivers.

The formation of this spatial-temporal instability was the result of a chain reaction in the alongshore transport. The first erosional zone developed as a result of a positive transport gradient downdrift of the perturbation, where the relatively low transport rate at the downdrift slope increased to normal values for a rectilinear coastline. The growth

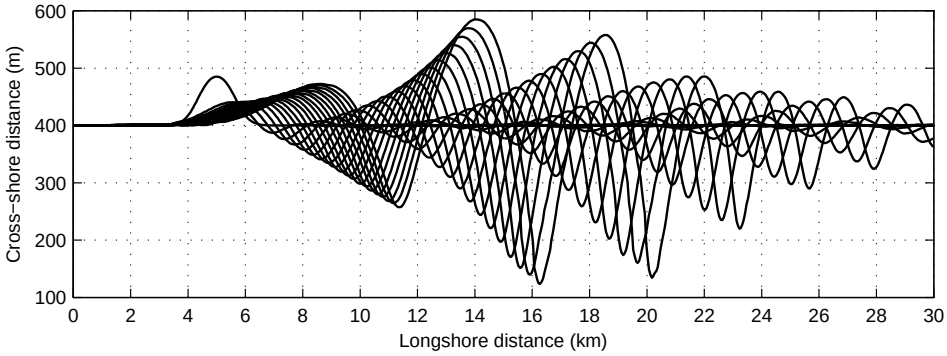

Figure 4.3: Time evolution of the shoreline for a rectilinear coast with a Gaussian shaped perturbation at 5 km for default conditions ($\theta_0 = 60°$). The shoreline is plotted every 6 months and the final shoreline corresponds with the result after 9 years. Notice that the cross-shore distance is exaggerated by a factor 20.

of this trough was enhanced by wave focusing on the downdrift slope of the trough. As a result, the transport rate increased above normal values, resulting in a negative gradient downdrift of the trough. This led to deposition and the gradual growth of a new perturbation. This chain-reaction continued and after 9 years a train of 6 sand waves developed with wavelengths between 2.3 and 7.5 km and mean amplitudes between 60 and 220 m (see table 4.1 and figure 4.3). The limitation on the shoreline angle was exceeded after these 9 years (see section 2.4.2).

The differences between the various sand waves can not only be attributed to the fact that the downdrift sand waves were younger, there were also differences in their dynamics. Table 4.1 shows the initial growth rate of the sand waves (determined for the first 3 years of the development of each sand wave). The initial growth rate of the first sand wave was relatively low and the 3^{rd} until the 6^{th} sand wave had similar initial growth rates. Very interesting is the fact that the amplitude of the first 3 sand waves continued to increase and that the amplitude of the crest of the 4^{th} until the 6^{th} sand wave seemed to stabilize at $60 - 80$ m. The table also shows that the migration rate increased until the 4^{th} sand wave and that the 4^{th} until the 6^{th} sand wave migrated at more or less the same rate. The increase in migration rate until the 4^{th} sand wave enabled the wavelength of the first 3 sand waves to increase gradually. Consistently the wavelength of the 4^{th} until the 6^{th} sand wave remained more or less constant around 2.5 km.

Just as in the previous chapter, the first sand wave had a relatively low growth and migration rate. It seems that the dynamics of the first sand wave is influenced by the rectilinear updrift bathymetry and that its more static behaviour works as an 'anchor' on the sand wave field. The sand waves, that formed due to the spatial-temporal instability, initially developed at a similar length scale and at similar growth rates. At longer time scales, non-linear effects became important. The sand waves became more asymmetrical and the troughs grew faster than the crests. The first sand waves of the train were

Table 4.1: Characteristics of the sand wave train that developed from an initial Gaussian shaped perturbation on a rectilinear coast for default conditions. The sand waves are numbered in downdrift direction (left to right).

sand wave	t_{form} (yr)*	σ (yr^{-1})***	λ_{form} (km)	$\lambda_{t=9}$ (km)	$\bar{A}_{t=9}$ (m)	$\bar{v}$ (m/yr)
1	2**	0.16	5	7.5	106	334
2	0.5	0.79	2	5	220	618
3	1.5	0.93	2	3.7	197	903
4	3	0.89	2	2.7	131	1058
5	4	0.85	2	2.3	83	1022
6	5	0.94	2	2.3	60	1080

* The time at which the sand wave formed and started to grow.
** The first sand wave formed directly from the initial perturbation but only after 2 years the crest started to grow.
*** The initial growth rate of each sand wave, determined over 3 years after t_{form}.

influenced by the 'anchor effect'. They migrated slower, their wavelength increased and their amplitude continued to increase. The sand waves further downdrift in the train behaved more uniformly and it seems that some equilibrium state was approached in which the sand waves migrated downdrift without a further increase in amplitude or wavelength.

4.4 Sensitivity to wave incidence angle

Simulations were done with $\theta_0 = 0°, 20°, 40°, 50°$ and $55°$. For $\theta_0 = 55°$ the initial localized perturbation led to the development of a sand wave field, similar to the default simulation (see section 4.3). However, the growth rates of the initial perturbation and the downdrift sand waves were much lower (a factor 2 to 3). After 9 simulation years the mean amplitude of the largest sand wave was only 49 m compared to 220 m for the default simulation. The migration rate was also lower (up to a factor 2) but the wavelength of the sand waves was similar to the default simulation.

For $\theta_0 = 50°$ the initial perturbation did not show a transition to growth and it continued to diffuse. The diffusion rate was however very low and therefore the initial perturbation maintained an amplitude of about 20 m while it migrated downdrift. The spatial-temporal instability developed very slowly. Figure 4.4 shows the evolution of this simulation over 20 years. The perturbation migrated 3.2 km and still had an amplitude of 18 m. The two downdrift sand waves had a amplitude of 13 and 6 m with a wavelength of 5.7 and 4.8 km respectively. In section 3.4 it was shown that for $\theta_0 = 50°$ the angle at the depth of closure was close to the critical angle and this explains the very mild shoreline instability.

For $\theta_0 = 40°$ the initial perturbation diffused faster and instead of migrating downdrift it only developed a planform asymmetry, with a steeper downdrift slope. After the strong initial diffusion in cross-shore direction, the diffusion was dominated by the alongshore transport and the diffusion slowed down as it is proportional to its amplitude. After 9

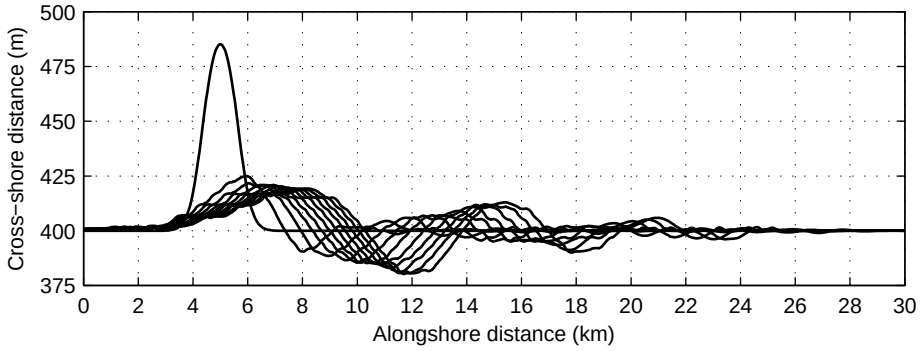

Figure 4.4: Time evolution of the shoreline for a rectilinear coast with a Gaussian shaped perturbation at 5 km for $\theta_0 = 50°$. The shoreline is plotted every 2 years and the final shoreline corresponds with the result after 20 years. Notice that the cross-shore distance is exaggerated by a factor 80.

years, the amplitude was only 9 m and no downdrift erosional zone or spatial-temporal instability developed. For $\theta_0 = 0°$ and $20°$ the diffusion rate was higher and the initial perturbation remained symmetrical.

4.5 Sensitivity to the dimensions of the perturbation

Various simulations were carried out to study the sensitivity to the width and the amplitude of the Gaussian shaped perturbation. Simulations with a width of 1 and 4 km showed that the initial diffusion of the perturbation was greater for a small width and that the transition period until growth was longer for a small width. This was the result of a relatively stronger alongshore diffusion. The difference in amplitude at moment the perturbations started to grow, resulted in different amplitudes after 9 years (figure 4.5). The growth rates of the first crest were however similar to that of the default simulation. In contrast, a perturbation with a width of 0.5 km diffused until a 10 m amplitude and, even though the wavelength of the resulting undulation increased, the crest did not show a transition to growth. All the simulations showed the development of a sand wave train. There were some differences in the growth rate of the first erosional zone and this caused differences in the downdrift sand waves. The self-organized behaviour of the sand wave train was however similar to the default simulation and the sand waves developed with similar wavelengths.

Simulations with a perturbation with an amplitude of 53 and 112 m (cross-shore extent until a 3 and 8 m water depth respectively) showed that the transition from diffusion to growth was shorter for a perturbation with a bigger amplitude and that the growth rate of the perturbation increased slightly. A bigger amplitude led to a faster development of the first erosional zone and higher growth rates for the spatial-temporal

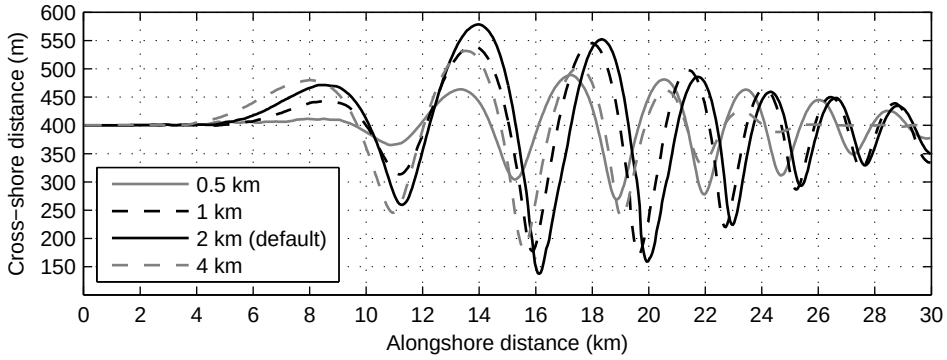

Figure 4.5: The shoreline after 9 years for default conditions and a rectilinear coast with an initial Gaussian shaped perturbation of different alongshore widths. Notice that the cross-shore distance is exaggerated by a factor 20.

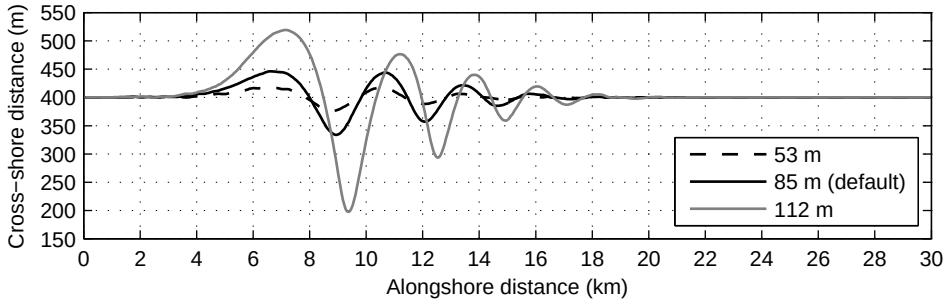

Figure 4.6: The shoreline after 3.5 years for default conditions and a rectilinear coast with an initial Gaussian shaped perturbation of different amplitudes. Notice that the cross-shore distance is exaggerated by a factor 20.

instability (figure 4.6). The simulation with a 112 m amplitude already approached the limitation on the shoreline angle after 3.5 years.

4.6 Implications to shore nourishment

Shore nourishment is a widely applied engineering approach to mitigate beach erosion and it involves the introduction of large quantities of sand to the beach system. It is considered a 'soft' engineering solution which, in general, has less negative side effects on adjacent beaches than coastal structures such as groins and breakwaters. The introduced sand becomes part of the beach system and the shore nourishment is merely a temporal

solution because it is considered to eventually diffuse. Shoreline variability induced by migrating undulations should be taken into account in nourishment planning because the variability might be greater than the long term trend (Stive *et al.*, 2002). Erosional zones on a coast might be related to these undulations and the resulting narrower beach width could increase the vulnerability of the dunes to erosion and breaching (Ruessink & Jeuken, 2002; Davidson-Arnott & van Heyningen, 2003). On the other hand, when there is no direct threat, it may not be efficient to nourish such a temporal erosional zone. Moreover, it is important to know how a nourishment itself influences the dynamics of the shoreline. Grove *et al.* (1987) suggested that apart from diffusing, a beach nourishment could initiate a solitary downdrift migrating shoreline sand wave. This suggestion is supported by the results of section 4.3 and various other studies where the input of a large body of sand to a coastline appears to initiate a shoreline sand wave (Inman, 1987; Thevenot & Kraus, 1995; Ruessink & Jeuken, 2002; Davidson-Arnott & van Heyningen, 2003). In this section we discuss the evolution of a beach nourishment, a shoreface nourishment and a scenario with an offshore dredge pit, under high angle wave conditions. First we will give some background information on the different scenarios.

4.6.1 Shore nourishment

The term shore nourishment is used as a general term for different nourishment schemes like dune reinforcement, beach nourishment and shoreface nourishment. Beach nourishment is the most commonly applied method and involves the placement of large quantities of sand on the subaerial beach, advancing the shoreline seaward (Dean, 2002). The volume of sand involved in beach nourishment is in the range of one to several million cubic meters spread over an alongshore section of several kilometers. The shoreline advances seaward several tens of meters and the initial nourished cross-shore profile is usually steeper than the original beach profile. This often results in an initially rapid diffusion in the cross-shore direction up to the depth of closure, until the equilibrium shape of the profile is restored. The planform diffusion depends on wave conditions and the amplitude and length of the nourishment. Typically the diffusion is slower for a wide nourishment with a small amplitude. The choice of the nourishment sand is also important for the success of a beach nourishment. Ideally, the nourished sand should have a similar or greater grain size than the local sand (Capobianco *et al.*, 2002). Relative coarse sediment allows for a steeper equilibrium profile, which leads to a relatively bigger advancement of the beach. Relative fine sediment adapts to a milder equilibrium slope and the majority of the nourished sand is therefore spread out over the cross-shore profile. Moreover, relative fine sediment leads to an increased alongshore spreading.

A second nourishment approach is shoreface nourishment, in which the sand is placed as a submerged berm (Dean, 2002). The submerged berm is located within the active zone of the cross-shore profile over an alongshore section of several kilometres. This method is gaining popularity as it seems to be effective and is cheaper than beach nourishment. Its effectiveness depends on two mechanisms. The first one is the feeder effect due to onshore transport of sand from the shoreface nourishment to the beach. The second one is the lee effect of the berm, which causes wave shadow and wave focusing, leading to gradients in

alongshore sediment transport. In particular, when a net alongshore transport is present there will be accretion in the lee of the berm due to a decrease in transport capacity. This can however also cause a downdrift zone of erosion due to the subsequent increasing transport capacity (van Duin *et al.*, 2004). The behaviour of shoreface nourishments is usually complex as they interact with bar dynamics (Grunnet & Ruessink, 2004).

Nourishments require a nearby source of good quality sand, which is usually dredged from an offshore location. These borrow pits can affect the shoreline directly by trapping sediment from the nearshore and indirectly through wave transformation and the resulting transport gradients (Dean, 2002). Borrow pits are generally located at depths greater than the depth of closure. Therefore they fill in very slowly and their forcing on the shoreline can persist for decades. Some discussion exists on the capacity of the CERC formula to correctly predict transport gradients due to bathymetric perturbations like borrow pits. On the one hand, Bender & Dean (2004) used an analytical wave transformation and the CERC formula to compute alongshore sediment transport and their predictions showed accretion in the shadow zone of a borrow pit with a downdrift erosional zone, qualitatively in agreement with results of process based models (Benedet & List, 2008; Hartog *et al.*, 2008). These results were only obtained if the additional term, which describes the contribution of alongshore gradients in wave height (Ozasa & Brampton, 1980), was added to the CERC formula. On the other hand, List *et al.* (2006, 2008) suggested that the transport gradients shoreward of a borrow pit computed with the CERC formula are out of phase with those of a process-based model, even when the additional term is added to the CERC formula. Probably, the validity of the CERC formula in the context of bathymetric perturbations depends largely on their length scale. Therefore, care should be taken when the CERC formula is used to predict alongshore transport gradients shoreward of a borrow pit when no observations are available for calibration.

4.6.2 Modelling results

The Gaussian shaped perturbation of the default simulation (see section 4.3) can be seen as a schematized beach nourishment on an open coast and the results are very similar to the results of van den Berg *et al.* (2011*a*). In the latter study the same model and conditions were used but the domain was only 20 km long and the perturbation had a slightly different shape and a steeper cross-shore profile but the volume and alongshore width were similar. The results of both studies suggest that the evolution of a nourishment might be completely different than a prediction by a traditional 1-line shoreline model, specially under dominant high angle waves conditions. Under dominant high angle wave incidence (with wave angles greater than the critical value at the depth of closure) the modelled nourishment grew and migrated downdrift. This might not be a big problem but the simulations also predicted the development of a downdrift erosional zone and on a beach that requires nourishment this might be a serious side effect. Furthermore, the simulations predicted a chain-reaction, leading to the development of a sand wave train, which introduces variability in the downdrift shoreline stretch.

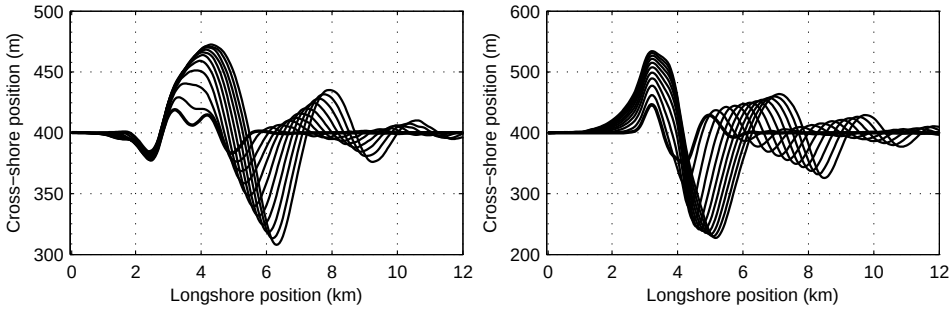

Figure 4.7: Initial development of the shoreline for the shoreface nourishment scenario (left panel) and the borrow pit scenario (right panel) using the default offshore wave conditions. The shoreline is plotted every 3 months and the final line corresponds to the result after 2 years. Notice the difference in the scaling of the cross-shore axis between both panels.

The shoreface nourishment and the borrow pit scenario were explored in van den Berg *et al.* (2011*a*). The shoreface nourishment was located between -6 and -8 m water depth and had a height of 3 m. The water depth above the crest of the shoreface nourishment was 4 m and the volume of the nourishment was similar to the beach nourishment scenario. The borrow pit was 1 km long and 100 m wide. It was located between -9 and -11 m water depth and it had a depth of 4 m. The volume of the borrow pit was smaller than for the other scenarios(0.4 Mm^3). The default high angle wave conditions and parameter setting were used (see table 3.1). Figure 4.7 shows the initial forcing of the shoreline for the shoreface nourishment and borrow pit scenario. The refraction over the shoreface nourishment forced gradients in alongshore transport and this created two erosional zones at the outer sides of its shadow and two accretional zones at the inner sides of its shadow. The accretional zones merged and grew to a single sand wave crest. This initial forcing is qualitatively in accordance with van Duin *et al.* (2004). The downdrift erosional zone grew and triggered the development of a downdrift sand wave train. The refraction over the borrow pit caused a mirrored forcing on the shoreline, with two accretional zones at the outer sides of the shadow and an erosional zone in its shadow. Notice that this pattern does not seem realistic, when compared with most of the studies discussed at the end of section 4.6.1. However, it is similar to what Bender & Dean (2004) found for simulations with the parameter K_2 of the second term of the CERC formula set to 0 (see section 2.2.1). In our simulations, $K_2 = K_1$ but the alongshore gradients in wave height were very small so that the second term of CERC was negligible. Because the borrow pit was located at deep water it was hardly filled in with sediment. Therefore its forcing on the shoreline remained relatively constant during the simulation and the first accretional zone grew in amplitude without migrating downdrift. Downdrift, the feedback mechanism took over and the erosional trough and the second accretional zone did not only grow but also migrated and a downdrift sand wave train was triggered. Notice that this is the only scenario where the second sand wave originated directly from the forcing and this contributed to the relatively fast development of the sand wave train.

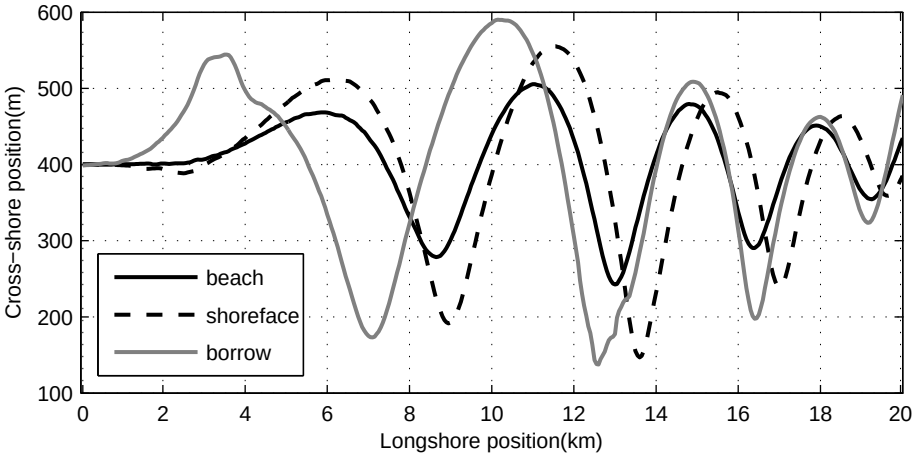

Figure 4.8: Final shoreline after 8 years for the three nourishment scenarios and the default offshore wave conditions. Notice the exaggeration in the cross-shore axis.

The shoreline evolution of the three scenarios used in van den Berg *et al.* (2011*a*) are compared in figure 4.8. In general the beach and shoreface nourishment evolved in a similar way, however the latter resulted into greater amplitudes of the sand waves. The larger amplitude of the first sand wave can be explained by the prolonged forcing on the shoreline by the shoreface nourishment. After 2 years the shoreface nourishment had diffused and from that moment on the shoreline dynamics were only controlled by the feedback between the shoreline changes and the wave field. The borrow pit scenario showed a different behaviour. As explained before, the crest of the first sand wave remained at the same location and only grew in amplitude. The resulting downdrift erosional zone was limited in its downdrift migration by the stationary crest and the wavelength of the first sand wave increased slowly. The combination of the static position of the crest and the deposition on the downdrift slope led to a bumpy shape. The development of the downdrift sand wave train was similar to the other scenarios. The growth rates were similar and the differences in amplitude between the different scenarios were simply the result of the differences in the initial development of the shoreline perturbation.

4.6.3 Discussion

First of all, it is important to emphasize that the model is idealized and that the model has not been calibrated. Therefore, the results only give a qualitative idea of the shoreline evolution for the three scenarios. The relatively simple wave module does not account for diffraction and reflection, which might be important for the correct computation of the wave field in case of the shoreface nourishment and borrow pit scenarios. Furthermore, the parametrized computation of the alongshore sediment transport with the CERC formula might not predict the correct transport gradients in the shadow of a shoreface

nourishment or a borrow pit. The initial shoreline perturbation in these two scenarios might therefore be somewhat different in reality.

The constant high angle wave conditions that were used for these simulations are rare on natural coasts and it has been shown in section 4.4 that the strength of the instability decreases when the wave incidence angle at the depth of closure decreases until the critical angle. It is therefore expected that the effect of shoreline instability on a real coast will be milder. For dominant wave incidence angles close to the critical value it is expected that the shoreline perturbation, caused by a nourishment, will maintain more or less its volume while it migrates downdrift at a rate of the order of 150 m/yr. The development of the spatial-temporal instability will be very weak but the erosion downdrift of the initial perturbation might be substantial, leading to a shoreline retreat in the order of 20 m. This behaviour is more consistent with observations of the dynamics of shoreline sand waves on real coasts. For even lower wave incidence angles the shoreline will be stable. On the majority of the coasts, the wave climate will be variable, incorporating a range of wave heights, periods and incidence angles. The evolution of a nourished coast and the possible negative effects of shoreline instability will depend on the relative contribution of stable and unstable conditions.

In the simulations, the nourishments were added to an otherwise straight coastline. In reality it is more likely that a nourishment is added to an undulating shoreline to mitigate the erosion in the troughs of the undulations. Therefore, it would be interesting to predict the effect of a nourishment on the natural sand wave dynamics. A detailed study of this is out of the scope of this study. We expect that any erosional zone, related to the trough of a shoreline sand wave, would recover and that other sand waves would remain unaffected. It could be fairly easy to use a beach nourishment to fill in a shoreline undulation but it would be far more difficult to also fill in the related undulation in the bathymetry, which could extend up to the depth of closure. If only a slight signal remains in the bathymetry, HAWI would cause the erosional zone to develop again. A model that correctly predicts the dynamics of the shoreline undulations would be useful in order to predict for different nourishment strategies, how fast the erosional zone would reform and if the nourishment strategy is cost effective. Wijnberg *et al.* (2006) studied the evolution of a relative short scale sand wave on the Dutch coast at Egmond after the trough was filled in with a beach nourishment. They found that the trough recovered in about half a year but they did not find a correlation between the recovery of the through and high angle wave conditions and it remained unclear what mechanism resulted into the recovery of the through.

4.7 Conclusions

A quasi 2D morphodynamic model for large scale shoreline dynamics was used to study the evolution of a coast with a localized large scale perturbation under constant high angle wave incidence conditions. Simulations showed that, if the wave incidence angle at the depth of closure was bigger than the critical value, the perturbation developed into a downdrift migrating shoreline sand wave and it triggered the growth of a downdrift

sand wave train through a chain-reaction in the alongshore sediment gradients. The formation of the sand wave train is a self-organized response of the morphodynamic system and can be seen as a spatial-temporal instability. While new sand waves were formed downdrift with initial wavelengths of about 2 km, the amplitude and wavelength of the older sand waves continued to increased and they migrated downdrift at relatively low rates. The first sand waves of the train therefore had bigger amplitudes and wavelengths.

The initial development of a sand wave field from a large scale perturbation was relatively fast compared to the formation in unison from small scale random perturbations in chapter 3 (in the order of $1-3$ years compared to $5-10$ years). The minimal wavelength of about 2 km, at which the spatial-temporal instability developed, is consistent with the minimal wavelength for sand wave formation found in chapter 3 and by Falqués & Calvete (2005).

The default experiment showed the development of 6 sand waves within the domain during 9 simulation years. Their mean amplitude ranged between $60 - 220$ m, their wavelength between $2.3 - 7.5$ km and they migrated at $334 - 1080$ m/yr.

The strength of the shoreline instability decreased with decreasing wave incidence angle. For wave incidence angles close to the critical angle, the initial perturbation maintained more or less its volume while it migrated downdrift and the downdrift sand wave train developed very slowly. For even lower wave angles the shoreline was stable and the perturbation diffused.

The dimensions of the shoreline perturbation affected the time scaling of the development of the spatial-temporal instability. Perturbations with a relatively big amplitude resulted into high growth rates. The alongshore length scale of the perturbation had less effect on the growth rates. Perturbations at a very short length scale (0.5 km) diffused even under unstable conditions but they did trigger the development of a downdrift sand wave train.

The results of this chapter show that shoreline instability could have important implications for shore nourishment. Under dominant high angle wave conditions, a beach nourishment could develop into a migrating sand wave including a downdrift erosional zone and it might trigger the growth of a sand wave train. A shoreface nourishment and an offshore borrow pit cause an indirect shoreline perturbation in their shadow, which could also lead to the development of shoreline sand waves. In general, it is important for nourishment planning to understand the variability of the coastline induced by shoreline sand waves and to predict the possible effect of a nourishment on the dynamics of sand waves.

Chapter 5

Formation of sand waves: the effect of variable wave incidence angles*

5.1 Introduction

In the previous chapters we assumed that long term coastal evolution was driven by the mean annual wave climate, represented by one typical value for wave incidence angle, height and period. The constant high angle wave conditions, which were used for the default simulations, are not very common on natural coasts and the simulations showed that the development of shoreline sand waves was very sensitive to the wave incidence angle. In a more realistic situation, high angle wave incidence alternates with low angle wave incidence, favoring coastline instability and stability respectively. Furthermore waves can come from opposite directions and wave height and period change. In this more realistic situation, the morphological changes are the result of the net effect of the varying wave conditions and these changes might differ from the morphological changes that are predicted with a mean annual wave climate. It is therefore essential to look at the sensitivity of the results to more realistic wave conditions.

Ashton & Murray (2006*a*) studied the effect of different wave probability distribution functions (only varying wave incidence angle) on HAWI and found that, if high incidence angles occurred for more than 50% of the time, undulations arose from an initially straight coastline. Different fractions of high and low angle waves and opposing wave directions led to a different shoreline response with features varying from shoreline sand waves

*Sections 5.2.1, 5.2.3 and 5.3.1 are largely based on van den Berg *et al.* (2011*b*): van den Berg, N., Falqués, A. & Ribas, F. 2011b. Modelling large scale shoreline sand waves under oblique wave incidence. J. Geophys. Res. Under review.

to cuspate bumps, flying spits and reconnecting spits. Falqués (2006) applied a linear model to the Dutch coast using the actual wave climate for a probability distribution function (varying wave angle, height and period). He found that, depending on the cross-shore profile of the sand waves, the fraction of high angle waves was barely sufficient to produce positive growth rates. Various studies suggest that even when high angle waves are not dominant, HAWI might play a role in the downdrift migration and the relatively low diffusion rates of already present large scale shoreline perturbations (Falqués, 2006; Ruessink & Jeuken, 2002; Davidson-Arnott & van Heyningen, 2003).

In the present study we use a simple version of the approach of Ashton & Murray (2006*a*) and choose a representative wave incidence angle for high and low angle conditions ($\theta_0 = 60°$ and $\theta_0 = 30°$ respectively). The fraction of high versus low incidence angle is expressed by the variable U, where $U = 1$ ($U = 0$) means 100% high angle waves (low angle waves) and $U = 0.5$ indicates a symmetrical distribution. A second variable, A, describes the fraction of waves approaching from the left relative to mean shoreline trend versus waves approaching from the right (asymmetry), where $A = 1$ ($A = 0$) means that all waves come from the left (right). The different incidence angles that are used for a specific simulation, occur all within one simulated day. This relatively short duration is chosen to minimize chronology effects, i.e. the order of the different wave conditions has a minimum effect on the shoreline evolution. As a first step, we only vary the wave angle and use the default and constant values for H_s and T_p. Varying the wave height and period would however also affect the evolution of the shoreline because for some combinations of wave angle, height and period, instability does not occur (see section 3.6). In order to study the effect of variable wave incidence angle on the formation of sand waves from random initial perturbations, we use the default experiment of chapter 3. The default experiment of chapter 4 is used to study the effect on a localized large scale perturbation.

5.2 Alternating high and low wave incidence angles

5.2.1 Random initial perturbations

Simulations with small scale random perturbations showed that a slight reduction of the fraction of high angle waves ($U = 0.9$) strongly reduced the spontaneous development of shoreline sand waves (using $A = 1$). After 20 simulated years, 4 sand waves with a wavelength of about 5 km and a mean amplitude of only 20 m developed (figure 5.1). This is in contrast to the default simulation ($U = 1$) where 6 sand waves with $\lambda = 4$ km and a mean amplitude up to 121 m developed within 13 years (see section 3.3). Reducing U to 0.8 almost inhibited the development of the sand waves and, besides some shoreline irregularities with an amplitude of 1 m, merely one sand wave developed with a wavelength of 7 km and an amplitude of 5 m after 20 simulated years (figure 5.1). For even lower values of U the growth rate of this single sand wave decreased further and for $U = 0.5$ it merely developed until an amplitude of about 1 m after 20 years (not shown).

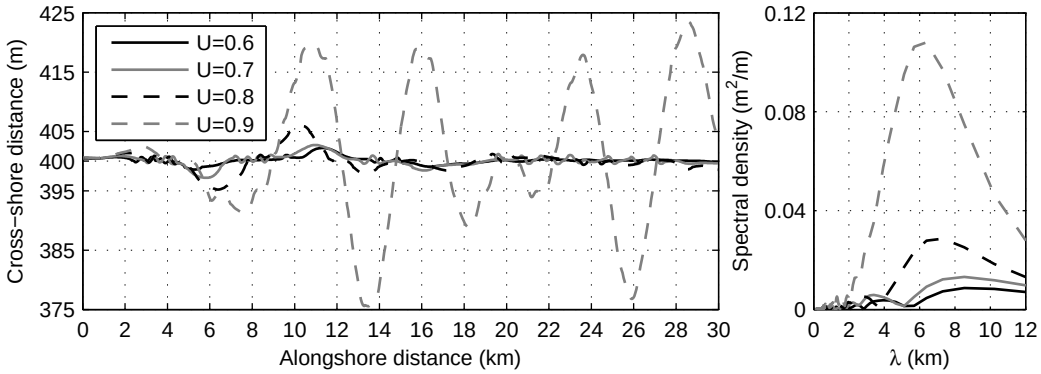

Figure 5.1: The shoreline after 20 simulation years for different fractions of high angle wave incidence, indicated by the variable U (left panel). The corresponding Fourier analysis of the shorelines (right panel).

The present results suggest that the spontaneous formation of sand waves due to HAWI requires a wave climate with a minimum contribution of high incidence angles of about 80% and that the wavelength increases for lower fractions of high angle waves. Apparently the contribution of the diffusive effect of the low angle waves ($\theta_0 = 30°$) to the shoreline dynamics was relatively stronger than the anti-diffusive effect (growth) of the high angle waves ($\theta_0 = 60°$). This can be explained as follows. The wave angles were chosen at an equal distance from the critical incidence angle of 45°. These are however the wave angles at the offshore boundary of the model and it is the wave angle at the depth of closure that is relevant for HAWI. The corresponding wave incidence angles at the depth of closure were $\theta_{Dc} = 27°$ and $\theta_{Dc} = 52°$ respectively. The latter value is only just above the critical angle and the negative diffusivity was therefore weak in comparison to the diffusivity of the low angle waves. However, the present results might be representative for a real coast, where the range of low angle waves is in general greater than the range of high angle waves (for the present study $\theta_0 \approx 0 - 50°$ and $\theta_0 \approx 50 - 60°$ respectively). This means that the net effect of the low angle waves will always tend to be stronger than the net effect of high angle waves in case of $U = 0.5$ and that instability only occurs for higher values of U. Non-linear effects could also add to the relative slow or negligible development of shoreline sand waves due to a fraction of low angle waves. For $U = 0.8$, one undulation developed with a relative long wavelength and, as will be discussed in section 6.3, the growth rate of this length scale is relatively low.

5.2.2 Localized initial perturbation

The growth/diffusion rate of the initial perturbation is plotted in figure 5.2a for the different values of U. During all simulations there was an initial fast retreat of the shoreline due to the adaption to the cross-shore equilibrium slope. For $U = 0.9$ the initial diffusion changed into growth at a rate of 0.03 yr^{-1}, which is a factor 5 smaller than for

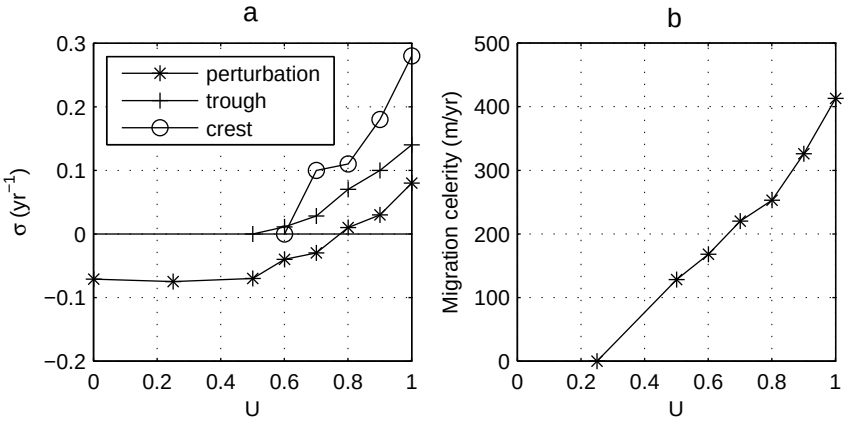

Figure 5.2: (a) The growth rate (σ) of a Gaussian shaped shoreline perturbation, its downdrift erosional zone (trough) and the first crest of the downdrift sand wave train for different values of U, computed over a period of 9 years. A negative growth rate of the shoreline perturbation indicates diffusion. (b) The average downdrift migration celerity of the initial shoreline perturbation for different values of U, computed over a period of 9 years.

the default simulation in chapter 4. After 9 simulation years $\bar{A}$ was 63 m. for $U = 0.8$ the growth rate was almost zero, which means that the amplitude of the perturbation remained more or less stable at 26 m after the initial shoreline retreat. For lower values of U the perturbation simply continued to diffuse at increasing rates. The growth rate of the downdrift erosional zone was smaller for a decreasing U but it still developed for values at which the initial perturbation only diffused (figure 5.2a). For $U = 0.6$ the amplitude of the erosional zone was only 5 m and together with the diffusing perturbation it formed a sand wave with a wavelength of about 10 km. The development of the first new downdrift crest is used as an indication of the development of the spatial-temporal instability. The growth rate of this crest decreased with a decreasing U and for $U < 0.7$ no downdrift sand wave developed (figure 5.2a). The spatial-temporal instability seems to be dampened less by the low angle waves than the spontaneous sand wave formation in the previous section. Figure 5.2b shows how the downdrift migration celerity of the initial perturbation decreased with a decreasing U. For $U = 0.25$ no downdrift migration could be observed and the perturbation only became asymmetrical.

5.2.3 Discussion on shoreline diffusivity

The previous two sections showed that shoreline instability requires a relatively big fraction of high angle wave incidence and that this can be explained by the, in general, stronger positive diffusion of the low angle waves compared to the negative diffusion of the high angle waves. This is in contradiction with the results of Ashton & Murray

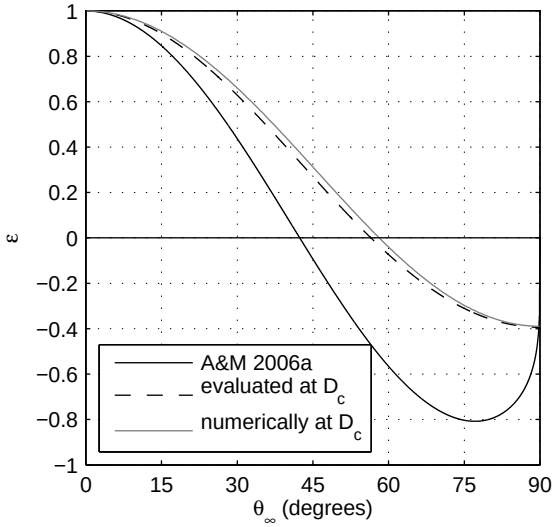

Figure 5.3: The shoreline diffusivity, ϵ, as a function of the deep water wave angle after Ashton & Murray (2006a) (solid line). The deep water angle dependance evaluated at D_c, refracted back to deep water quantities (dashed line). The angle dependance computed numerically at D_c, refracted back to deep water quantities (gray line).

(2006a) who found that instability occurred for $U > 0.5$. In order to understand this discrepancy we briefly discuss the approach presented in that paper and compare this with the approach used in this thesis.

Ashton & Murray (2006a) distributed the fraction of high and low wave incidence angles with a probability function over the wave angle bins, $\theta_\infty = 45°$ - $90°$ and $\theta_\infty = 0°$ - $45°$ respectively. Ashton & Murray (2006b) state that, for a symmetrical distribution ($U = 0.5$), the magnitude of the net negative diffusivity (high angle bin) is comparable to the magnitude of the net positive diffusivity (low angle bin). This can be demonstrated as follows. Inserting the deep water version of the CERC formula (equation 1.7) into the equation for the shoreline diffusivity coefficient (equation 1.4) results into

$$\epsilon = \frac{K_2}{D} H_\infty^{\frac{12}{5}} T_p^{\frac{1}{5}} \cos^{\frac{1}{5}}(\theta_\infty - \phi) \left(\cos^2(\theta_\infty - \phi) - \left(\frac{6}{5}\right) \sin^2(\theta_\infty - \phi) \right). \qquad (5.1)$$

Because θ_∞ is the wave angle at the base of the shoreface (D_∞), before the waves experience nearshore shoaling and refraction (i.e. the wave base), any angle between $0°$ and $90°$ is theoretically possible. Figure 5.3 shows ϵ as a function of θ_∞ (solid line). Based on this dependance we can now estimate the net effect of a symmetrical wave distribution over the high and low angle wave bins. The integral of the dependence of ϵ on θ_∞ is the same for both wave bins. Thus, the positive diffusion produced by the low angle waves equals in magnitude the negative diffusivity produced by the high angle waves, i.e. for this approach instability indeed occurs for $U > 0.5$.

The essential difference between the approach of the present thesis and that of Ashton & Murray (2006*a*) lies in the fact that the later assumes that the depth of closure, D_c, in equation (1.1) is equivalent to D_∞, i.e. that the shoreline perturbations extend into the bathymetry up to D_∞ (see section 1.3.2). In the Q2D-morfo model the perturbations extend up to D_c and in general $D_\infty > D_c$. For example, in our computations with $T = 6$ s, $D_c \simeq 8$ m whereas $D_\infty \simeq 30$ m. The approach of the present thesis seems more realistic in the context of sand wave formation and the critical wave angle should therefore be evaluated at D_c, which means that the corresponding wave angle at deep water has to be even bigger (see section 3.5). For example, using $T_p = 6$ s and $D_c = 8$ m, $\theta_\infty \approx 61°$ in order to have $\theta_{Dc} \approx 45°$. This means that the separation of the low and high angle wave bin at 45° is not correct and the solid line in figure 5.3 is no longer valid. The crossing with the y-axis would shift to higher wave angles and the high angle wave bin would become smaller.

In order to compare qualitatively the approach of the present study with the approach of Ashton & Murray (2006*a*), we can try to find the dependance of the shoreline diffusivity on θ_{Dc}. One option is to assume that that equation (1.7) is valid at intermediate water depth (D_c) and ϵ can than be computed with equation (5.1), using H_{Dc} and θ_{Dc}. In order to plot the dependance of ϵ on θ_{Dc} against the corresponding deep water wave angle, the waves are refracted from D_c back to deep water over a rectilinear bathymetry (from D_c up to D_∞ the bathymetry is unperturbed). The resulting dependance is plotted in figure 5.3 with a dashed line. In this more realistic situation, the high angle wave bin is clearly smaller than the low angle bin and the magnitude of the negative diffusion is smaller. For a symmetrical distribution ($U = 0.5$), the net negative diffusion is a factor 4 smaller than the net positive diffusion. This suggests that a value of $U > 0.8$ is required for shoreline instability and the spontaneous formation of shoreline sand waves.

A second, and more accurate method would be to express Q directly as a function of H_{Dc} and θ_{Dc}. This can not be done analytically and this has therefore been done numerically, solving the dispersion relation, Snell law and energy conservation (see Falqués, 2003). The obtained dependance of ϵ on θ_{Dc} can again be plotted against the corresponding deep water angle. The resulting curve (gray line) is very similar to the curve obtained with the first method and this demonstrates that equation (1.7) can indeed be applied at intermediate water depths. It can be concluded that, if in the approach of Ashton & Murray (2006*a*) it is assumed that the cross-shore extent of the shoreline perturbations is up to depth of closure instead of the wave base, U needs to be approximately bigger than 0.8 for shoreline instability, This is consistent with the results of the Q2D-Morfo model in the previous two sections.

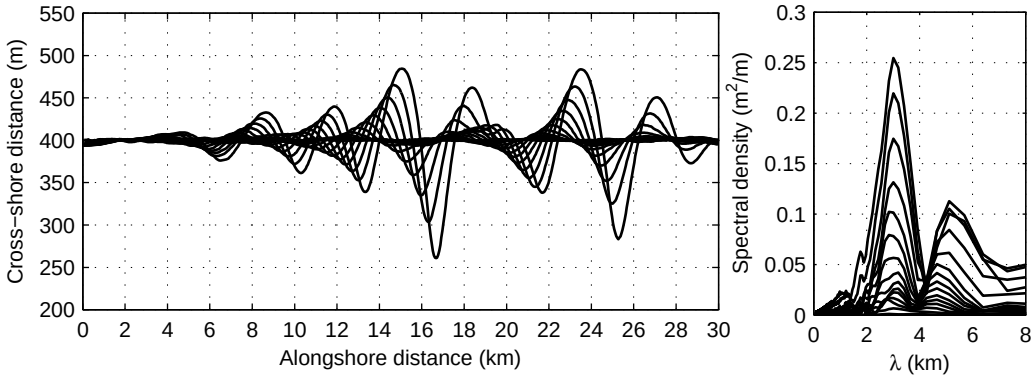

Figure 5.4: The evolution of the shoreline over 13 simulation years for bimodal high angle wave incidence ($U = 1$, $A = 0.75$), starting from random perturbations (left panel). The shorelines are plotted each year. The corresponding Fourier analysis of the shorelines (right panel).

5.3 Bimodal high angle wave incidence

5.3.1 Random initial perturbations

Here we explore the effect of bimodal high angle wave incidence on the spontaneous formation of sand waves ($U = 1$, $A =$variable). When a fraction of the waves came from the opposite direction ($A = 0.75$) the growth and migration rate ($\sigma = 0.26$ yr^{-1} and $v = 350$ m/yr) were lower than for the default simulation (see section 3.3) and the wavelength of the sand waves increased gradually during the 13 simulation years from the initial 2 km until only 3 km (figure 5.4).

For $A = 0.5$, a regular sand wave field developed and the sand waves did not migrate (figure 5.5). The sand waves developed initially with $\lambda \approx 2$ km but after about two years the dominant wavelength started to shift to 4 km. This shift took place while the amplitudes were still small (between 1 and 4 m) and it was not the result of a gradual stretching of the individual sand waves nor the result of merging because both would require migration. Instead, non-linear dynamics led to the reorganization of the sand wave field and a subharmonic of the initial unstable undulation became dominant. The secondary peak in the energy density spectrum of figure 5.5 (right panel, black line) shows the subharmonic at 4 km. This 4 km undulation was formed by crests with a slightly larger amplitude. These relatively large crests grew faster in amplitude and became more symmetrical. Each adjacent relatively small crest diffused and disappeared due to the formation of wider troughs between the bigger crests. In general every second crest disappeared and the initial spacing of about 2 km shifted to the more optimal spacing of about 4 km. The amplitude of the resulting regular and symmetrical sand waves grew during the rest of the simulation at a rate $\sigma = 0.26$ yr^{-1} and their wavelength and

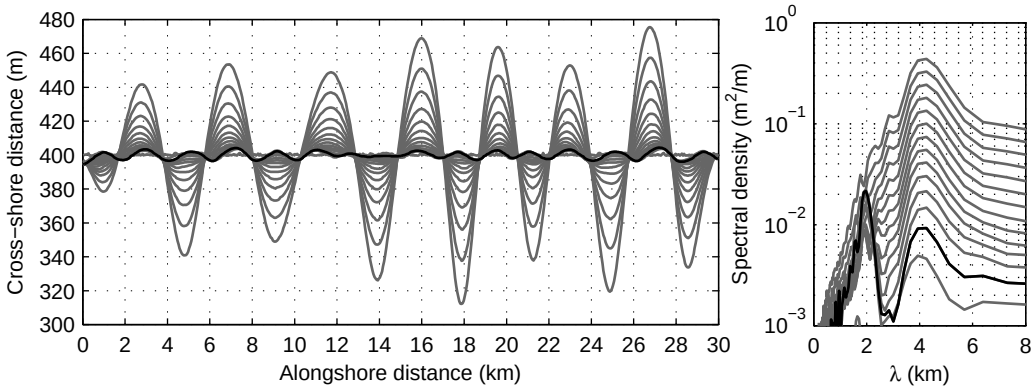

Figure 5.5: The evolution of the shoreline over 13 simulation years for bimodal high angle wave incidence ($U = 1$, $A = 0.5$), starting from random perturbations (left panel). The shorelines are plotted each year and the black line indicates the shoreline after 2 years. The corresponding Fourier analysis of the shorelines (right panel).

position remained constant. The growth of stationary and symmetrical sand waves is very similar to the formation of the so-called 'cuspate bumps', described by Ashton & Murray (2006*b*). Due to the symmetrical wave climate, net accretion only took place at the crest and net erosion only at the trough. The erosion at the updrift flank and deposition at the downdrift flank was canceled out when the waves came from the opposite direction and the net change at the flanks was therefore minimal. At the crest and the trough there was a zone with accretion and erosion respectively during both conditions, which did lead to a net change.

5.3.2 Localized initial perturbation

When a fraction of the high angle waves came from the opposite direction ($A = 0.75$) the initial shoreline perturbation diffused less during the first year and grew faster in the following years at a growth rate of 0.17 yr^{-1}, compared to 0.08 yr^{-1} for $A = 1$. This is an interesting result because the simulations with random initial perturbations showed a decrease of the growth rate for bimodal waves (see section 5.3.1). An explanation for this can probably be found in the fact that the bathymetry updrift of the initial perturbation was rectilinear for the simulations with $A = 1$ and the sand wave train only developed on the downdrift side (see section 4.3.1). The wave field and transport gradients at the initial perturbation were different than at a crest in the middle of the sand wave train and the initial perturbation always grew at a relatively low rate. In the present simulation a sand wave train still developed on the right side of the perturbation because the majority of the waves arrived from the left. However, when the smaller fraction of waves arrived from the right, the waves approached the perturbation over an undulating bathymetry and the resulting transport gradients favored the growth of

the initial perturbation. Furthermore, an erosional trough slowly developed at the left side of the perturbation, which also favored the growth when the waves arrive from the left. The growth of the spatial instability itself was dampened due to the bimodal waves because the formation and growth of the new sand waves, due to the chain reaction in alongshore transport, was slower.

For $A = 0.5$, the spatial-temporal instability developed symmetrically on both sides of the initial perturbation and the perturbation itself was stationary with again a slightly higher growth rate of 0.22 yr^{-1} (figure 5.6). The development of the spatial instability was dampened further and on each side only 2 relatively small sand waves developed after 9 simulation years.

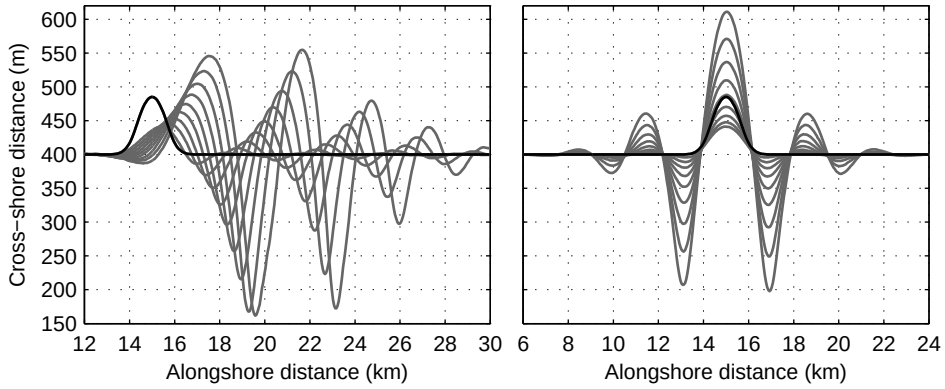

Figure 5.6: The evolution of the shoreline over 9 simulation years for bimodal high angle wave incidence, starting from a localized perturbation; left panel $U = 1$, $A = 0.75$ and right panel $U = 1$, $A = 0.5$. The shorelines are plotted each year and the black line indicates the initial shoreline.

5.4 Conclusions

A more realistic wave climate, with alternating high and low angle wave incidence (represented by 60° and 30°, respectively), reduced the potential for spontaneous sand wave formation from small scale perturbations. Even a very small fraction of low angle waves, strongly reduced the growth rate of the sand waves and for a fraction of high angle waves lower than 80%, no regular sand wave field developed. It is demonstrated that the range of wave angles that lead to stability is larger than the range of wave angles that lead to instability and that the average magnitude of the positive diffusion produced by the stable wave angles is bigger than the average magnitude of the negative diffusion, produced by the unstable wave angles.

Small fractions of low angle waves also reduced the growth rate of a localized large

scale perturbation. For a fraction of high angle waves around 80%, the perturbation more or less maintained its volume while it migrated downdrift. This result compliments previous studies which suggest that, even if high angle waves are not dominant, HAWI might play a role in the persistence and downdrift migration of large scale shoreline perturbations. For an increasing fraction of low angle waves the perturbation diffused at an increasing rate and the migration rate decreased. The spatial-temporal instability developed slower due to small fractions of low angle waves. When the fraction of high angle waves decreased to 60% merely a mild downdrift erosional zone developed and for even lower fractions there was no effect on the coast adjacent to the initial perturbation.

A bimodal wave climate, with fractions of high angle waves coming from opposite directions, reduced the growth and migration rate of the shoreline sand waves that formed from small scale perturbations. When the wave climate was symmetrical, the small scale perturbations developed into a very regular sand wave field and the sand waves did not migrate. The sand waves initially developed with $\lambda = 2$ km but non-linear dynamics led to the reorganization of the sand waves and a subharmonic of $\lambda = 4$ km became the dominant wavelength.

The growth rate of a localized large scale perturbation was enhanced by a bimodal wave climate but the development of the spatial-temporal instability was dampened. When the wave climate was symmetrical, the localized perturbation did not migrate and grew at a relatively high rate. The sand wave train developed very slowly on both sides of the localized perturbation.

Chapter 6

Physical mechanisms*

6.1 Introduction

In the context of one-line shoreline modelling, Ashton *et al.* (2001) showed that the existence of a maximum of the alongshore transport rate curve, $Q(\theta_\infty - \phi)$, could lead to shoreline instability and the growth of shoreline perturbations (see figure 1.3). In a 2DH context, high angle wave instability develops due to specific gradients in alongshore transport along a perturbed shoreline. The physical mechanism behind shoreline instability is the feedback between the shoreline changes and the wave field through wave refraction and shoaling over the associated bathymetry. This leads to alongshore gradients in wave angle and height at breaking, which drive the alongshore sediment transport. For deep water waves higher than 42°, the gradients in wave height at breaking become dominant and lead to a transport pattern that results into growth and migration of shoreline perturbations (Ashton *et al.*, 2001; Falqués, 2003; Falqués & Calvete, 2005; Ashton & Murray, 2006*a*; Falqués *et al.*, 2011). In the present study this was refined by showing that HAWI only develops when the wave angle at the depth of closure is bigger than the critical angle of about 42° (see also Uguccioni *et al.*, 2006).

The actual development of HAWI thus depends on the adequate transport gradients along a perturbed coastline. The Q2D-morfo model can provide further insight into the physical mechanism behind shoreline instability and the formation of shoreline sand waves, by directly looking at the 2D picture and the causes for the alongshore gradients in Q, in line with the study of List & Ashton (2007). In section 6.2 the gradients of Q, the wave angle and height along a undulating coastline are studied. Stable and unstable wave conditions are compared and the results of the Q2D-morfo model are compared with the traditional one-line modelling approach and the approach of Ashton *et al.* (2001);

*Sections 6.2, 6.3.1 and 6.3 are largely based on van den Berg *et al.* (2011*b*): van den Berg, N., Falqués, A. & Ribas, F. 2011b. Modelling large scale shoreline sand waves under oblique wave incidence. J. Geophys. Res. Under review.

Ashton & Murray (2006*a*) (referred to as Ashton&Murray approach).

An important assumption of the Ashton&Murray approach is that their model is only valid for shoreline evolution on a large temporal and spatial scale. However, their model does not predict a minimum or optimal length scale for HAWI. The studies of Falqués & Calvete (2005); Uguccioni *et al.* (2006) did demonstrate the existence of a minimum and optimal length scale for HAWI. The length scale was suggested to depend on the cross-shore profile slope and to scale with the surf zone width but the physical mechanism behind the wavelength selection remained unclear. Section 6.3 explores the physical mechanism behind wavelength selection by looking at shoreline undulations with various wavelengths.

In section 6.4 the spatial-temporal instability is explained by looking at the alongshore gradients of Q and in section 6.5 we discuss the model limitations, finite amplitude behaviour and the bathymetry associated with shoreline sand waves.

6.2 High angle wave instability

6.2.1 Transport gradients along an undulating shoreline

In order to gain more insight into the physical mechanism behind shoreline instability we look at the transport gradients along a uniformly undulating shoreline. Here we do not study the evolution of this undulation but we only compute the wave field and resulting alongshore transport and analyse them for unstable ($\theta_0 = 60°$) and stable ($\theta_0 = 30°$) conditions. Three different approaches are compared: i) Q2D-morfo, ii) traditional one-line model and iii) Ashton&Murray. In approach (ii), the feedback of the morphology into the wave field is disregarded. The wave height and angle at breaking are computed by wave transformation over a rectilinear bathymetry and they are therefore constant in the alongshore direction. Q varies alongshore as a function of the relative wave angle at breaking, which depends only on the orientation of the shoreline (see section 1.2). In approach (iii), the alongshore transport is computed as a function of deep water waves and the shoreline orientation, according to the method of Ashton *et al.* (2001) (see equation 1.7). This is similar to the 'CERC-recast' in List & Ashton (2007) and to obtain the wave height and angle at deep water, the waves at the offshore boundary (10.9 m depth) are transformed to deep water waves (50 m depth) by using linear wave theory and assuming a rectilinear bathymetry. The wave height and angle at deep water for unstable and stable conditions were $H_\infty = 1.73$ m, $\theta_\infty = 78.5°$ and $H_\infty = 1.12$ m, $\theta_\infty = 34.5°$ respectively.

The bathymetry with an uniformly undulating shoreline was constructed with the default cross-shore equilibrium profile and a sinusoidal shoreline perturbation was added. A wavelength of 3 km was chosen for the undulation because the simulations in the previous chapter showed that the range of $2-4$ km was most common for the development of sand waves. A domain size of 30 km and the default parameter setting were used (see

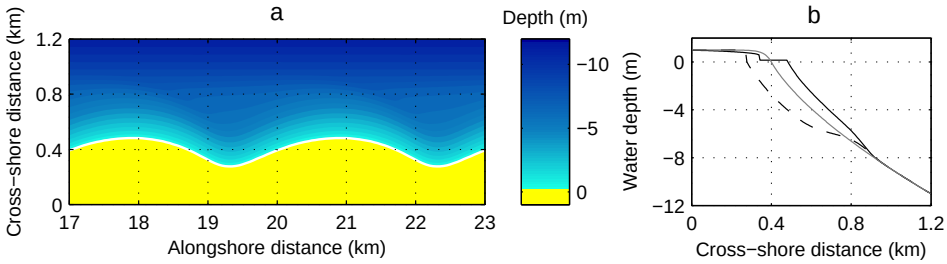

Figure 6.1: (a) The undulating bathymetry with $\lambda = 3$ km, which is used to study the alongshore gradients of the transport. Notice that the cross-shore distance is exaggerated by a factor 2. (b) The cross-shore profile at the crest (solid line), at the through (dashed line) and the equilibrium profile (gray line).

table 3.1). Subsequently, this bathymtery was forced during 2 years with high angle wave conditions. During these years the perturbed bathymetry adapted to the equilibrium profile and the undulation reorganized until an optimal configuration was reached and shoreline instability led to the growth of the undulation. The undulation was still uniform with a wavelength of 3 km and an amplitude of 82 m. Figure 6.1 shows a 6 km section of this bathymetry and the cross-shore profile at the crest and the trough.

Figures 6.2b and f show the alongshore distribution of Q of the Q2D-morfo model for the unstable and stable wave conditions (solid black line). The wave angle at D_c was $\theta_{Dc} = 52°$ and $\theta_{Dc} = 27°$, respectively and the associated wave height $H_{Dc} = 0.89$ m and $H_{Dc} = 0.98$ m. According to the one-line sediment conservation equation (1.1), a negative transport gradient ($\partial Q/\partial y > 0$) means divergence of the sediment flux (shoreline erosion) and a positive transport gradient ($\partial Q/\partial y < 0$) means convergence of the sediment flux (shoreline accretion). It can be seen that in case $\theta_0 = 60°$ the maximum of the alongshore transport, Q_{max}, is located slightly updrift of the crest, causing accretion at the crest and at the downdrift slope of the sand wave. This leads to growth and downdrift migration of the sand wave. In contrast, for $\theta_0 = 30°$ there is erosion at the crest and accretion at the bay, leading to diffusion of the sand wave along with a slight downdrift translation.

Figures 6.2b and f also show Q for the traditional one-line approach (dashed lines). It is interesting to see that in case $\theta_0 = 30°$ the pattern of Q is qualitatively the same for both the traditional one-line and the Q2D-morfo approach, except for a slight lag for Q2D-morfo, that is responsible for the migration. The gradients of Q are milder for Q2D-morfo, implying a smaller diffusivity than predicted by the traditional approach (Ashton & Murray, 2006*a*; Falqués, 2003; Falqués & Calvete, 2005). In contrast, for $\theta_0 = 60°$, the alongshore distributions of Q for the traditional one-line approach and for Q2D-morfo are very different. The position of Q_{max} did not change for the one-line approach and the shoreline remained stable. For the Q2D-morfo the pattern of Q changed, leading to instability.

The solid gray lines in figure 6.3 indicate the alongshore gradients in Q, obtained

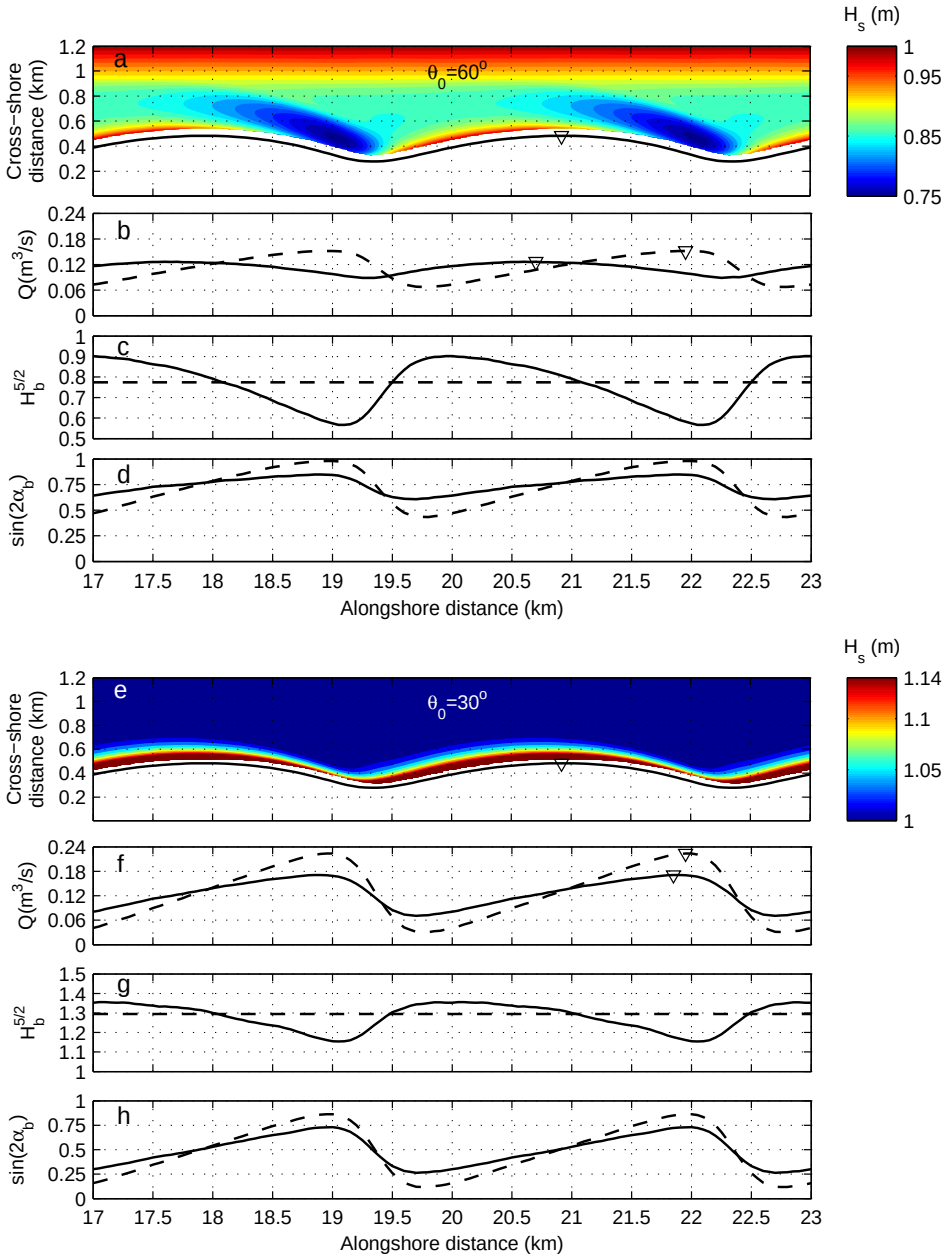

Figure 6.2: Contour plots of the wave height up to breaking for an undulating coastline with $\lambda = 3$ km, (a) $\theta_0 = 60°$ and (e) $\theta_0 = 30°$. The shoreline is indicated by the black line and the waves come from the left. In the panels below: (b and f) alongshore distribution of the sediment transport rate, (c and g) $H_b^{5/2}$ and (d and h) $\sin(2\alpha_b)$. The solid lines represent the results of Q2D-morfo and the dashed lines correspond to the traditional one-line approach. The symbol ∇ indicates the maxima of the shoreline position and Q.

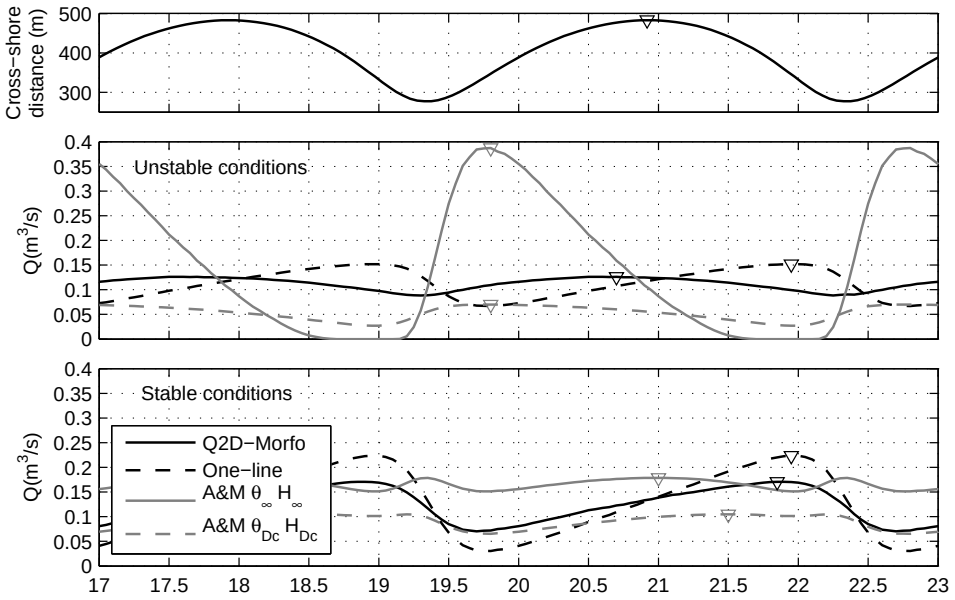

Figure 6.3: The shoreline position of an undulating coast with $\lambda = 3$ km (top panel). The alongshore distribution of the sediment transport rate Q for the Q2D-Morfo approach, the traditional one-line approach, the Ashton&Murray approach using the wave angle and hight at deep water and the Ashton&Murray approach using the wave angle and height at the depth of closure. The middle panel and the lower panel represent unstable ($\theta_0 = 60°$) and stable ($\theta_0 = 30°$) conditions respectively. The symbol ∇ indicates the maxima of the shoreline position and Q.

with the approach of Ashton&Murray (using the wave angle and height at deep water). For the unstable conditions (middle panel), Q_{max} was a factor 3 bigger than for Q2D-morfo and it was located further updrift of the crest. This favors growth over migration and since the gradients were bigger, the growth rate was higher. The magnitude of Q becomes zero at the downdrift slope because here the relative wave angle becomes bigger than 90° (see figure 1.3). This zone, where the transport is zero, can be seen as a wave shadow zone (Ashton & Murray, 2006*a*). In this shadow zone no change takes place and this would lead to the growth of a spit-like shape as described by Ashton & Murray (2006*a*). However, the simulations with Q2D-morfo show that for these relative smooth undulations with a finite cross-shore extent, a zone with zero transport is not realistic. The refraction around the crest of the undulation merely leads to a zone with relatively low wave energy (see figure 6.1a). The development of a spit-like shape from shoreline undulations only seems realistic when the undulations have a relative big amplitude or when they are very asymmetrical with a steep downdrift slope. The present version of the Q2D-morfo model is however not capable of reproducing these shoreline shapes. For stable conditions, the Ashton&Murray approach predicts relatively low transport gradients and Q_{max} is located just downdrift of the crest (figure 6.3, lower panel). The position of Q_{max} favors downdrift migration over diffusion. In addition, the low transport

gradients would also contribute to a relatively low diffusion rate. The position of Q_{max} is the result of the fact that the relative wave angle at the downdrift slope becomes bigger than 42° which leads to a decreasing Q and consequently a local minimum (where the other approaches predict a maximum). This local minimum leads to some form of instability at the downdrift slope.

The comparison with the Ashton&Murray approach shows that using the wave input at the base of the shoreface (wave base) and assume that the shoreline undulations extend up to this depth, strongly overpredicts high angle wave instability and leads to unrealistic behavior at the downdrift slope of shoreline undulations for unstable as well as stable conditions. This is consistent with the exploration in section 5.2.3. The assumption that shoreline undulations extend up to the base of the shoreface only makes sense for very large coastal features such as large spits and capes. In the context of the spontaneous development of shoreline sand waves from small scale perturbations and in the context of the dynamics of shoreline undulations of several kilometers on timescales of years to decades, it is more reasonable to choose the depth of closure as the position to evaluate the critical angle for instability. At this depth the waves begin to shoal and refract over depth contours that follow the curvature of the shoreline. It has been demonstrated in section 3.5 that instability indeed develops for angles at the depth of closure greater than about 42°.

It was demonstrated in section 5.2.3 that the deep water expression for Q of Ashton&Murray can also be applied at intermediate water depth. Therefore, the approach of Ashton&Murray can be applied by using the wave height and angle at the actual depth of closure. Figure 6.3 shows the resulting alongshore transport pattern (dashed gray lines). For unstable conditions, the gradients are now in the same range as the Q2D-morfo approach. However, the position Q_{max} did not change and it was still located further updrift and this leads to a shorter erosional and wider accretional zone and favors growth over migration. This can possibly be explained by the fact that the Ashton&Murray approach does not take into account the effect of wave convergence at the crest (wave focusing). This effect would shift Q_{max} closer to the crest. For stable conditions, the gradients of Q are smaller than for the Q2D-morfo approach. In general, the pattern also leads to erosion of the crest and deposition in the through. The lines coincide at the minimum but deviate at the downdrift flank of the crest. Q_{max} is located slightly further updrift than for the Q2D-morfo approach and this would lead to more migration. These tests suggest that the model of Ashton&Murray can lead to more realistic predictions if an instantaneous shift of the active profile (from the shoreline up to depth of closure) is assumed, instead of assuming an instantaneous shift of the whole shoreface. By assuming that the rest of the shoreface remains rectilinear, the wave height and angle at the depth of closure can be computed by transforming waves from deep water over rectilinear depth contours. The depth of closure could be estimated from observations of an actual bathymetry or from the wave climate using for example the expression of Hallermeier (1978) and it will tend to increase for increasing time scales (Hinton & Nicholls, 1998).

6.2.2 Competition between relative wave angle and wave energy

The physical cause for shoreline instability can be understood by recalling that, according to the CERC formula, Q is proportional to the product of $H_b^{5/2}$ and $\sin(2\alpha_b)$, where $\alpha_b = \theta_b - \phi$ is the angle between wave fronts at breaking and local shoreline orientation. In this section we disregard the second term in equation (2.3) because simulations with the parameter $r = 0$ showed that this term had little effect on the shoreline evolution (see also section 3.7). By neglecting this term, the gradients in Q only depend on the gradients in $H_b^{5/2}$ and the gradients in $\sin(2\alpha_b)$. Figures 6.2c and g show that in both cases (unstable and stable), the H_b term has its maximum at the updrift flank of the sand wave, favoring instability. On the contrary, the α_b term has its maximum at the lee for both cases, contributing to stability. Therefore, there is in both cases a competition between the wave angle effect (stabilizing) and the wave height effect (destabilizing). For $\theta_0 = 30°$, the alongshore variations in $H_b^{5/2}$ are mild (the maximum is 17% larger than the minimum) while the alongshore variations in $\sin(2\alpha_b)$ are strong (the maximum is 114% larger than the minimum). This has the result that the stabilizing term fully dominates the alongshore distribution of $\partial Q/\partial y$. The contrary occurs for $\theta_0 = 60°$. Now the relative variations in $H_b^{5/2}$ are bigger (57%) while the relative variations in $\sin(2\alpha_b)$ are smaller (31%). As a result, the maximum in H_b causes a shift of Q_{max} in the updrift direction so that the shoreline becomes unstable. Thus, consistently with previous studies (e.g., Ashton & Murray (2006*a*,*b*); Falqués & Calvete (2005); Falqués *et al.* (2011)), this analysis shows that the essential hydrodynamic process triggering high angle wave instability is the difference in refractive energy dispersion between the updrift and the downdrift flanks of the sand waves.

6.3 Wavelength selection

6.3.1 Growth and migration rate as a function of wavelength

Figure 6.4 shows the evolution of the undulating shoreline with $\lambda = 3$ km, which was used in the previous section, for high angle wave conditions ($\theta_0 = 60°$). The undulating shoreline can be seen as a uniform sand wave field. After the initial phase, during which the cross-shore profile adapted to the equilibrium profile, the amplitude of the sand waves increased. Just as in the previous chapters the most updrift sand wave had a lower growth and migration rate and its wavelength increased (see figure 4.3.2). This effect died out further downdrift, where the sand waves grew and migrated uniformly at a constant rate. The wavelength of these sand waves remained constant at $\lambda = 3$ km.

The simulation was also carried out for wavelengths of $1, 2, 2.5, 3.5, 4, 6$ and 10 km. For the simulation with a wavelength of 6 and 10 km a domain size of 40 km was used. The growth and migration rate can be determined for each wavelength by looking at the part of the domain with uniformly evolving sand waves and is calculated as explained in section 3.3. The simulation with $\lambda = 1$ km showed that this length scale was clearly

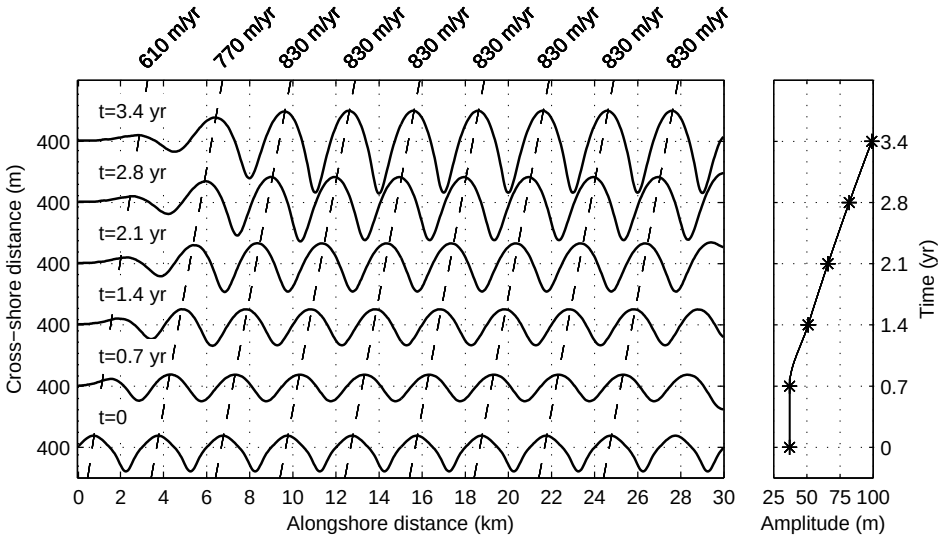

Figure 6.4: Uniform evolution of an undulating shoreline with an initial wavelength of 3 km for default conditions ($\theta_0 = 60°$). The migration celerity of the sand waves is indicated by the dashed lines and the growth of the mean amplitude is plotted in the right panel.

not prone to HAWI because the undulations diffused rapidly within the first 3 months ($\sigma = -8.5$ yr^{-1}). During this period the sand waves migrated downdrift at a rate of 2700 m/yr (figure 6.5b). Figure 6.5a shows the growth/diffusion rate corresponding to the other wavelengths. The undulations with $\lambda = 2$ km still diffused and migrated but at a much lower rate. The simulation with $\lambda = 2.5$ km resulted in a slow growth of the shoreline undulations and it seems that around this wavelength HAWI becomes relevant. This is consistent with the minimum wavelength found with the Fourier analysis for the simulation with random perturbations (see chapter 3) and with the initial wavelength of the spatial-temporal instability (see chapter 4). Interestingly, this was the only wavelength for which the growth of the undulations slowed down after about 3 years and the amplitude seemed to become stable at about 80 m. The fastest growing wavelength was located between 3 and 3.5 km.

For even bigger wavelengths the growth and migration rate decreased slowly. Even though the growth rate was low for $\lambda = 10$ km, HAWI was still relevant at this length scale. Interestingly, this simulation showed smaller scale undulations that started to grow on top of the large scale undulations after about 5 years. The first smaller scale sand wave developed at the downdrift slope of the most updrift sand wave and it triggered the growth of a sand wave train (figure 6.6). The wavelength of these smaller scale sand waves ranged between 2 and 3 km. Because the superimposed sand wave train grew faster in amplitude and propagated faster than the large scale sand waves, it slowly consumed the larger scale sand waves.

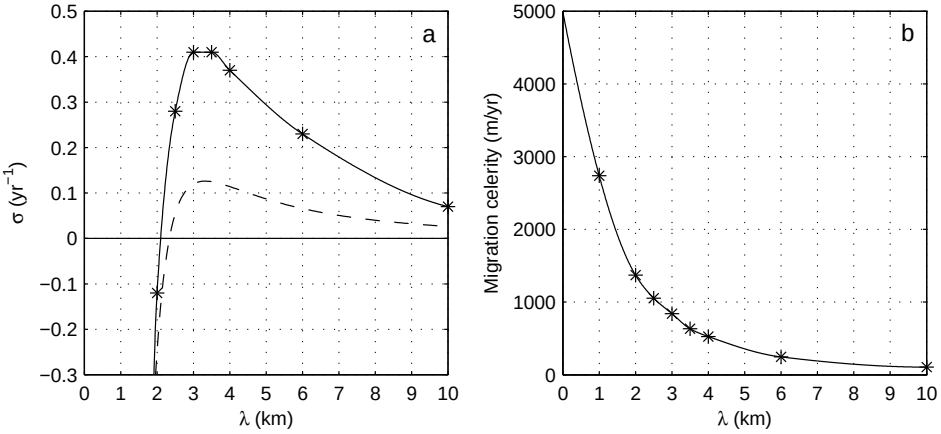

Figure 6.5: (a) The average growth and (b) the migration rate of the sand waves of an initially undulating shoreline as a function of the wavelength of the undulations for default conditions. A negative growth rate indicates diffusion of the sand waves. The dashed line in (a) is the growth curve computed with the linear stability model of Falqués & Calvete (2005) for similar conditions ($xl = 700$).

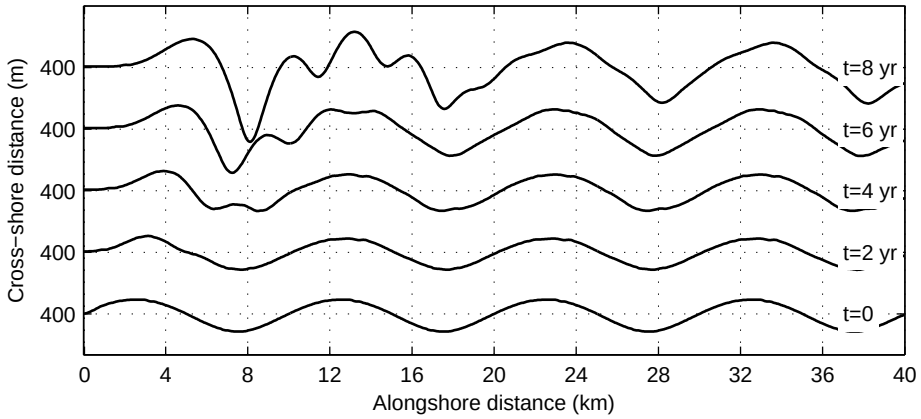

Figure 6.6: The evolution of an undulating shoreline with an initial wavelength of 10 km for default conditions ($\theta_0 = 60°$). The cross-shore distance is exaggerated by a factor 20.

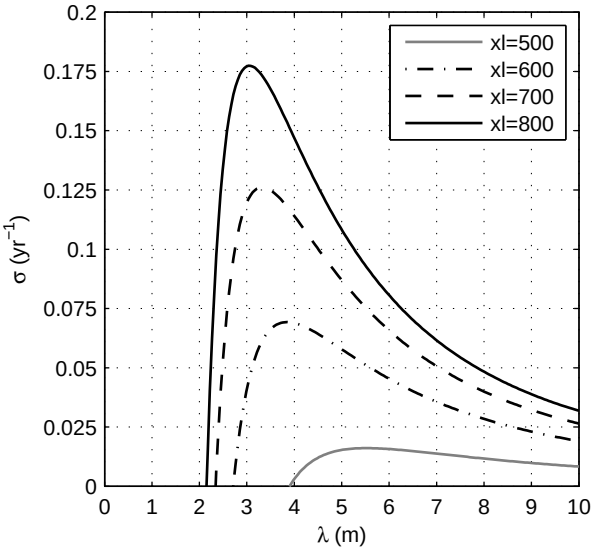

Figure 6.7: Growth rate of the instability as a function of wavelength computed with the linear stability model presented in Falqués & Calvete (2005) with conditions similar to the default simulation. Four different values of the e-folding distance for the offshore decay of the bathymetric perturbation, xl, were used.

6.3.2 Comparison with the growth curve of linear stability model

It is interesting to compare the growth curve of figure 6.5a with the predictions of the linear stability model of Falqués & Calvete (2005). To this end, the linear model was applied with the bathymetry and the wave forcing of the default experiment. It is important to keep in mind that in addition to linearity, this model assumes instantaneous coupling between changes of the shoreline and the bathymetry, while Q2D-morfo considers the dynamics of the cross-shore profile. In the linear model, the coupling between shoreline and bathymetry is controlled by the e-folding distance of the offshore decay of the bathymetric perturbations, xl. Figure 6.7 shows the growth rate against the wavelength for different values of xl. For $xl = 400$ there was no instability and for the other simulations the dominant wavelengths were in the range of $\lambda = 3.1 - 5.5$ km (table 6.1). The dominant wavelength increased slightly with a decreasing xl. However, for $xl = 500$ the dominant wavelength was larger ($\lambda = 5.5$ km) and the growth rate was relatively low. This is actually about the distance of the offshore extent of the perturbations in the default simulations with Q2D-morfo. Therefore it seems that the bathymetric perturbations in Q2D-morfo are more effective in triggering HAWI under these conditions than an equivalent xl in the linear model. Even when comparing with the higher values of xl, the growth rate of the linear stability model is a factor 3 lower and the migration celerity is one order of magnitude larger than predicted with Q2D-morfo. The growth curve for $xl = 700$ is is also plotted in figure 6.5a to show that the curves are qualitatively similar and the typical wavelength for HAWI was similar for high values of xl.

Table 6.1: Results of the linear stability model presented in Falqués & Calvete (2005) with conditions similar to the default simulation and different values of the e-folding distance for the offshore decay of the bathymetric perturbation, xl.

xl (m)	λ (km)	σ (yr^{-1})	v (km/yr)	D_{xl} (m)	θ_{xl} (deg)
400		no instability		6.6	47.6
500	5.5 km	0.016	3.3	7.8	51.5
600	3.8 km	0.069	6.6	8.9	54.8
700	3.3 km	0.13	9.0	10.0	57.6
800	3.1 km	0.18	10.8	11.0	60

6.3.3 Wavelength selection explained

In section 6.2 we discussed the physical mechanism behind shoreline instability but neither the existence of a minimum length scale for the development of shoreline sand waves, nor the shape of the growth curve presented in figure 6.5a were explained. Falqués & Calvete (2005) discussed the existence of a preferred wavelength for instability in the linear regime but only provided an explanation for the minimum wavelength. Their analysis showed that for very small length scales the maximum of H_b was located downdrift of the crest and therefore the position Q_{max} was located downdrift of the crest, which leads to diffusion. List & Ashton (2007) predicted alongshore transport gradients with a process-based circulation model and also suggested the existence of a minimum alongshore length scale for HAWI. In their simulations the cross-shore extent of the shoreline undulation was related to the length scale of the undulation. An undulation with a short wavelength extended into the bathymetric lines up to a relative small water depth. Instability did not occur because the wave angle had decreased below the critical value before reaching the bathymetric perturbation. The occurrence of a minimum length scale in their simulations was therefore related to the criterion for HAWI (see section 3.5). The simulations in the previous section however show that the wavelength selection occurs independently from this cross-shore effect. The growth and diffusion rates varied with the alongshore length scale of the undulations, while the depth of closure and the wave angle at the depth of closure was similar for all length scales.

In order to understand the existence of a preferred wavelength for HAWI we look at how the position of the extrema of H_b, α_b and Q relative to the crest change with the wavelength. Figure 6.8 shows the shoreline of a sand wave with a normalized alongshore distance, where 0 indicates the position of the crest and -1 (1) the position of the updrift (downdrift) trough. We can now determine the relative position of Q_{max} and Q_{min} along an undulating shoreline for different wavelengths (without morphological evolution). The undulations have a small amplitude with a fixed ratio, $2A/\lambda = 0.012$, so that non-linear effects are negligible. They extend into the bathymetry until about 9 m depth and, in combination with the default high angle wave conditions, this would lead to instability for the appropriate wavelengths. The horizontal bars above the normalized sand wave indicate the zones of erosion and deposition for the different wavelengths and the transition from erosion (deposition) to deposition (erosion) corresponds to the position of Q_{max} (Q_{min}). The vertical lines indicate the relative position of the extrema of H_b and α_b.

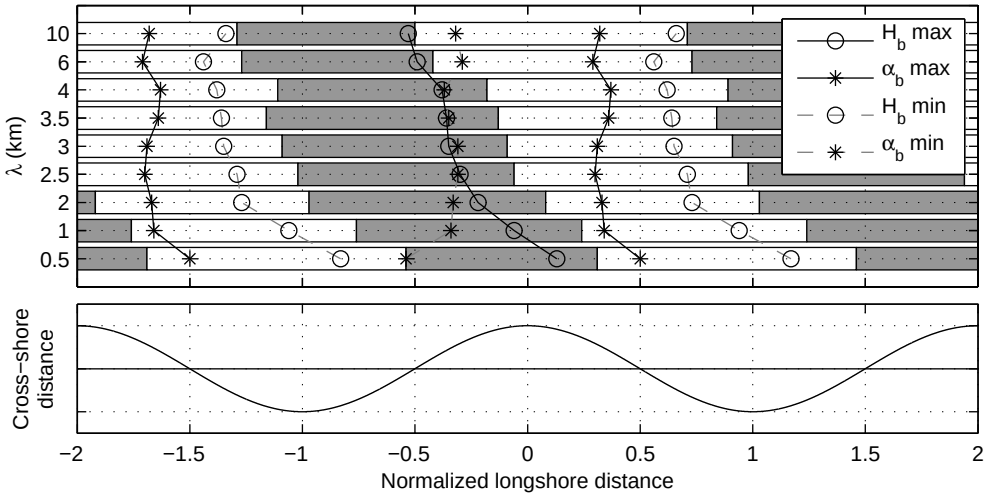

Figure 6.8: The alongshore position of the extremes of Q, H_b, α_b relative to the position of the crest of a shoreline sand wave were determined for simulations with an undulating shoreline with different wavelengths. The lower panel shows a shoreline sand wave with a normalized alongshore distance. The bars above show, for each wavelength, the zones of erosion (gray, $\frac{\partial Q}{\partial y}$ =positive) and deposition (white, $\frac{\partial Q}{\partial y}$ =negative). The transition from erosion (deposition) to deposition (erosion) corresponds with the position of Q_{max} (Q_{min}). The vertical lines indicate the extremes of H_b and α_b.

For $\lambda = 0.5$ km the alongshore transport pattern is similar to the pure diffusive pattern that we know from low angle waves or the traditional one-line approach. Q_{max} is located slightly updrift of the inflection point, which results into downdrift migration. Just as found by Falqués & Calvete (2005), the position of the maximum of H_b is located downdrift of the crest for this small wavelength. Even though for $\lambda = 1 - 2$ km the maximum of H_b moves updrift of the crest, the relative variations of $\sin(2\alpha_b)$ are still strong enough to keep the position of Q_{max} downdrift of the crest. Consistently with figure 6.5a, Q_{max} moves updrift of the crest for $\lambda = 2.5$ km, leading to a shift from diffusion and migration to growth and migration. This shift is caused by the further updrift displacement of the maximum of H_b and by the increased importance of the relative variations of $H_b^{2.5}$ (the position of Q_{max} moves closer to the maximum of H_b). The combination of these two effects explains the existence of a minimum wavelength. The updrift displacement of the maximum of H_b is the result of a shift from the dominance of wave focusing at the crest for small wavelengths (maximum H_b close to crest) to the dominance of wave energy dispersion due to refractive wave crest stretching for large wavelengths (maximum H_b on updrift slope). The increase of the importance of the variations of $H_b^{2.5}$ (for $\lambda = 10$ km the position of the extrema of Q and H_b almost coincide) results from the increase of relative variations of $H_b^{2.5}$ together with the decrease of relative variations of $\sin(2\alpha_b)$.

Even though the updrift displacement of Q_{max} for increasing wavelength explains the existence of a minimal length scale for instability, it contradicts the decreasing growth

rate for larger wavelengths. However, the growth or diffusion rate of the undulations does not only depend on the pattern of the alongshore transport, it also depends on the magnitude of the alongshore gradients. Large transport gradients lead to a higher rate of growth or diffusion. For a given amplitude, the relative variations of Q (ΔQ) decrease for increasing wavelengths because the difference between the maximum and minimum values of α_b and H_b decrease. Moreover, the transport gradients are proportional to $\Delta Q/L$. Therefore, when the length scale L becomes very large, the growth rate tends to zero. This explains the decrease in growth rate for increasing wavelength and thereby the the existence of an optimal wavelength for instability. Migration takes place for all wavelengths (see figure 6.5b) and the decrease of the migration rate with increasing wavelength can also be explained by the decreasing alongshore gradients in Q. This is in line with the general assumption that the dynamics of relatively large sandy features are slower (Sonu, 1968).

6.3.4 Wavelength selection explained with linear stability model

The physical mechanism behind wavelength selection was further explored in van den Berg *et al.* (2011*c*) with the use of the linear stability model of Falqués & Calvete (2005). Here, only the main results are presented and these are compared with the results that were obtained with the Q2D-morfo model. In addition, they explored the sensitivity of the wavelength selection to parameters like the cross-shore slope, the wave height, period and incidence angle and they showed that the optimal wavelength does not depend on the width of the surf zone as was suggested in previous studies.

The linear stability analysis was used to explore the initial tendency of the development of shoreline sand waves. In the end of section 6.3.1 we presented growth curves computed with this linear model and this showed that for similar conditions both models predicted a minimum wavelength between 2 and 3 km, an optimum wavelength between 3 and 4 km and decreasing growth rates for higher wavelengths. van den Berg *et al.* (2011*c*) used the same approach as in section 6.3.3 to study the position of the extrema of Q, H_b and α_b for different wavelengths. The results are presented in figure 6.9a (using $xl = 700$ m). The resemblance with figure 6.8 is striking and this confirms the conclusions of section 6.3.3. Because the undulations were symmetrical and non-linear effects were not present, the tendencies were clearer than for the Q2D-morfo results. Figure 6.9b shows the same analysis for low angle wave incidence. Even though the maximum of H_b shifts to the updrift side of the crest for bigger wavelengths, Q_{max} remains on the downdrift side and the shoreline remains stable. This is the result of the relative high gradients in α_b which dominates the position of Q_{max} for these low angle wave conditions.

The position of the maximum of H_b is crucial for the development of HAWI and it was discussed in section 6.3.3 that this position is determined by the competition between wave energy focusing at the crest and wave energy dispersion due to the stretching of the wave crests, which leads to higher wave energy at the updrift flank of the undulation. The first process seems to be dominant for small wavelengths and the latter for big

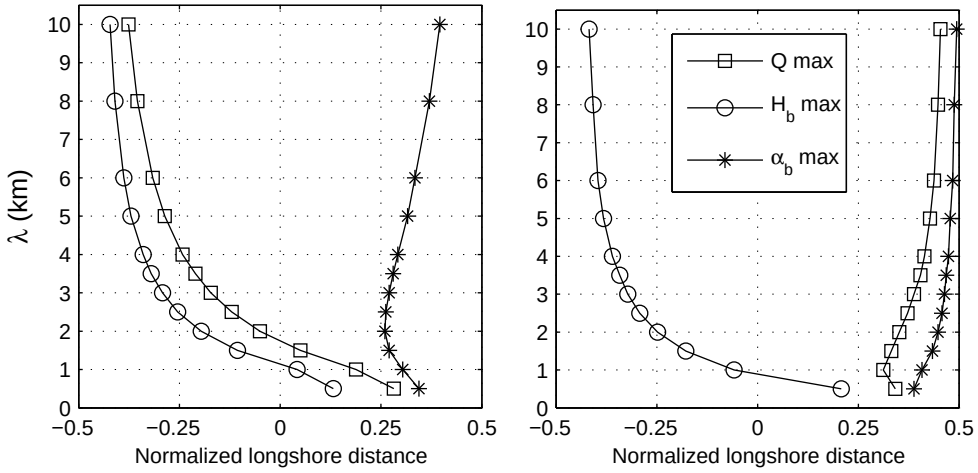

Figure 6.9: The alongshore location of the maxima of Q, H_b and α_b relative to the position of the crest, as a function of the wavelength, computed with a linear stability model. Left panel: unstable conditions ($\theta_0 = 60°$), right panel: stable conditions ($\theta_0 = 30°$).

wavelengths. To illustrate this effect, van den Berg *et al.* (2011*c*) estimated the relative importance of these two effects as a function of the wavelength. They isolated the two effects and first looked at the intensity of wave focusing for different wavelengths under normal wave incidence. The difference in the wave height between the crest and the trough was defined as ΔH_{foc}. It was assumed that the results of the linear model, which in theory are only valid for amplitudes tending to zero, could be extrapolated to an amplitude of 10 m. Second, the intensity of wave energy dispersion was estimated by computing the wave height for the updrift flank by assuming refraction over a rectilinear bathymetry with a wave incidence angle equal to $\theta_0 - \phi$ and similarly for the downdrift flank with $\theta_0 + \phi$. The difference in wave height between the updrift and the downdrift flank was defined as ΔH_{dis}. Figure 6.10 shows that the ratio $\Delta H_{dis}/\Delta H_{foc}$ is nearly 1 for small wavelengths and it increases up to about 10 for $\lambda = 10$ km. Thus, both effects were comparable for small wavelengths but the wave energy dispersion effect became dominant for increasing wavelengths. Both ΔH_{dis} and ΔH_{foc} decreased for increasing wavelengths but ΔH_{foc} decreased faster.

Sensitivity tests showed that the optimal wavelength for sand waves formation was inversely proportional to the mean cross-shore slope β. Figure 6.11 shows the optimal wavelength as a function of β^{-1} for several wave conditions and a planar profile. The relation with the wave period was less clear. In general the optimal wavelength increased for higher values of T_p but only for very idealized situations (planar profile and a large depth of closure) there was a linear relationship between T_p and the optimal wavelength. H_0 only had an influence on the optimal wavelength for high values of T_p and higher waves led to a bigger wavelength. The relation between the optimal wavelength, β and T_p can also be demonstrated by scaling the wave equations (2.17), (2.18) and (2.19).

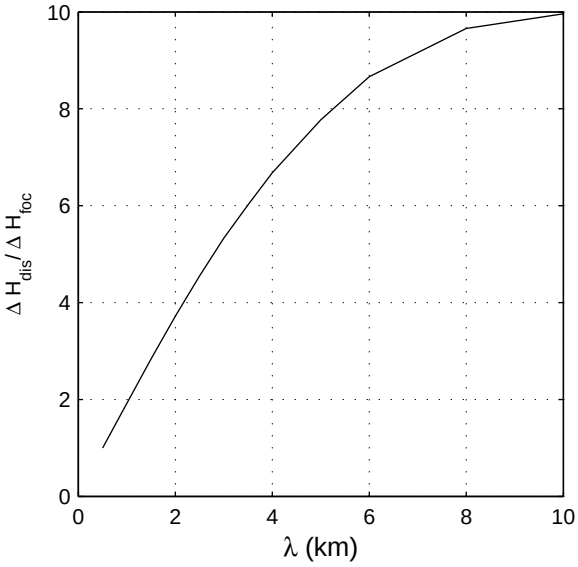

Figure 6.10: Relative influence of the wave energy dispersion versus wave energy focusing, measured by the ratio $\Delta H_{dis}/\Delta H_{foc}$, as a function of wavelength, λ.

This gives the optimal alongshore length scale

$$\lambda_y = \frac{L_0}{\beta} \quad , \tag{6.1}$$

where L_0 is the wavelength of the water waves. The details of the scaling can be found in van den Berg *et al.* (2011*c*). Equation (6.1) gives some idea of the range of wavelengths that can be expected on a real coast. For a mild cross-shore profile with $\beta = 0.01$ and high angle wave conditions with $T_p = 5 - 7$ s, a dominant wavelength in the range of $4 - 8$ km is expected. For steeper profiles and shorter waves, the wavelength will be smaller. A profile with $\beta = 0.03$ and high angle wave conditions with $T_p = 3$ s would result into a dominant wavelength of about 0.7 km.

6.3.5 Absence of wavelength selection in previous studies

The exploration in this section provides an explanation to why the model of Ashton *et al.* (2001) does not predict a minimal wavelength for HAWI. Their model does not include the effect of curvilinear bathymetric lines and therefore it does not include the effect of wave focusing. For unstable conditions, it predicts that for every wavelength the position of the maximum of H_b is located updrift of the crest. Consequently, Q_{max} is also located updrift of the crest and perturbations would grow independently of their wavelength. Figure 6.12 shows the transport gradients along an undulating shoreline with a wavelength of 1 km and it shows that the Q2D-morfo approach predicts diffusion and migration, while the Ashton&Murray approach predicts growth and migration.

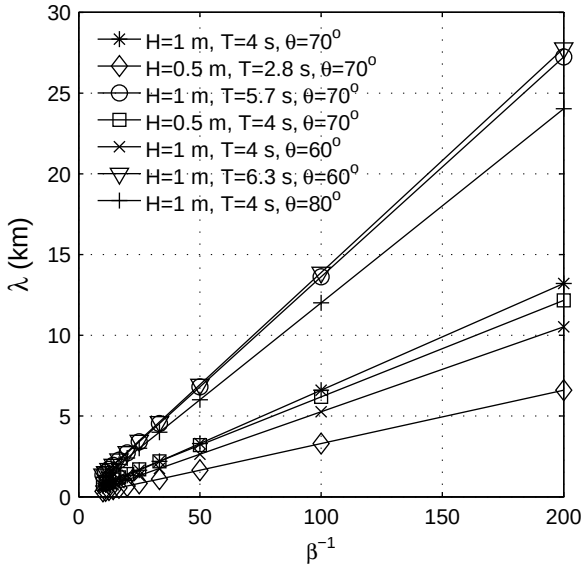

Figure 6.11: The wavelength, λ, as a function of the inverse of the beach slope, β^{-1}, for the idealized beach geometry and various wave conditions. The symbols represent the model results and the solid lines are the corresponding linear fit.

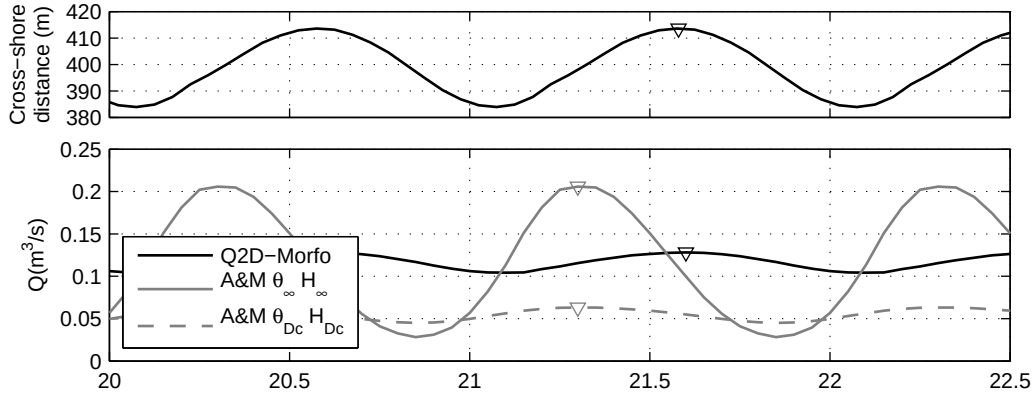

Figure 6.12: The shoreline position of an undulating coast with $\lambda = 1$ km (top panel). The alongshore distribution of the sediment transport rate Q for the Q2D-Morfo approach, the Ashton&Murray approach using the wave angle and height at deep water and the Ashton&Murray approach using the wave angle and height at the depth of closure for unstable conditions. The symbol ∇ indicates the maxima of the shoreline position and Q.

The effect of decreasing growth rates for increasing wavelengths, which leads to an optimal wavelength, should in principle be reproduced by their model. However, their model predicts a continuous coarsening of the shoreline features. Even if the model would predict a wavelength with a maximum growth rate, this wavelength would not persist The coarsening is related to the merging of sand waves (smaller sand waves migrate faster and merge with their bigger neighbours) and to the inclusion of an artificial 'wave shadowing' mechanism (Ashton & Murray, 2006*a*). The wave shadowing mechanism describes how relatively large amplitude shoreline features shadow their smaller neighbours from high angle waves. As a result, the smaller shoreline features diffused and the length scale of the shoreline features increased. The wave shadowing mechanism leads to a certain ratio between the wavelength and amplitude of shoreline features but not to an optimal wavelength. This mechanism was included because their model does not compute the actual wave field, it computes the alongshore transport directly as a function of the deep water waves and the local shoreline orientation (see section 1.3.1). Without the wave shadowing mechanism the model would not include the effect of adjacent shoreline features. However, this wave shadowing effect only seems reasonable in case of very large scale or asymmetrical features. In the present study the shoreline undulations were still relatively smooth features. The shoreline undulations affected their neighbours through their effect on wave refraction and the resulting wave field and alongshore sediment transport gradients. The formation of sand waves in the present model is therefore a fully self-organized mechanism. The relative low wave energy downdrift of a shoreline undulation due to refraction can be seen as a mild form of wave shadowing but this does not lead to a coarsening of the wavelength.

6.4 Spatial-temporal instability

In chapter 4 we discussed the development of a sand wave train, downdrift of a localized shoreline perturbation. The development of this spatial-temporal instability was explained by a chain-reaction in the alongshore sediment transport. Here we look at the alongshore gradients of Q and H_b to illustrate this chain-reaction.

Figure 6.13 shows the wave height and the alongshore gradients of Q for a localized shoreline perturbation similar to the one used in section 4.2 but with an offshore extent up to 9 m water depth. The default model settings were used with $\theta_0 = 60°$. Figure 6.13a shows the transport pattern at $t = 0$, which illustrates the initial development of the spatial-temporal instability. It can be seen that Q_{max} is located downdrift of the crest which leads to diffusion and migration of the perturbation. A minimum in Q occurs at the end of the downdrift flank. This marks the end of the zone where deposition takes place and it is a consequence of the low wave energy at the downdrift flank due to wave dispersion. It can be seen that the wave energy increases when the shoreline becomes rectilinear again. This leads to a positive transport gradient downdrift of the perturbation, which would result into erosion and the formation of an erosional zone or through. This transport pattern was also found with a process based model by List & Ashton (2007) and is consistent with the qualitative description by Inman (1987).

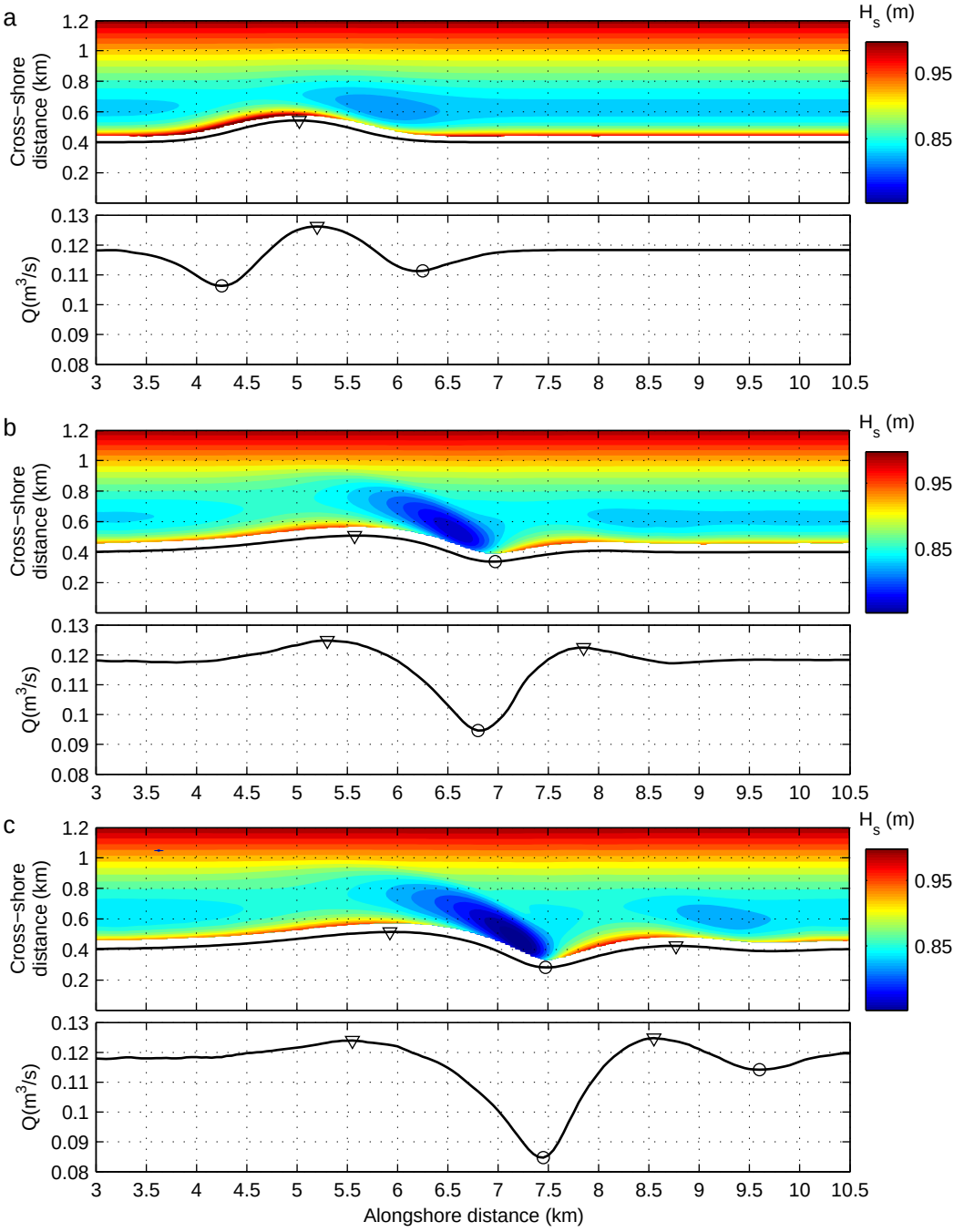

Figure 6.13: This figure illustrates the initial development of the spatial-temporal instability at (a) $t = 0$, (b) $t = 0.5$ yr and (c) $t = 1$ yr. The contour plots show the wave height up to breaking for a coast with a localized perturbation and $\theta_0 = 60°$. The shoreline is indicated by the black line and the waves come from the left. In the panels below, the alongshore distribution of the sediment transport rate Q is plotted. The symbols ∇ and o indicate the maxima and minima of the shoreline position and of Q.

Figure 6.13b shows the transport pattern at $t = 0.5$ yr. Q_{max} is now located updrift of the crest of the perturbation, as would be expected for these unstable conditions. As a consequence, the perturbation grew in amplitude and migrated downdrift. It can be seen that a through formed downdrift of the perturbation, just as the transport pattern predicted at $t = 0$. The minimum of Q is located slightly updrift of the trough, which is needed for the growth of the through. A secondary Q_{max} can now be seen at the end of the downdrift flank of the through. This secondary maximum is a consequence of the increase of the wave energy, which results from the relative low wave energy dispersion on this flank. Further downdrift the wave energy is slightly lower at the rectilinear shoreline and this results into a negative transport gradient, which would lead to deposition downdrift of the through. Figure 6.13c shows the transport pattern at $t = 1$ yr. A new crest was formed downdrift of the through and this new crest in its turn triggers the development of a through and so on.

The spatial-temporal instability is a self-organized process, which results from the feedback between the changing bathymetry, the wave field and the sediment transport. The length scale at which the new downdrift sand waves form can be explained by the mechanisms discussed in section 6.3 and would therefore depend mainly on the slope of the cross-shore profile and the wave period. The spatial-temporal instability is expected to be dominant on coasts with a clear localized perturbation and very unstable conditions. An indication for its occurrence could be a series of sand waves with a decreasing amplitude in downdrift direction. On a coast where HAWI is not so strong, i.e. with considerable fraction of low angle waves, the development of the sand wave train might be limited up to a situation where only a downdrift erosional zone is formed (see section 5.2.2). In the context of spontaneous sand wave formation, the spatial-temporal instability is not relevant because the sand waves form in unison. However, on a real coast there could be a confluence of spontaneous sand wave formation and the spatial-temporal instability.

6.5 Discussion

6.5.1 Model limitations

The Q2D-Morfo model has several limitations and even though some of these can be overcome it must be kept in mind that the aim of the model is to give qualitative predictions of large scale shoreline dynamics at a relatively low computational cost, including only the most essential processes.

The wave field is computed with a relatively simple approach based on linear wave theory, assuming regular and unidirectional waves. The method does not include wave diffraction, wave dissipation due to wave breaking of irregular waves or wave-current interaction. The model can also use an external wave module to compute the wave field. This option could be used to validate the results obtained with the Q2D-Morfo model. The model is prepared to use the Ref/Dif model (Kirby & Dalrymple, 1994) as

an external wave module and some test have been done. Ref/Dif uses the parabolic mild slope equation, assumes irregular waves and includes diffraction and dissipation due to wave breaking and due to bottom shear stresses. However, this model has an important limitation for the present application; numerical errors develop for very oblique wave incidence. An alternative could be the spectral wave model SWAN (Booij *et al.*, 1999). A more realistic wave model could be useful, not only for validation, but it would also make the model more flexible for the use with complex bathymetries, complex shoreline shapes and coastal structures. It would however lead to longer computation times. Three examples of studies on HAWI that include more processes in their wave model are: Uguccioni *et al.* (2006) (irregular waves and dissipation due to wave breaking), Barbaro *et al.* (2010) (analytical model taking into account the wave spectrum) and List & Ashton (2007) (SWAN).

The Q2D-Model computes the total integrated alongshore transport rate with the empirical CERC formula. This requires only the wave height and relative wave angle at breaking and the model uses a cross-shore shape function for the alongshore transport flux (see section 2.2.1). Besides the limitations of the CERC formula for quantitative predictions (Cooper & Pilkey, 2004), the present approach may also have some limitations for qualitative predictions of shoreline evolutions. This approach does not use the actual cross-shore distribution of the alongshore current and it does not include the effect of the inertia of the alongshore current or a possible delay in sediment entrainment by the alongshore current (Uguccioni *et al.*, 2006). Furthermore, the second term included in the CERC formula might not describe correctly the effect of alongshore variations in wave setup (List *et al.*, 2008). An improvement would be to compute the actual alongshore current from the radiation stresses and include the effect of alongshore gradients in wave setup. The alongshore sediment transport could then be computed directly from the alongshore current using for example the Bailard formulation (Bailard, 1981) or the total load formulation of Soulsby and van Rijn (Soulsby, 1997). It would be interesting to compare the results of this more realistic approach with the present approach. Two existing studies, that use a more realistic approach, show that the HAWI mechanism is not essentially affected by the idealizations of the present study (Uguccioni *et al.*, 2006; List & Ashton, 2007). However, small differences might arise in the alongshore transport patterns, which can be especially important for the wavelength selection mechanism and for situations where the coast is on the edge of instability.

The Q2D-morfo model includes cross-shore dynamics, which is based on the assumption that on long time scales the profile tends to an equilibrium shape. Because of this, the details of the wave driven cross-shore transport processes can be ignored and a relatively simple and computationally efficient parametrization can be chosen. As an initial approach a diffusive transport was used, which leads to the adaptation of the cross-shore profile to a predefined equilibrium profile (see section 2.2.2). In the future it would be interesting to include other cross-shore transport parameterizations, which predict an equilibrium profile based on physics and that give a more physically based magnitude of the cross-shore transport and its cross-shore distribution (including the related depth of closure). For example the semi-empirical model of Plant *et al.* (2001) could be implemented.

In the present version of the model the equilibrium profile is defined perpendicular to the y-axis, which makes sense for undulations with small amplitudes. As a consequence the cross-shore transport flux is also directed perpendicular to the y-axis. However, when the amplitude increases, the angle between the shoreline and the y-axis increases and at this point it would more appropriate to define the equilibrium profile and the cross-shore transport perpendicular to the shoreline orientation. The transport would then not be simply onshore/offshore but up-slope/down-slope. In order to achieve this, the adaption of the profile to an equilibrium profile should be changed into the adaption of the profile slope to an equilibrium slope. A relatively simple adjustment of equation (2.2.2) could make this possible and would improve the model. The transport flux could then be computed as a diffusivity coefficient multiplied with the difference between the local profile slope and the equilibrium slope, which is a function of the water depth. The transport flux could then be applied in a direction perpendicular to the local orientation of the bathymetry. When the local slope was bigger than the equilibrium slope, the sediment flux would be directed down-slope and when the local slope was smaller than the equilibrium slope, the sediment flux would be directed up-slope.

An important limitation of the model is the constriction on the angle between the shoreline orientation and the y-axis (see section 2.4.2). The constraint of $|\tan\phi_s| \lesssim 2\Delta x/\Delta y$ poses a limit to the amplitude and asymmetry of the shoreline sand waves. When the amplitude of the sand waves become relatively big, the model results become unreliable and big jumps develop in the shoreline at the downdrift flanks of the sand waves. This makes it impossible to continue the simulations and to see how the shoreline sand waves would develop further. It is not exactly clear where this constraint originates from but most likely the boundary condition at the shoreline and/or the sediment transport formulations close to the shoreline must be improved.

6.5.2 Finite amplitude behaviour

In most of the simulations the growth of the shoreline sand waves was exponential due to the positive feedback between the morphological changes and the wave field. When the amplitude of the sand waves increased, the alongshore gradients in H_b and α_b increased and consequently the gradients in alongshore transport increased, which led to faster morphological changes. As discussed in the previous section the model is not capable of describing sand waves with a relatively big amplitude and therefore it remains unclear if the processes included in the model would predict a saturation of the growth (finite amplitude). An exception to this are the simulations with a lower fraction of high angle waves, where the low angle wave contribution dampens the sand wave growth (see chapter 5). However, in some simulations with constant high wave incidence angle, there was also tendency to saturation of the growth. In chapter 4 the increase of the amplitude of the sand waves further downdrift in the sand wave train seemed to slow down. Something similar was found for the simulations with an undulating shoreline with $\lambda = 2.5$ km in section 6.3.1. These simulations have in common that λ was relatively small and that it did not increase. In simulations where λ is bigger or where it increases together with the amplitude, the amplitude of the sand waves increases exponentially. Therefore, it seems

that for a high aspect ratio (total amplitude divided by λ) the sand waves can reach an finite amplitude. Because the magnitude of the gradients remain high, a mechanism must exists, which shifts the alongshore transport pattern from unstable to stable for high aspect ratios.

A mechanism for the saturation of sand wave growth could be the competition between wave energy focusing at the crest and wave energy dispersion due to the stretching of the wave crests. This competition was used to explain the existence of a minimal length scale for sand wave formation in section 6.3.4 and it depends on the curvature of the bathymetric contours, which is related to the aspect ratio of the sand waves. For high aspects ratios wave energy focusing might become increasingly important, moving Q_{max} downdrift, eventually leading to a shift from instability to stability. It can therefore be argued that if a certain wavelength is initially unstable for a relatively small amplitude (Q_{max} located updrift of the crest), it might become stable for a relatively large amplitude (Q_{max} located at or downdrift of the crest). A more detailed study of the finite behaviour of shoreline sand waves requires model improvements that enable for simulations with bigger aspect ratios.

6.5.3 The bathymetry associated with shoreline sand waves

In both the simulations with a localized perturbation and in the simulations with an undulating shoreline it took some time before the bathymetry became optimal for HAWI. During the first months of the simulations the perturbations diffused despite of the high angle wave conditions. One reason for this is the adaptation of the cross-shore profile, which took place during the first months. The cross-shore dynamics redistributed sediment between the shoreline and the depth of closure. As a result the perturbation reached the water depth where the wave incidence angle was bigger than the critical angle for HAWI (see section 4.3.1). In addition, the adaptation of the cross-shore profile might hide a net input of sediment in the cross-shore profile at the crest of the perturbation because sediment is transported from the upper part of the profile to the lower part. Therefore there might be deposition in the surfzone at the crest of the perturbation even though an increase in amplitude of the perturbation at the shoreline is not observed yet.

A second factor that might contribute to an optimal configuration of the bathymetry for HAWI is the shape of the bathymetric lines. In the studies of Ashton *et al.* (2001); Falqués & Calvete (2005); Uguccioni *et al.* (2006) the bathymetric lines were assumed to follow the curvature of the shoreline. In the Q2D-model the two dimensional approach and the cross-shore dynamics allow for a deviation from the curvature of the shoreline. Figure 3.4 and 6.1 show that the crest of the bathymetric undulations bend in the direction of the waves. The development of this phase lag between the depth contours and the shoreline is illustrated in figure 6.14 (simulation used from section 6.2). Initially there is no phase lag but after 3.4 years, the contour line at 5 and 7 m water depth developed a phase lag of about 100 and 300 m respectively. A closer look at the cross-shore profile at the crest, 300 m updrift of the crest, and at the updrift through shows that the phase lag is caused by the slower response of the cross-shore profile at greater water depths (figure

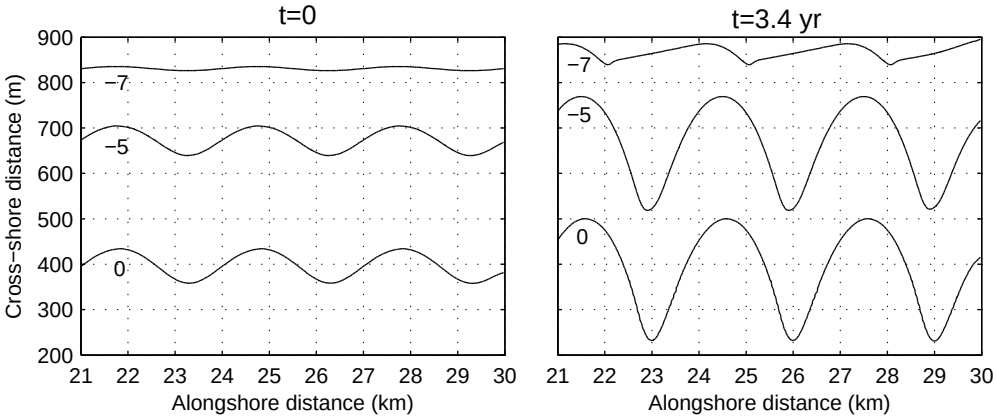

Figure 6.14: The depth contours of an undulating coastline with $\lambda = 3$ km at $t = 0$ (left panel) and $t = 3.4$ (right panel).

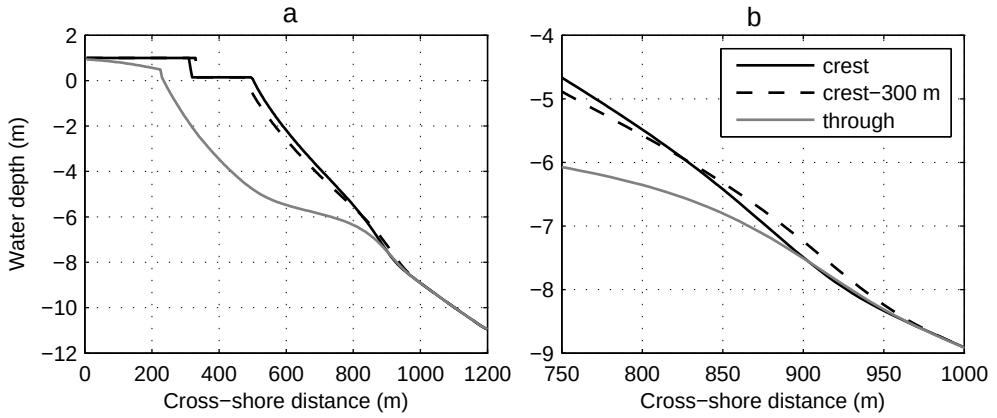

Figure 6.15: (a) Three cross-shore profiles of an undulating shoreline with $\lambda = 3$ km at $t = 3.4$ yr. (b) A section of the cross-shore profiles around the depth off closure.

6.15). As a result the bathymetric profile at the actual crest of the shoreline undulation reaches up to a smaller water depth than at a few hundred meters updrift. At the latter position the perturbation reached a maximum water depth, even though the profile was already eroding at the upper part of the profile. The phase lag of the contour lines at greater water depth is expected to favor HAWI. It depends on the cross-shore distribution functions of the alongshore transport and the diffusive alongshore transport (see section 2.2) and it would play a more important role if variable wave conditions were used.

Even though the cross-shore dynamics in the model is highly simplified, the develop-

ment of a phase lag might not be unrealistic. On a natural coast the fastest changes take place in the surfzone and the cross-shore profile at greater water depth adapts slower. However, little is known about the bathymetry of shoreline sand waves on real coasts. A recent analysis of shoreline undulations and the related bathymetry on the west coast of Denmark shows that some shoreline undulations are correlated with undulations in the bathymetry up to 5 m water depth (Kaergaard *et al.*, 2011). They observed a phase lag of the 5 m water depth contour line of about 1000 m in downdrift direction. This is opposite to our modeling results where the phase lag of the bathymetric contours is always in updrift direction. More field observations are needed to confirm the correlation between the shoreline undulations and the bathymetry and the direction of a possible phase lag.

Two other factors that might be important for the feedback between the morphology and the wavefield are the asymmetry of the undulations (relatively steep downdrift flank) and the difference in the profile shape at the trough and the crest (steep at the crest and shallow with a terrace at the through). Both the asymmetry and the difference between the profile at the crest and the slope increase when the sand waves grow.

6.6 Conclusions

An analysis of the pattern of the alongshore transport Q, the wave height and the relative wave angle along an undulating coastline gave more insight into the instability mechanism and wavelength selection. The growth or decay of shoreline sand waves and their migration depend on the alongshore distribution of Q, which can be characterized by the location of its maximum relative to the crest of the sand wave.

Consistently with the HAWI theory, Q_{max} was located downdrift of the crest for low wave incidence angles and slightly updrift of the crest for high wave incidence angles. For both low and high wave incidence angle, the maximum of H_b was located updrift of the crest and the maximum of α_b downdrift of the crest, close to the inflection point. For low angle wave incidence the gradients of α_b were dominant and therefore Q_{max} was located close to the inflection point (creating sand wave diffusion). In line with previous studies it was found that for increasing wave incidence angles, the relative importance of the gradients in H_b increased, which moved the position of Q_{max} in a updrift direction (sand wave diffusion and migration). Above the critical wave incidence angle, Q_{max} moved updrift of the crest leading to the growth of the sand waves along with downdrift migration. The underlying physical mechanism of HAWI is the wave energy dispersion due to wave refraction, which leads to a maximum in H_b on the updrift flank and a minimum at the downdrift flank.

Applying a method similar to that of Ashton *et al.* (2001) shows that their approach overestimates instability, not only due to their assumption on the cross-shore extent of the perturbations but also because they do not take into account the curvature of the bathymetric lines. The curvature of the bathymtric lines leads to wave energy focusing at the crest. This effect competes with the wave energy dispersion and moves the position

of Q_{max} closer to the crest, which results into a less unstable transport pattern.

It was found that undulations with small length scales diffused even under high angle wave conditions. Below a minimum wavelength of the undulations, the alongshore transport pattern shifted from growth and migration to diffusion and migration. This can again be explained by the competition between the gradients in H_b and α_b. The maximum of α_b was located near the downdrift inflection point for all length scales. However, the position of the maximum of H_b moved significantly depending on the length scale. For short sand waves, this maximum was located slightly downdrift of the crest and as a result Q_{max} was located downdrift of the crest, which led to diffusion. For longer sand waves the maximum in H_b moved updrift of the crest and in addition, the relative importance the gradients in H_b increased. This shifted Q_{max} updrift and resulted into sand wave growth. The underlying physical mechanism for the occurrence of a minimal wavelength is the competition between wave energy dispersion and wave focusing. The latter is more important for small length scales and moves the maximum in H_b close to the crest and the first becomes more important when the wavelength increases and moves H_b further updrift. On the other hand, it was found that the alongshore gradients in Q decrease monotonically for increasing wavelengths. As a result the sand wave growth rate tends to zero for large wavelengths and this explains the occurrence of an optimal wavelength for sand wave growth.

A linear model was used to confirm the mechanism of wavelength selection and it was used to study the dependence of the wavelength selection on various parameters. The experiments showed that the optimal wavelength for sand wave formation is inversely proportional to the mean profile slope. The relation with the wave period was less clear but in general the optimal wavelength increased for higher values of T_p. Contrary to previous studies it was found that the width of the surf zone does not affect the optimal wavelength.

The analysis of the alongshore transport gradients along a localized perturbation confirmed that the spatial-temporal instability developed from a chain-reaction in alongshore transport.

Several improvements of the Q2D-model were suggested. The most important one is be to overcome the limitation on the shoreline orientation, which would make it possible to describe sand waves with larger amplitudes and to investigate if the sand waves would attain a finite amplitude. Some simulations suggest that the competition between wave focusing and wave dispersion could provide a mechanism leading to saturation of the growth for a certain aspect ratio. Wave focusing becomes more important if the curvature increases, which would move Q_{max} to the crest and slow down the growth.

The basis of the mechanisms described in this chapter is the feedback between the bathymetry and wave field. Several characteristics of the bathymetry are expected to influence this feedback. The most important one is the cross-shore extent of the undulations but other ones are the presence of a possible phase lag between the shoreline and the depth contours, the asymmetry of the sand waves and the difference between the shape of the profile at the through and at the crest. However, little is known about the

bathymetry of shoreline sand waves on real coasts and more observations are required to validate and improve the model predictions.

Chapter 7

Qualitative comparison with observations

7.1 Introduction

The role of high angle wave instability in the formation and dynamics of sand waves along natural coastlines is difficult to ascertain due to: i) the large length and time scale involved, ii) the scarcity of systematic measurements at these scales and iii) the confluence of other processes that may also be important for the dynamics of shoreline undulations. Point (i) has as a consequence that shoreline sand waves are difficult to observe in the field. Aerial and satellite pictures can be useful tools for the identification of sand waves. However, the dynamics of the sand waves are in the order of years to decades and therefore a high resolution in time and space is needed to identify the dynamics and track individual sand waves. Because the amplitude of the sand waves on many coasts is often relatively small, they can sometimes be difficult to identify from aerial or satellite images. Systematic measurements of cross-shore profiles or the shoreline position are therefore a useful addition and sometimes the only way to clearly identify shoreline sand waves. This brings us to point (ii) because these detailed and systematic measurements are rare. Point (iii) refers to one of the underlying assumptions of this study: sand waves occur on a length scale larger than that of surfzone rhythmic features and surfzone dynamics are therefore not important for their dynamics. The separation between both processes will in some cases not be that clear.

In this chapter we qualitatively compare our model results with observations. We will first give an overview of observations of shoreline sand waves from existing literature. Then we will present observations of shoreline sand waves on the southwest coast of Africa (based on satellite images). The later observations are compared to model predictions, using the characteristic conditions of that coast. The chapter is concluded with a discussion and some suggestions are made for future observations.

7.2 Observations from existing literature

The most convincing connection between shoreline instability and high angle waves comes from elongated water bodies like lagoons, narrow gulfs and lakes (Zenkovitch, 1959; Ashton & Murray, 2006*b*; Ashton *et al.*, 2009). Due to the geometry of these water bodies there is one dominant fetch orientation, which leads to a wave climate with high wave incidence angles relative to the shore and a limited fetch length leads to relatively short wave periods. Zenkovitch (1959) suggested the connection between the formation of the commonly present cuspate spits and the instability of the shoreline under high angle wave incidence and described their formation in a conceptual way with the use of aerial images. Examples are the cuspate spits in the Azov Sea in the south of Ukraine and the lagoons on the coast of the Chukotsky peninsula in the east of Russia (figure 7.2 and 7.1, respectively). Cuspate or flying spits have also been described on the open ocean coast of Namibia (Elfrink *et al.*, 2003), which has an energetic wave climate with a very oblique wave incidence (see section 7.3).

Shoreline sand waves are less striking features but they have been documented on various coasts. Table 7.1 gives an overview of various studies and the observed characteristics of the sand wave fields. Care must be taken with the interpretation of the wavelengths reported by the various studies because it is not always clear how this length was defined. Ideally the wavelength is defined as in figure 3.3 but at some sites the wavelength is determined visually from images and only a crest can be distinguished clearly. This might lead to an underestimation of the wavelength (e.g. Davidson-Arnott & van Heyningen, 2003; Thevenot & Kraus, 1995).

Stewart & Davidson-Arnott (1988); Davidson-Arnott & van Heyningen (2003) described the formation and migration of sand waves along two sections of Long Point, a large spit on the shore of Lake Erie, USA (figure 7.3). The wave climate is characterized by $H_s = 1-2$ m, $T_p = 4-6$ s and a dominant southwest direction, which leads to a rather oblique incidence with respect to the coast. Figure 7.4 shows an example of one of the sand waves on the distal end of this coast. Oblique aerial photographs and topographic surveys were used to track the shoreline sand waves. They had length scales in the range of $0.35-1.6$ km, amplitudes between 50 and 100 m and they migrated downdrift at about $150-300$ m/yr. The length scale was defined by the distance between the beginning of the crest (the point at which the beach width ceased to decrease in the updrift direction) and the downdrift end of the crest (the point at which beach width ceased to decrease in the downdrift direction). Their planform shape was in general asymmetric with a relatively steep downdrift slope. Specially on the distal end of the spit, they could be followed for periods up to 10 years or more. The sand waves formed at the updrift end of the sand wave fields, triggered by the welding of the inner bar to the beach and they tended to grow in length and amplitude while they migrated downdrift. The welding of the inner bar seemed to be related to local sediment abundance and onshore migration during periods with calm conditions. Even though the welding of bars played an important role in the formation and migration of the sand waves, the length and time scale of the sand waves was larger than that of the nearshore bar dynamics. Furthermore, gradual migration also took place without the welding of bars. Therefore, another mechanism

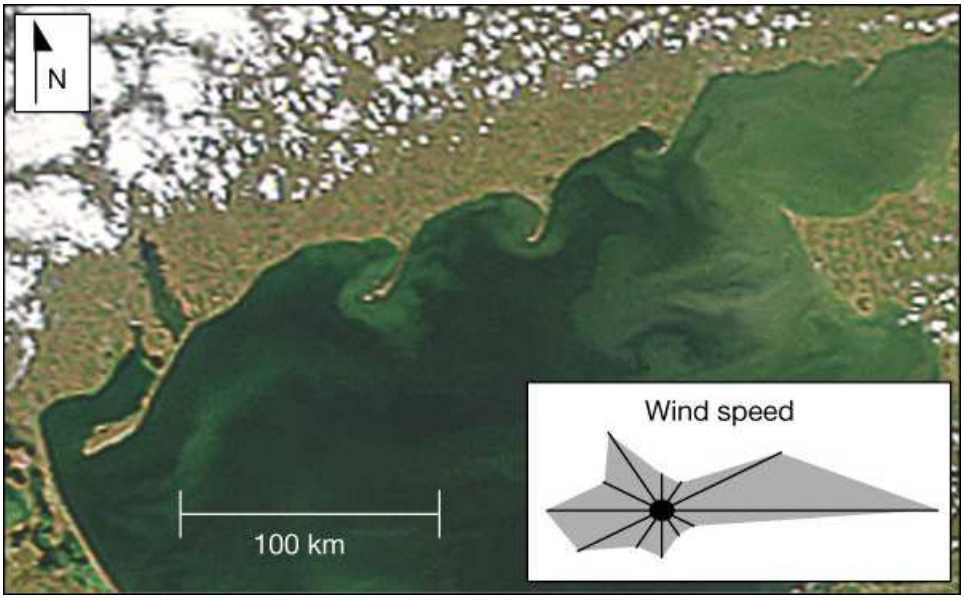

Figure 7.1: Large scale cuspate spits in the Azov Sea in the south of Ukraine (Ashton *et al.*, 2001).

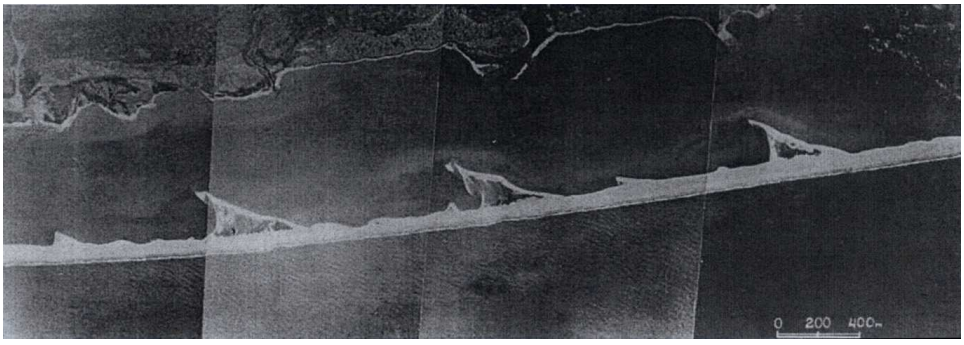

Figure 7.2: Cuspate spits in a lagoon on the north coast of the Chukotsky peninsula, Russia (Zenkovitch, 1959).

must be important for the sand wave dynamics and it was suggested that HAWI might play a role in the growth and downdrift migration (Davidson-Arnott & van Heyningen, 2003; Ashton & Murray, 2006*b*).

A recent study in the eastern Gulf of Finland, Russia, showed the dynamics of shoreline sand waves and spits and it was suggested that they could be related to HAWI (Ryabchuk *et al.*, 2011; Leont'ev *et al.*, 2011). The study used field measurements as well as aerial and satellite images. The sand waves formed where the coastline changes orientation, they increased in size in the downdrift direction and finally developed into spits. The wavelength of the sand waves and spits ranged between 0.3 and 1 km, their amplitudes were between 15 and 200 m and they migrated downdrift at a rate of about 100 m/yr. Figure 7.5 shows a satellite image from 2010 and a previous shoreline derived from a satellite image from 2005 and figure 7.6 shows the evolution of the sand waves and spits according to Ryabchuk *et al.* (2011). Field observations confirmed the erosional and accretional patterns along the coastal features, which is required for growth and migration. The wave climate is dominated by high angle low energy waves that arrive from the west and the nearshore zone is very shallow. Relict spits and lagoons were identified and showed that spit formation occurred for at least the last 2500 years (Ryabchuk *et al.*, 2011).

Sand waves have also been identified with the use of aerial photos on ocean coasts. Thevenot & Kraus (1995) studied alongshore sand waves at Southampton Beach on the barrier coast of Long Island, USA. Five sets of aerial photos withing a 16 month period were used to identify 11 sand waves on the 15 km long beach. The sand waves had a length scale between 0.4 and 1.5 km, amplitudes between 20 and 90 m and they migrated at rates between 0.2 and 2.2 km/yr. Their planform shape tended to be asymmetric with a relatively steep downdrift flank. Aerial photos suggested that oblique finger shoals (downdrift direction) are associated with the sand waves. Some of the sand waves grew in length and amplitude but no clear trend was found and in general they merely maintained their dimensions. Thevenot & Kraus (1995) related the formation of the sand waves with the periodic opening of an inlet, which creates an ebb-tidal shoal that welds to the downdrift beach. However, they did not provide an explanation for their downdrift migration and persistence over long periods. The site has a semi-diurnal tide with a range of 0.9 m. The wave climate can be characterized by $H_s = 1$ m, $T_p = 8$ s and the dominant wave direction is towards the west but high angle wave incidence does not seem to be very persistent. Two shore parallel breaker bars are present at 100 and $300 - 400$ m offshore respectively.

On Fire Island, also on the coast of Long Island, Gravens (1999) analyzed the naturally occurring shoreline undulations on the 50 km long beach over a period of 11 years. They used shoreline positions derived from aerial photos and GPS surveys and applied a spectral analysis to quantify the length scale. The sand waves had a wavelength between 1 and 3 km, amplitudes between 10 and 40 m but no clear migration trend was found. Because of the lack of this trend of migration they referred to them as shoreline undulations instead of sand waves. Some of the sand waves disappeared and formed again at a similar position only migrating within a window of $1 - 2$ km. They argued that the shoreline undulations might be related to offshore bathymetric irregularities and that

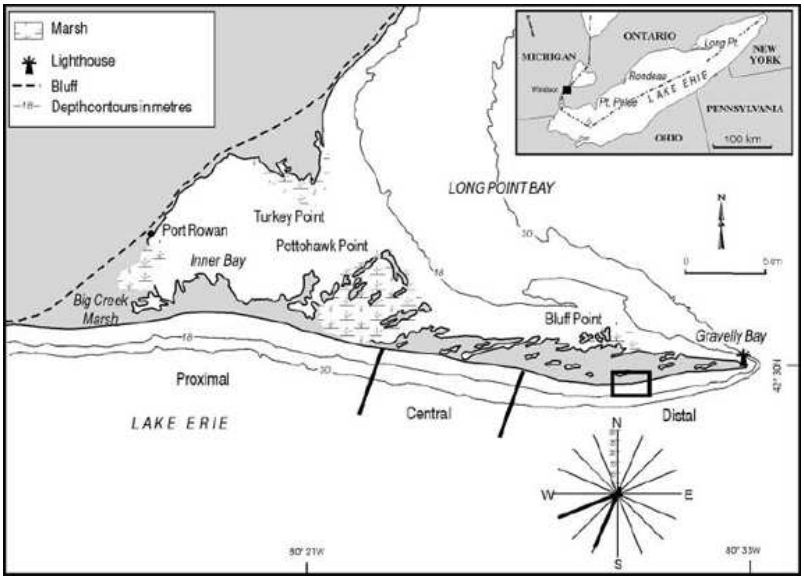

Figure 7.3: The Long Point spit in Lake Erie, USA, indicating the two zones where sand waves occur (proximal and distal) and the wave rose indicates the average wave direction (Davidson-Arnott & van Heyningen, 2003).

Figure 7.4: Satellite image showing a shoreline sand wave on the distal end of the Long Point spit. The black line indicates 500 m (image source: Google Earth).

Figure 7.5: The evolution of alongshore sand waves and spits in the Eastern gulf of Finland. The horizontal line indicates 5 km. The image is from 2010 and the blue line indicates the shoreline position of an image from 2005 (image source: Google Earth).

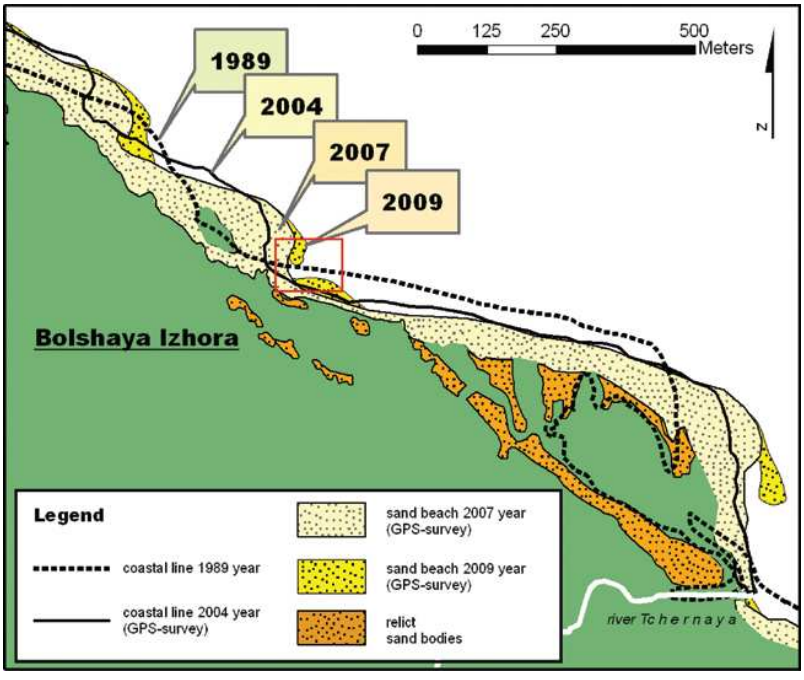

Figure 7.6: The evolution of alongshore sand waves and spits in the Eastern gulf of Finland (Ryabchuk *et al.*, 2011).

they form under specific wave conditions.

On many coasts shoreline sand waves can not be easily observed from aerial photos or satellite images. Even though their amplitude is relatively small, they might still introduce an important variability to the coastline position. Bruun (1954) observed undulations on the west coast of Denmark with wavelengths between 0.3 and 2 km. Some of the undulations only had a crest or through and others both a crest and a through. Periodic measurements of undulations showed amplitudes up to 80 m and migration rates between 0 and 1 km/yr. He suggested that there might be a connection between the undulations and nearshore bar dynamics. In a recent study, Kaergaard *et al.* (2011) analyzed shoreline undulations on two sites along the Danish coast. They used measurements of cross-shore profiles up to 9 m water depth to determine the shoreline position and a possible correlation between the shoreline and the depth contours. The undulations had a wavelength between 5 and 6 km, amplitudes up to 100 m and they migrated at a rate of about 370 m/yr. The undulations were more persistent on the site where the cross-shore extent of the undulations reached up to a greater water depth (5 m) and the wave incidence angle was more oblique ($H_s = 1.3$ m, $T_p = 4.7$ s). They found a good correlation between the shoreline and the 5 m depth contour but the correlation with the nearshore bars was weak. The authors suggested that on this latter site, HAWI could play a role in the dynamics of the undulations.

Verhagen (1989) analyzed the shoreline position on different parts of the coast of The Netherlands. Here we only discuss the results for the central part, the Holland coast. The shoreline position was determined from cross-shore profile data or the position of the high and low water line, which are available since 1855 and have an alongshore spacing of 1 km. Removing the mean trend revealed shoreline sand waves that migrated to the north with a celerity of 65 m/yr and they were better developed in the south and the north of the Holland coast. No physical mechanism was proposed for the occurrence of the sand waves on this part of the coast and they appeared to traverse groin fields unaffected. The amplitude of the sand waves was $40-60$ m and they had a period of $75-100$ yr ($\lambda = 5-6.5$ km). Guillen *et al.* (1999) studied the dunefoot position along the Holland coast. This position was determined with the use of cross-shore profiles which were measured over the period of 1964 to 1992 on intervals of $200-250$ m. The analysis of the dunefoot position on a decadal scale showed undulations with a wavelength of $2-3$ km and a periodicity of $4-15$ yr (migration celerity $150-200$ m/yr). This was more pronounced in the northern part of the Holland coast and in general the migration direction was to the south. The amplitude of the undulations was $10-20$ m and there was a correlation between the dunefoot position and the shoreline position. The amplitude of the undulations in the shoreline were bigger than the related undulations in the dunefoot position. Ruessink & Jeuken (2002) also studied the dynamics of the dunefoot position along the Holland coast. They found wavelengths of $3.5-7$ km, amplitudes of $5-20$ m, a migration celerity of $0-70$ m/yr and most sand waves migrated to the north although migration direction varied along the coast. Most sand waves could be tracked over decades and they also found a correlation with the shoreline position. An explanation for this is that a narrow beach leads to a local dune retreat and a wider beach protects dunes and favors their growth. Guillen *et al.* (1999) suggested that the non-uniform wave energy distribution due to non-uniformity in the nearshore bar system (crescentic shapes and rip channels)

Figure 7.7: Aerial photo of the Southampton beach showing alongshore sand waves and the Mecox inlet in the bottom right (photo credit: Joseph R Melanson of Skypic.com).

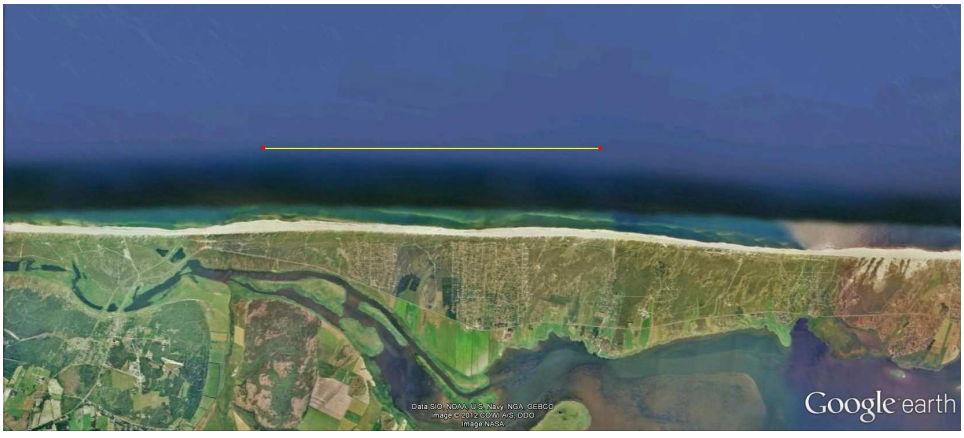

Figure 7.8: Satellite image showing subtle alongshore sand waves along the west coast of Denmark. The Ringkøbing Fjord can be seen in the bottom right corner. The line indicates a distance of 5 km and the north is in the right of the image (source: Google Earth).

may control shoreline evolution and cause the alongshore sand waves. Ruessink & Jeuken (2002) however stated that the time scale of the dynamics of the nearshore bars is shorter than that of the sand waves and that it remains unclear if these dynamics can explain the existence of shoreline sand waves. They suggest that HAWI can also play a role in the formation of sand waves on this coast (see also Ashton *et al.*, 2003; Falqués, 2006).

Most observations of sand waves are in the range of kilometres and smaller scale undulations are generally related to surfzone dynamics. An exception to this are the small scale sand waves ($\lambda \sim 0.1 - 0.2$ km) along El Puntal spit, Santander, Spain (Medellín *et al.*, 2008). Their formation and destruction was monitored with an Argus video system (time scale in the order of weeks). Medellín *et al.* (2009) showed that the sand waves might be related to HAWI and that the small scale could be the result of the very steep cross-shore profile and the very oblique low energy waves that results from refraction and diffraction within the Santander bay.

Other studies that can provide additional insight on the occurrence and behaviour of sand waves are Pringle (1985); Grove *et al.* (1987); Inman *et al.* (1992); Alves (2009). Pringle (1985) described a so called ord along the Holderness coast in England, which can be seen as a single shoreline undulation. They observed a mean alongshore length of 1.2 km, a mean amplitude of 85 m and a migration rate of 500 m/yr. Grove *et al.* (1987) described the dispersion and downdrift migration of a large artificial injection of sediment on the coast at San Onofro in California, USA. The migration celerity of the hump was less than 1 km/yr and the amplitude diminished to half every 300 days. An erosional zone developed downdrift of the hump. Inman *et al.* (1992) described the migration of so called 'sand blankets' along the Nile delta. The sand blankets were about 1.5 m thick, occurred at depths of 4 to 6 m, had an alongshore length of $2 - 4$ km and migrated downdrift at $0.5 - 1$ km/yr. It was argued that they are driven by the divergence of a coastal current and that they generate series of accretion/erosion waves along the shoreline. The sand blankets show similarities to the migrating wave-shaped sand humps described by Bruun (1954) on the Danish coast. These migrating humps occurred at the 9 m depth contour, had a height of $1 - 2$ m and an alongshore length of $2 - 3$ km. Alves (2009) described two very large scale undulations (200 km) of the barrier coast in the south of Brazil, on which shoreline undulations of $10 - 100$ km were superimposed. The shoreline data was obtained from a nautical map, which was based on aerial photos. They linked the shoreline undulations and observations of shoreline erosion to HAWI and explored this hypothesis with the approach of Ashton & Murray (2006*b*).

Satellite images can be used to find more sites where shoreline sand waves are present and information on the dominant wave direction could indicate if their origin might be related to HAWI. Falqués *et al.* (2011a) studied various sand wave fields on the southwest coast of Africa (see section 7.3). Using only one set of satellite images however has the disadvantage that it gives little information on the time evolution of the shoreline and in some cases it will remain uncertain if shoreline undulations are dynamic or if they are related to, for example, the underlying geology. Water level fluctuations due to tide and wave setup can also complicate the correct interpretation of the shoreline position from satellite images.

Table 7.1: Characteristics of observed shoreline sand waves/undulations from various studies. The data used for each study: m = field measurements, a = aerial photos, s = satellite images, v = video images. The final column shows to which mechanism each study attributed the occurrence of the sand waves/undulations.

author	location	λ (km)	A (m)	v (m/yr)	data	related to
Stewart 1988	Lake Erie, USA	$0.7-2^{***}$	$50-95$	$150-300$	m, a	bar welding
Davidson-Arnott 2003	Lake Erie, USA	$0.4-1.6^{***}$	$50-100$	$150-300$	m, a	bar welding, HAWI
Ryabchuk 2011	Gulf of Finland, Russia	$0.3-1$	$15-200$	$20-100$	m, a, s	HAWI
Thevenot 1995	Southampton Beach, USA	$0.8-3^{***}$	$20-90$	$200-2200$	a	periodic inlet opening
Gravens 1999	Fire Island, USA	$1-3$	$10-40$	0	m	irregularities offshore bathymetry
Bruun 1954	east coast Denmark	$0.3-2$	$60-80$	$0-1000$	m	non-uniformity bar system
Kaergaard 2011	east coast Denmark	$5-6$	100	370	m	non-uniformity bar system, HAWI
Verhagen 1989	The Netherlands**	5.5	$40-60$	65	m	-
Guillen 1999 *	The Netherlands**	$2-3$	15	$150-200$	m	non-uniformity bar system
Ruessink 2002 *	The Netherlands**	$3.5-10$	$10-60$	$70-200$	m	HAWI?
Medellin 2008	Santander, Spain	$0.12-0.15$	15	0	v	HAWI
Falques 2011b	Namibia & Angola	$2-8$	$60-175$	$-$	s	HAWI

* Based on the position of the dunefoot.
** Only the data of the Holland coast is included.
*** The wavelength might be underestimated due to visual interpretation.

7.3 Southwest coast of Africa*

7.3.1 Introduction

The southwest coastline of Africa, in Namibia and Angola, features long uninterrupted sandy beaches and it is exposed to an energetic and very persistent oblique wave incidence from the SSW (Elfrink *et al.*, 2003; van Eeden *et al.*, 2008). An exploration of satellite images reveals that shoreline sand waves are very common along this coast. They have wavelengths between $2 - 8$ km and amplitudes up to a few hundreds of meters. In this section various sand wave fields are analyzed from satellite images and in order to find out whether the coast is prone to the formation of sand waves due to HAWI, the Q2D-morfo model is applied with the characteristic morphological and wave conditions of this coast.

7.3.2 Wave climate

The southwestern coast of Africa is dominated by southerly swells generated by storms in the Southern Atlantic Ocean. Offshore wave data of the coast of Namibia were obtained from various sources (Elfrink *et al.*, 2003; van Eeden *et al.*, 2008; Bosman & Joubert, 2008). All studies used a global wave hindcast model to compute the mean offshore significant wave height, H_s, the peak wave period, T_p, and the wave direction. The mean H_s was about 2 m and the wave direction SSW (figure 7.9). There is however an inconsistency in the values of T_p because van Eeden *et al.* (2008); Bosman & Joubert (2008) claim very large peak periods between 10 and 14 s whereas Elfrink *et al.* (2003) describe periods between 6 and 8 s. Because the latter study also gives the water depth of these offshore wave data (132 m), this range for T_p is chosen for the present study.

7.3.3 Studied sand wave fields

The studied area is the sandy southwestern coast of Africa (figure 7.10). The coast of Namibia is covered by the active dunes of the Namib Sand Sea in the south and the Cunene Sand Sea in the north, both part of the Namib Desert. The Curosa-Bahia dos Tigres sand field is located in the south of Angola and, further north, there are some long stretches of sandy coasts downdrift of river deltas. While on other coasts around the world shoreline undulations can only be observed after analysis of detailed measurements of the shoreline position (Verhagen, 1989; Ruessink & Jeuken, 2002), the undulations on this African coast can be clearly observed from a quick survey of satellite images. Most striking are the large spits of Walvis Bay and Sandwich Bay and a large scale shoreline sand wave located in the north of the coast of the Namib Sand Sea (figure

*This section is largely based on Falqués *et al.* (2011a): Falqués, A., van den Berg, N. & Ribas, F. 2011a. Modelling shoreline sand waves. Application to the coast of Namibia. Proceedings of the 7th IAHR Symposium on River, Coastal and Estuarine Morphodynamics: RCEM 2011.

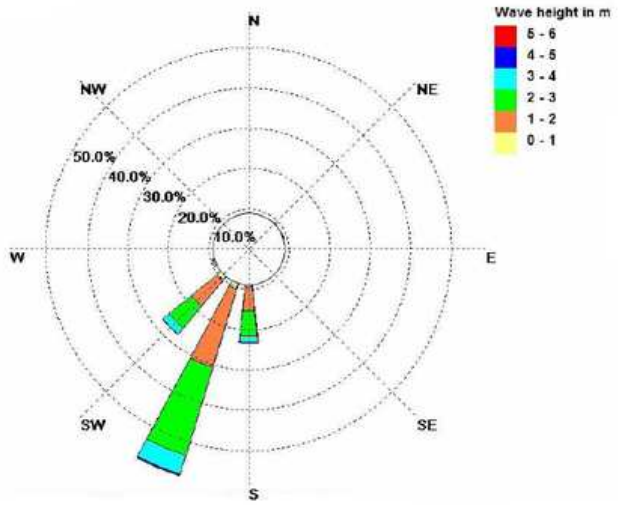

Figure 7.9: Mean annual wave height rose 70 km offshore of the Namib coast (Bosman & Joubert, 2008)

7.10C). Wilkinson *et al.* (1989) described the evolution of Sandwich Bay over a period of 30 years with the use of aerial photos from space shuttles. The spits resemble the flying spits described by Ashton *et al.* (2001), who related their formation to the high angle wave instability acting over very long time periods. This is consistent with the highly oblique wave climate on this African coast. The study of Elfrink *et al.* (2003) on the evolution of the Walvis Bay spit confirmed that high angle wave instability might play an important role on its evolution.

Five different sand wave fields (hereinafter referred to as SWF) with shoreline undulations at length scales of a few kilometres have been selected for this study. The most southern one is the Namib SWF (figure 7.10E), which can be observed after zooming in to the Namib Sand Sea south of the Sandwich Bay spit. It is about 30 km long and the orientation of the coast is roughly North-South (180°). The second and third areas are located in the north of Namibia and the south of Angola. Given that the coastline changes orientation at S 17° 35′6 latitude, the zone was divided in two (Cunene SWF and Dos Tigres SWF, figure 7.10B). The Cunene SWF is 60 km long and is orientated 169°. Dos Tigres SWF is 150 km long, has an 183° orientation and ends at the Bahia dos Tigres flying spit. The fourth sand wave field (Corporolo SWF) is located further north in Angola and is not related to a coastal desert but to the Corporolo river delta (figure 7.10A). This delta provides a source of sand and the sand waves developed downdrift, where the coastline changes orientation from 148° to 223°. This stretch of coast is 20 km long. The last sand wave field (Cuanza SWF) is located on a 20 km long spit downdrift of Cuanza river delta (figure 7.10D). Just as for the previous sand wave field, the coastline changes orientation at the beginning of the spit from 160° to 228°.

Because the Cuanza SWF is located on a spit it seems unlikely that there is some

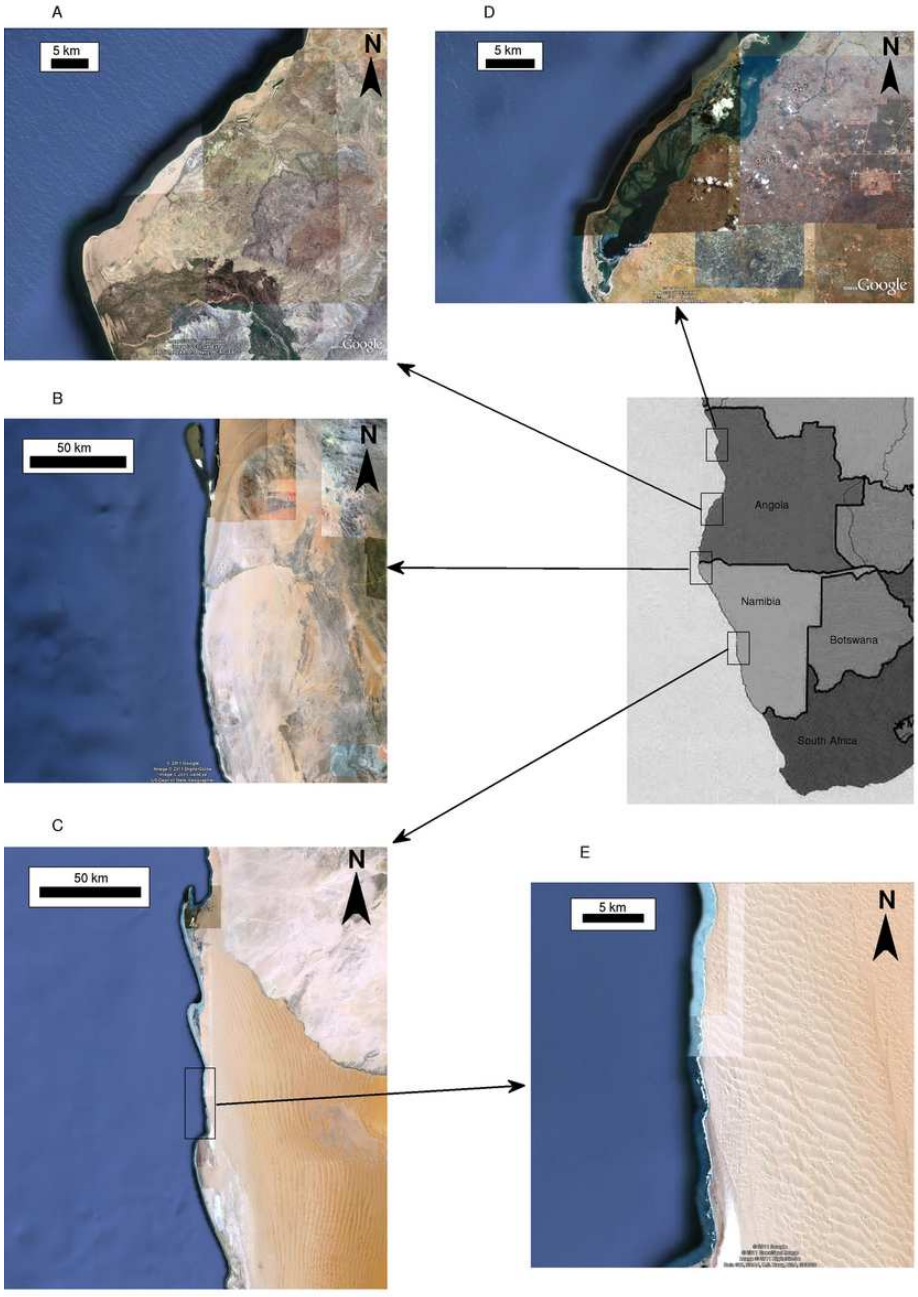

Figure 7.10: The southwestern coast of Africa, indicating the studied sand wave fields (SWF): (a) Corporolo SWF, (b) Cunene SWF and Dos Tigres SWF, (c) Large spits on Namib Sand Sea coast, (d) Cuanza SWF, and (e) Namib SWF (image source: Google Earth).

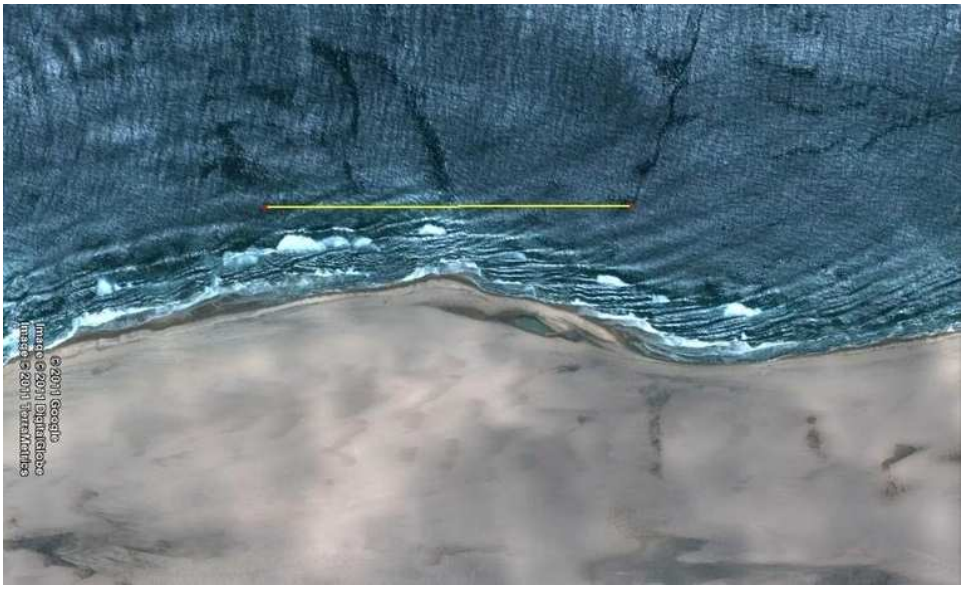

Figure 7.11: Example of accretional/erosional morphology on Cunene SWF. The horizontal line indicates a length of 1 km (image source: Google Earth)

geological forcing on the shoreline undulations. Satellite images show some rock outcrops between the sand dunes for the Cunene SWF and Dos Tigres SWF, so that the underlying geology might play a role in the shape of those coastlines. Most of the undulations, however, show an accretional wide beach at the crest and an erosional narrow beach at the downdrift though (figure 7.11). This suggests that these shoreline undulations are mainly shaped by the interaction between a sandy coastline and hydrodynamics. The same can be concluded for the Corporolo and Namib SWF because historical shorelines, that reflect their evolution, are visible on the beach. Unfortunately no bathymetric information is available for these sand wave fields. The only estimation of a cross-shore profile can be obtained from the bathymetry of the Walvis Bay spit presented in Elfrink *et al.* (2003). A steep beach slope of 0.08 and a distance of 438 m from the shoreline to the 20 m depth contour were estimated.

7.3.4 Wavelength and amplitude of the sand wave fields

The shoreline position of the sand wave fields was digitized from satellite images with the use of Google Earth. Most of the coastline is covered by 2.5 m resolution Quickbird2 multispectral images. For the present purpose this resolution is sufficient and errors introduced by varying tidal levels and wave run-up are not important because we are looking at relatively large scale undulations and we do not look at the time evolution of the shoreline. The shoreline was sampled with an interval of about 100 m. The resulting shoreline was exported and the geographic coordinates were converted to Cartesian

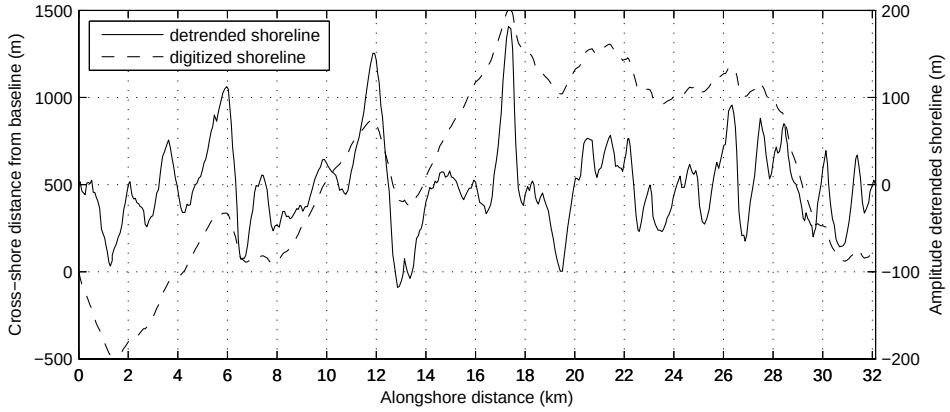

Figure 7.12: Digitized and detrended shoreline of the Namib SWF.

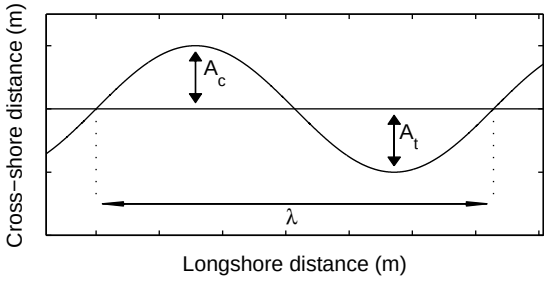

Figure 7.13: Definition sketch of a shoreline sand wave, where A_c is the amplitude of the crest, A_t is the amplitude of the through and λ is the wavelength.

coordinates. Subsequently the shoreline data was detrended by subtracting a smoothed shoreline which was obtained using an alongshore running average within a window of about 2 km (figure 7.12). This also filtered out some of the small scale variations related to surfzone dynamics and variations that were introduced by the digitization. In order to quantify the length scale and amplitudes of the sand waves we used the definitions of figure 7.13. The mean amplitudes (average over all the crest and trough amplitudes) of the shoreline sand waves were estimated from the detrended shorelines (table 7.2). The mean amplitude varied between 59 and 175 m and the largest one (298 m) was found on the Coporolo SWF. The dominant wavelengths were determined with a Fourier analysis of the shoreline position, which gives the spectral density (m^2/m) as a function of the wavelength. The wavelength spectrum for the Namib SWF is presented in figure 7.14. It can be seen that undulations with various wavelengths coexist but that the dominant wavelength is about 5.8 km. The secondary peaks are located at 2 and 2.8 km. The dominant wavelengths of the other sand wave fields can be found in table 7.2 and range between 1.5 and 7.5 km.

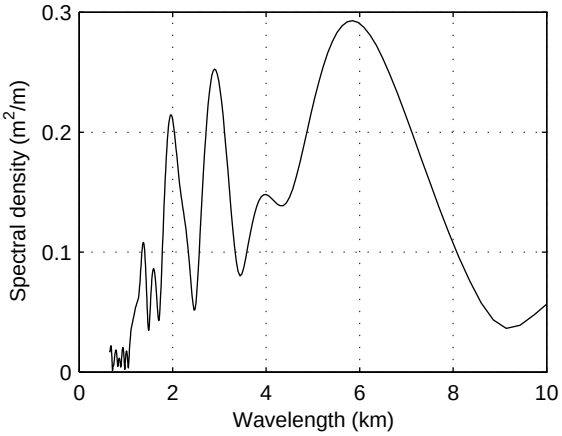

Figure 7.14: Fourier analysis of the detrended shoreline of the Namib SWF. The spectral density is plotted as a function of the wavelength.

Table 7.2: Amplitude and dominant wavelength for each sand wave field.

SWF	A_{mean} (m)	A_{max} (m)	λ 1^{st} peak (km)	λ 2^{nd} peak (km)	λ 3^{rd} (km)
Namib	92	180	5.8	2.8	2
Cunene	78	159	4.4	$1.5 - 2.7$	5.7
Dos Tigres	62	200	3.4	7.5	$4 - 5$
Corporolo	175	298	1.5	3	–
Cuanza	59	99	1.9	2.9	–

7.3.5 Model simulations

A 30 km long rectilinear coastline with an alongshore uniform cross-shore Dean-type profile is used for the simulations. The shape of the profile is controlled by prescribing the swash slope β_s and the water depth D_{ref} at the offshore distance $x_{ref} = 438$ m. On top of this morphology we add a localized Gaussian-shaped bathymetric perturbation, similar to the generic simulations in chapter 4. A localized perturbation is used instead of random perturbations because instability develops faster from a localized perturbation and this makes the exploration of different conditions easier. The size of the simulation domain is $L_x = 1000$ m, including 400 m of dry beach and 600 m of submerged beach, and $L_y = 30000$ m. The grid size is given by $x = 5$ m and $y = 50$ m, and the time step is $t = 0.001$ days. The wave field is updated once a day. The Gaussian shaped perturbation causes an initial undulation on the shoreline position of 2 km alongshore width and two different amplitudes are used, 13 m and 27 m. The corresponding bathymetric perturbation extends offshore up to 7 and 18 m water depth respectively. Other model parameters are set to their default values see table 3.1. Several experiments have been performed to cope with the uncertainty and variability in the bathymetric and wave conditions along the SW African coast (table 7.3). We consider two bathymetric profiles, a steep one and a milder one. According to section 7.3.2 we apply a significant wave

Table 7.3: Parameter setup for the numerical experiments and resulting tendency to stability/instability.

nr	β_s	D_{ref} (m)	$\bar{A}$ (m)	θ_0 (◦)	H_{rms} (m)	T_p (s)	D_p (m)	θ_p (◦)	tendency
1	0.08	20	13	58	1.17	8	9.5	39.2	Stability
2	0.08	20	27	58	1.17	8	18	51.7	Stability
3	0.06	15	13	58	1.17	8	7	37.1	Weak instability
4	0.08	20	13	61	1.10	8	9.5	40.7	Stability
5	0.06	15	27	61	1.10	7	13.5	54.6	Instability
6	0.06	15	13	61	1.10	7	12.5	52.8	Instability

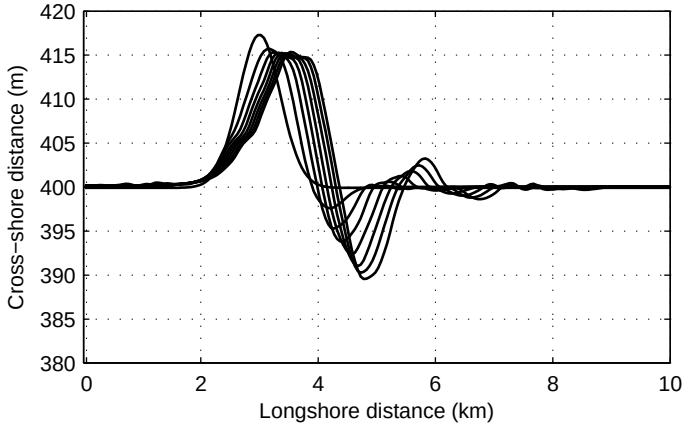

Figure 7.15: Initial evolution of the shoreline for experiment 6, from an initial Gaussian shaped perturbation at $y = 3$ km. The shoreline is plotted every 50 days and the final shoreline corresponds with the result after 1 year. The wave incidence is from the left. Notice that the cross-shore distance is exaggerated by a factor 150.

height $H_s = 2$ m and wave periods $T_p = 7 - 8$ s at a water depth of 132 m. Since the dominant wave direction in deep water is SSW and the coastline trend is approximately S-N, we consider deep water wave angles in the range $65° - 70°$. The offshore waves are refracted to the offshore boundary of the model by assuming rectilinear and parallel depth contours. This results in wave angles between $58° - 61°$ at the offshore boundary. The rest of the parameter setup can be found in table 7.3, where we also include the water depth at the offshore reach of the initial perturbation, D_p, and the wave angle at this depth for each experiment.

The shoreline evolution of the experiments can be characterized by the evolution of the initial perturbation (figure 7.15) and, in case of instability, the development of a spatial-temporal instability which triggered the growth of a downdrift sand wave train (figures 7.16 and 7.17). The evolution of the perturbation can be summarized by: the initial diffusion of the perturbation (mainly in the cross-shore direction), downdrift migration of the crest, development of asymmetry, development of a downdrift erosional

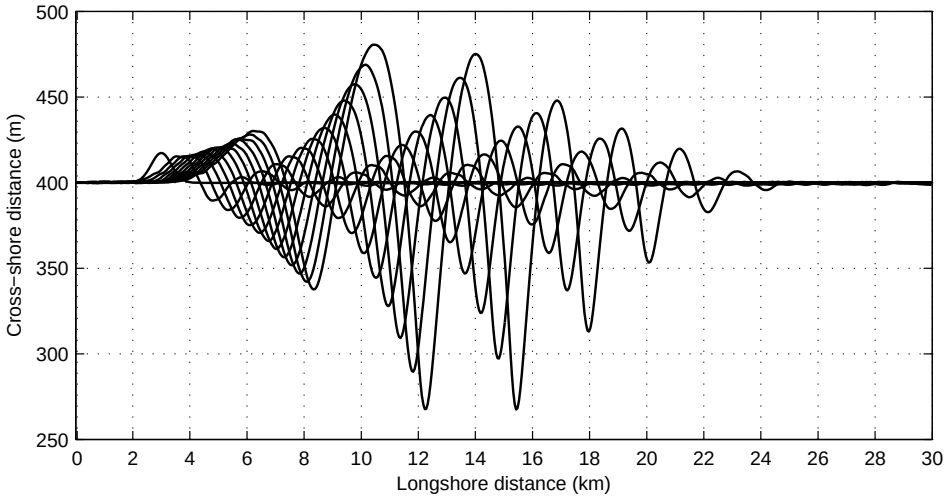

Figure 7.16: Formation of the sand wave train for experiment 6, from an initial Gaussian shaped perturbation at $y = 3$ km. The shoreline is plotted every year and the final shoreline corresponds with the result after 11 year. The wave incidence is from the left. Notice that the cross-shore distance is exaggerated by a factor 60.

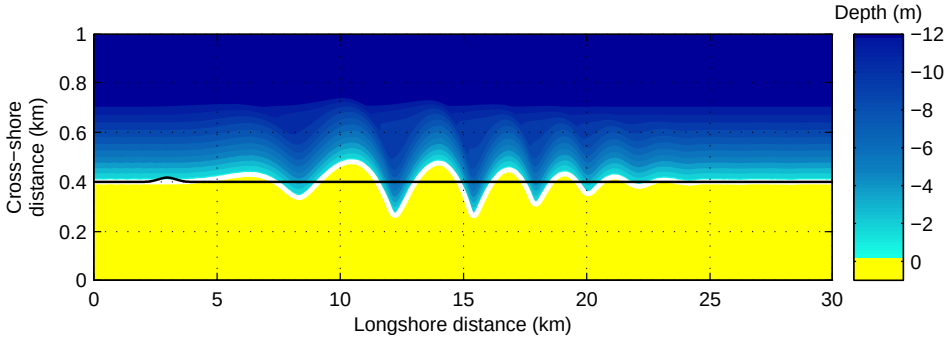

Figure 7.17: Bathymetry of the sand wave train for experiment 6 after 11 years. The black line indicates the initial shoreline. The wave incidence is from the left. There is a factor 10 exaggeration in the cross-shore direction.

zone, and subsequently growth (experiments 3, 5 and 6) or decay (experiments 1, 2 and 4). The results of the six experiments show that only some combinations of bathymetric profiles and wave conditions led to instability (last column of table 7.3). A steep profile seems to limit the development of instability. Even in case of a large amplitude perturbation, for which D_p and θ_p were relatively big (experiment 2), the initial perturbation diffused and even though the downdrift erosional zone grow up to several meters, no sand wave train developed. A milder cross-shore profile (experiment 3) led to a weak instability and the initial perturbation eventually grew slowly and a subtle sand wave train developed. Increasing the wave angle and lowering the wave period led to a stronger instability (experiment 5 and 6) and a clear downdrift sand wave train developed. The characteristic wavelength of the instability is that of the sand wave train, since the length scale associated to the first crest and trough is influenced by the dimensions of the initial perturbation. That wavelength was roughly 2 km for both experiments 5 and 6. This wavelength roughly coincides with the length scale of the initial perturbation but for wider initial perturbation the sand wave train develops at the same characteristic wavelength. The shape of the initial perturbation does not affect the wavelength of the downdrift sand wave train, which is fully self-organized (see section 4.5).

The time scale of development of the instability is relatively short, in one year the wave train is already visible with a crest and a small trough. Within 11 yr the maximum amplitude of the sand waves reached 121 m and the wavelength of the first free sand wave increased from 2 km until 3.8 km. At the same time, the sand waves migrated downdrift with a celerity of $0.6 - 0.7$ km/yr. Even in case of a stable coast, the coastline diffusivity is relatively low, so that shoreline features created by other processes could persist and propagate downdrift for a long time. Thus, no matter if they grow or decay, all shoreline features at these scales migrate downdrift under an oblique wave incidence. This is visible, e.g., in experiment 4 (figure 7.18), where the sand wave resulting from the initial perturbation decays but propagates at a celerity of about 0.45 km/yr.

7.3.6 Discussion and conclusions

A large part of the southwest coast of Africa in Namibia and Angola is composed of long sandy beaches and very striking is the presence of a system of 3 large scale spits (60 km spacing). Apart from the spits, many stretches of coast feature regular shoreline undulations or shoreline sand waves. A Fourier analysis of the shoreline position of some sand wave fields show that several length scales coexist within the range of 1.5 and 7.5 km. Since the wave climate is dominated by incidence angles from SSW (very oblique to the coast which roughly trends S-N) it is plausible that those shoreline features are driven (or at least influenced) by shoreline instability. This hypothesis is supported by the fact that the wavelengths overlaps with the range of $3 - 15$ km, predicted with linear instability analysis for general conditions by Falqués & Calvete (2005). The study was based on only one set of satellite images and the evolution of the sand waves was therefore not observed. Satellite images however suggest that the shoreline undulations are dynamic, showing erosion at the bay and deposition at the crest and a tendency to growth in downdrift direction. However rock outcrops can also be seen on the images

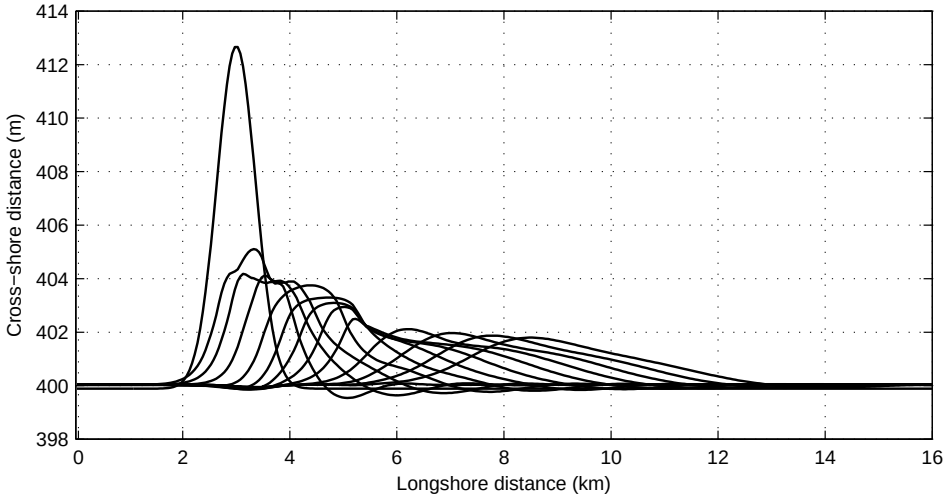

Figure 7.18: Evolution of the shoreline for experiment 4, from an initial Gaussian perturbation at $y = 3$ km. The shoreline is plotted every year and the final shoreline corresponds with the result after 11 years. The wave incidence is from the left. Notice that the cross-shore distance is exaggerated by a factor 500.

and we can not rule out that the underlying geology may play a role in the presence of these shoreline undulations. The large scale spits, might have formed over a very long period from the smaller scale sand waves, a process that was described by Ashton *et al.* (2001).

Preliminary computations with the Q2D-morfo model suggest that this coast indeed has potential for shoreline instability. The factors that favor instability are the high wave angles relative to the coast in deep water and the energetic wave climate (annual mean H_s about 2 m). A factor that reduces the potential for instability are large wave periods, since wave refraction severely reduces the angle of these long waves until they reach the morphodynamic active part of the beach profile. Unfortunately, there is no consensus on the wave period in the consulted literature. Elfrink *et al.* (2003) points out to dominant periods of $T_p = 6 - 8$ s while van Eeden *et al.* (2008); Bosman & Joubert (2008) indicate wave periods mainly in the range $T_p = 10 - 14$ s. Here, we tested the cases $T_p = 7$ s and 8 s which seem realistic on that coast. For $T_p = 7$ s the model clearly predicted coastline instability and the formation of free sand waves with a wavelength of about 2 km. They migrated at a rate of $0.6 - 0.7$ km/yr and within about 10 yr their wavelength slowly increased up to 3.8 km and the amplitude reached up to 100 m. This wavelength is in good agreement with the lower part of the range of wavelengths obtained with the Fourier analysis of the various sand wave fields on the southwest coast of Africa. The variance in the wavelength of the sand wave fields could be related to i) alongshore variability in the bathymetry as a milder profile slope leads to longer wavelengths, ii) differences in the wave conditions along the coast or iii) transition to larger wavelengths due to long term growth and nonlinear interactions. The time scales of the model results seem to

be realistic compared to the observations of shoreline variability by Elfrink *et al.* (2003). For simulations with $T_p = 8$ s, the system seemed to be at the threshold for instability: growth or decay of sand waves occurred, depending on the bathymetry and the initial perturbation. The coastline diffusivity was however relatively low and coastline features formed by other mechanisms could persist and propagate downdrift for a long time under these conditions.

An important limitation of the present study is the lack of detailed knowledge of the bathymetry of the various sand wave fields. From a bathymetric map we inferred the slope at the shoreline and the position of the 20 m bathymetric contour at only one location. From this we adjusted a Dean-type profile and we assumed that this characteristic profile could be used along the whole coast. Simulations suggest that a very steep profile limited the potential for shoreline instability (experiments 1,2 and 4). In section 3.5 it was discussed that the wave angle at the depth of closure is crucial for HAWI and in the generic simulations the critical angle was $\theta_{Dc} \approx 45°$. The depth of closure was defined as the depth where the cross-shore diffusivity is a factor 10^4 smaller than the value close to the shoreline. According to this theory, the wave angle at D_c in the various experiments of this chapter, could explain why in some experiments the shoreline remains stable and in others a sand wave train developed. D_c however did not vary much between the steep and mild profile and was about 7 m. For a mild profile in combination with a higher wave incidence angle and a smaller wave period, D_c was about 6 m (experiments 5 and 6) but θ_{Dc} was merely a few degrees larger than for the stable experiments. Curiously the angles at D_c were between 34° (stable) and 37° (unstable), e.g. about 10° lower than the critical angle found in section 3.5. This suggests that HAWI can develop for relatively low values of θ_{Dc} and that the slope and the shape of the cross-shore profile also plays an important role in the development of HAWI. A future generic study on HAWI should therefore explore the role of the cross-shore profile.

Future work on the southwest coast of Africa should focus on obtaining more detailed bathymetric data and more reliable wave climate data. In particular, the discrepancy in the reported wave periods must be solved. Model computations should be done with a more accurate bathymetry of the sand wave fields, using i) time series from wave records or ii) synthetic time series of wave forcing based on the statistics given by the wave roses. This could provide an indication on why on certain stretches there are sand waves while on others stretches they are not found, and on why different wavelengths and amplitudes are observed at different locations. Furthermore, it would be interesting to obtain satellite images at different moments in time so it can be confirmed that the sand waves are dynamic with a tendency to growth and migration in downdrift direction.

7.4 Discussion

The observations discussed in this chapter show great similarity to the generic model results and they suggest that HAWI can indeed be the main mechanism behind sand wave formation on many sites. Large scale shoreline sand waves are in general found on coasts with an oblique wave incidence and they are more pronounced if the fraction

of high angle waves is very high. The typical wavelengths are in the same range as the model predictions, migration rates and the time scale are similar and the characteristic asymmetrical shape with erosion at the updrift flank and deposition at the crest could be recognized in many observations. However, some uncertainties remain on the role of HAWI in the generation and dynamics of the observed sand waves.

The main uncertainty arises from the fact that there are no direct observations of the physical processes behind the HAWI mechanism. The Q2D-morfo model uses a parametric approach, based on the assumption that the long term evolution of the shoreline sand waves is driven by the net effect of gradients in alongshore transport. However, direct measurements of alongshore transport volumes are very difficult. Even if it would be possible to measure the transport at one position, it varies in time and in cross-shore and alongshore direction due to variations in the various contributing factors, e.g. wave conditions, currents, profile, bedforms, sediment (Cooper & Pilkey, 2004). It would therefore be impossible to measure the net gradients in the alongshore transport over long periods. Further investigation on HAWI should focus on more complete observations of the morphology of shoreline sand waves, their evolution and the conditions under which this takes place. This can be used to validate model predictions and to rule out other processes. The model predictions could be improved by using the actual bathymetry of a sand wave field, a more realistic wave module and by computing the sediment transport directly from the currents. This modelling approach would not be suited for very long term simulations but the short term tendencies could be used to validate the HAWI theory.

Some of the observed wavelengths are at the lower end of the range predicted by the model and in two studies the authors suggested that the occurrence of undulations in the shoreline was related to the nearshore bar system (Bruun, 1954; Guillen *et al.*, 1999). Both studies were published before the work of Ashton *et al.* (2001) on HAWI and subsequent studies on the same coasts did suggest that HAWI could play a role in sand wave formation on these coasts (Kaergaard *et al.*, 2011; Ruessink & Jeuken, 2002). Bruun (1954) pointed out that there seemed to be a relation between breaches in the alongshore bar and shoreline undulations on the Danish coast. Satellite images of the Danish coast confirm that there are many relatively short scale undulations on this coast and that rhythmicity in the nearshore bar system plays a role. Figure 7.4 shows an example of some very clear shoreline undulations on the Danish coast, south of the Nissum Fjord. The undulations are asymmetric and their length scale increases in downdrift direction from 0.35 to 1 km. A crescentic bar system can be recognized and seems to be related to the shoreline undulations. van Enckevort *et al.* (2004) presented a review of observations of crescentic bars and wrote that their length scale can range between 150-3000 m. On some sites the crescentic bars even migrated in the direction of the mean alongshore current and they were present over periods of days up to several months. Kaergaard *et al.* (2011) however showed that, on another section of the Danish coast, some larger scale undulations seemed to be related to HAWI and not to the nearshore bar system. This illustrates that, both HAWI and the dynamics of the bar system might cause shoreline undulations on the same coast, depending on local conditions. At intermediate length scales, it is possible that there is a confluence of both processes and it might not be clear if the shoreline follows the curvature of the nearshore bar or the other way around.

On the Dutch coast, Guillen *et al.* (1999) also argued that the shoreline undulations might be related to the non-uniformity in the nearshore bar system (crescentic shapes and rip channels). On this coast the length scales are however relatively big and this non-uniformity in the bar system does not explain the observed persistence of the undulations over many years. Ruessink & Jeuken (2002) argued that the time scale of the dynamics of the nearshore bars is shorter than that of the shoreline undulations on the Dutch coast. However, even if the latter is true, the non-uniformity in the nearshore bar system might still function as an initial perturbation of the shoreline, triggering the growth of shoreline sand waves due to HAWI. The role of the nearshore bars on Southampton Beach is not clear. Thevenot & Kraus (1995) reported that two nearshore bars are present on this coast but did not mention alongshore bar rhythmicity. Figure 7.4 suggests that a crescentic pattern with a large spacing can be present on this coast but the breaking wave pattern and rip currents might also be related to the shoreline sand waves and their associated finger shoals. Stewart & Davidson-Arnott (1988) showed that the cross-shore dynamics of nearshore bars can also be important for sand wave formation and dynamics. The welding of the inner bar triggered the formation of sand waves on the Long Point spit and caused jumps in the migration of the sand waves. This process might also be important on other coasts. Figure 7.4 suggests the welding of an inner bar on the Danish coast in the left of the image.

For some of the studies it remains unclear if the fraction of high angle waves is big enough for spontaneous sand wave formation. In section 5.2 it was argued that a relatively big fraction of high angle waves is required for HAWI and that the range of high angle waves is relatively small. The averaged wave climate at an offshore location only gives an indication of the potential for HAWI on a coast. The wave incidence angles should be determined at the most offshore extent of the sand waves and the fraction of high angle waves at this water depth should be relatively high. The cross-shore extent of sand waves is therefore very important for HAWI and a limited cross-shore extent would rule out HAWI as mechanism for sand wave formation (see section 3.5 and Kaergaard *et al.* (2011)). Most studies however lack information on the submerged bathymetry of the sand waves. Even if the fraction of high angle waves is not very high, HAWI could still play a role in the downdrift migration and the relative low diffusion rate (or slow growth) of sand waves that were initially formed by another mechanism. This could, for example, be the case at Southampton Beach, where initial formation of sand waves is caused by the welding of an ebb-shoal related to the periodic opening (Thevenot & Kraus, 1995).

Future observations of shoreline sand waves should focus on:

1. Long time series of high resolution measurements in time and space of the shoreline position and cross-shore profiles to identify and track individual sand waves. Simulations for the southwest coast of Africa also suggested that the shape and slope of the cross-shore profile is an important factor for HAWI and the profile slope has been shown to be an important parameter for the wavelength selection (see section 6.3.4).

2. Data on the submerged bathymetry of shoreline sand waves. A limited cross-

shore extent of the sand waves would rule out HAWI as mechanism for sand wave formation.

3. Time series of the morphology of the nearshore bar system (if present). In order to rule out surfzone dynamics as a direct cause for sand wave formation and dynamics, it is required to demonstrate a lack of correlation between the non-uniformities of the nearshore bar and the shoreline undulations.

4. Time series of wave conditions.

Figure 7.19: Shoreline undulations related to a crescentic bar on the Danish coast, south of the Nissum Fjord. The north is in the right of the image and the horizontal line indicates 2 km (source: Google Earth).

Figure 7.20: High energy conditions on Southampton beach, Long Island, USA. The horizontal line indicates 2 km (source: Google Earth).

Chapter 8

Conclusions

The objective of this study was to provide more insight into the formation and dynamics of shoreline sand waves and, in particular, to explore the role of high angle wave instability. A non-linear morphodynamical model for large scale shoreline dynamics was used to predict the formation and evolution of shoreline sand waves. The model assumes that large scale and long term shoreline dynamics is controlled by the wave driven alongshore transport and the details of the surfzone morphodynamics are therefore not resolved. It computes the wave field with a simple wave module over the evolving bathymetry and uses the empirical CERC formula to compute the alongshore transport, including a cross-shore distribution. Cross-shore dynamics is described in a parametrized way and the model is capable of describing shoreline perturbations with a finite and dynamic cross-shore extent. The quasi 2D approach was expected to provide more insight into the physical mechanism behind high angle wave instability. The most important conclusions of the study are summarized by answering the research questions that were formulated in the introduction.

1. Does the Q2D-morfo model predict the formation of shoreline sand waves due to high angle wave instability?

   In line with the previous studies on HAWI, the Q2D-morfo model predicts the formation of shoreline sand waves under oblique wave incidence.

2. If so, under what conditions and what are the characteristics of the shoreline sand waves?

   In chapters 3 and 4 the formation of sand waves was studied using initial random small scale perturbations and an initial localized perturbation, respectively. Under constant high angle wave incidence, the random perturbations led to the formation in unison of shoreline sand waves. In the generic simulations, the sand waves developed with wavelengths between 2 and 5 km and the time scale for their formation was in the order of $5-10$ years. Their amplitude increased exponentially and after

13 simulated years the amplitude reached up to 121 m and the sand waves migrated downdrift at a rate of about 0.5 km/yr.

Under the same conditions, the localized perturbation developed into a downdrift migrating shoreline sand wave and it triggered the growth of a downdrift sand wave train through a chain-reaction in the alongshore transport gradients. The formation of the sand wave train can be seen as a spatial-temporal instability. New sand waves were formed downdrift with initial wavelengths of about 2 km. They subsequently grew in amplitude and wavelength and the first sand waves of the train therefore had bigger amplitudes and wavelengths. The default experiment showed the development of 6 sand waves within the 30 km domain during 9 simulated years. The mean amplitude ranged between $60 - 220$ m, the wavelength between $2.3 - 7.5$ km and the sand waves migrated downdrift at $0.3 - 1.1$ km/yr. The initial development of a sand wave field from a large scale perturbation was relatively fast compared to the formation in unison from small scale random perturbations (in the order of $1 - 3$ years).

In the default simulations, instability developed for wave incidence angles above a critical value of about 42° and the growth rate of the shoreline sand waves increased strongly for wave angles above this value. However, it was demonstrated that this critical angle is required at the depth of closure (i.e., the most offshore extent of the shoreline perturbations) and not at deep water (Ashton *et al.*, 2001) or the offshore boundary of the model (Falqués & Calvete, 2005). The refinement of this criterion reduces the potential for the occurrence of high angle wave instability on natural coasts. For wave incidence angles close to the critical angle, the initial localized perturbation maintained more or less its volume while it migrated downdrift and the downdrift sand wave train developed very slowly. For wave incidence angles below the critical value the localized perturbation diffused and the adjacent shoreline remained stable. It must be kept in mind that the criterion for instability is not very exact due to uncertainties in the definition and determination of the depth of closure and the critical angle could vary for other alongshore transport formulations or different cross-shore profiles. The growth rate of the shoreline sand waves was higher for a mean wave climate with high waves and short wave periods, with the growth rate being roughly proportional to $H_s^{2.5}/T_p^{-1}$.

3. What role do cross-shore dynamics play in high angle wave instability and the dynamics of shoreline sand waves?

   Cross-shore transport redistributes sediment between the surfzone (where most of the alongshore transport takes place), the shoreline and the shoaling zone and it therefore plays an essential role in the feedback between shoreline perturbations and the wave field. It controls up to what depth a shoreline perturbation extends into the bathymetry and it was demonstrated that shoreline instability only developed if the wave angle at this depth was bigger than a critical value of about 42°. Simulations showed that faster cross-shore dynamics led to higher growth rates. In the simulations with constant wave conditions shoreline undulations eventually always extended up to the depth of closure. This seems reasonable in the context of a large temporal scale but it needs to be validated with observations of sand waves on real coast.

4. What is the effect of variable wave incidence angles on the formation and dynamics of shoreline sand waves?

   A more realistic wave climate, with alternating high and low wave incidence angle (represented by 60° and 30° at the offshore boundary, respectively), reduced the potential for spontaneous sand wave formation from small scale perturbations. For a fraction of high angle waves lower than 80%, no regular sand wave field developed. It was demonstrated that the range of wave angles that lead to stability is larger than the range of wave angles that lead to instability and that the average magnitude of the positive diffusion produced by the stable wave angles is bigger than the average magnitude of the negative diffusion, produced by the unstable wave angles. Small fractions of low angle waves also reduced the growth rate of a localized large scale perturbation. For a fraction of high angle waves around 80%, the perturbation more or less maintained its volume while it migrated downdrift. This confirms that, even if high angle waves are not dominant, HAWI might play a role in the persistence and downdrift migration of large scale shoreline perturbations. For an increasing fraction of low angle waves the perturbation diffused at an increasing rate and the migration rate decreased. The spatial-temporal instability was dampened due to small fractions of low angle waves. For high angle wave fractions lower than 60% there was no effect on the coast adjacent to the initial perturbation. A bimodal wave climate, with fractions of high angle waves coming from opposite directions, reduced the growth and migration rate of the shoreline sand waves that formed from small scale perturbations. When the wave climate was symmetrical, the small scale perturbations developed into a very regular sand wave field and the sand waves did not migrate. The growth rate of a localized large scale perturbation was enhanced by a bimodal wave climate but the development of the spatial-temporal instability was dampened.

5. What is the physical mechanism behind high angle wave instability?

   The gradients in the alongshore transport Q, the wave height and the relative wave angle at breaking along an undulating coastline were analyzed in order to provide more insight into the physical mechanism behind HAWI. The growth or decay of shoreline sand waves and their migration depend on the alongshore distribution of Q, which is a function of the wave height, H_b, and relative wave angle breaking, α_b. For low angle wave incidence the gradients of α_b were dominant and Q_{max} was located on the downdrift flank of the undulation (causing diffusion). However, for increasing wave incidence angles, the relative importance of the gradients in H_b increased, which moved the position of Q_{max} in the updrift direction (causing diffusion and migration). Above the critical wave incidence angle, Q_{max} moved updrift of the crest leading to the growth of the sand waves together with a downdrift migration. In line with previous studies it was found that the essential physical mechanism behind high angle wave instability is wave energy dispersion due to wave refraction, which leads to a maximum in H_b on the updrift flank and a minimum on the downdrift flank. In addition to this mechanism, the curvature of the bathymetric lines leads to wave energy focusing near the crest. This effect competes with the wave energy dispersion and moves the position of Q_{max} closer to the crest, which results into a less unstable transport pattern.

6. Does the Q2D-morfo model predict an optimal wavelength for sand wave formation

and what is the underlying physical mechanism?

Simulations showed that undulations with small length scales diffused even under high angle wave conditions. The existence of a minimum length scale for HAWI can be explained by analyzing the alongshore gradients of H_b and α_b. The maximum of α_b was located near the downdrift inflection point of the undulation for all length scales. However, the position of the maximum of H_b moved significantly depending on the length scale as a result of the competition between wave energy dispersion and wave focusing. For short sand waves, wave focusing was dominant and the maximum of H_b was located slightly downdrift of the crest and, as a result, Q_{max} was located downdrift of the crest (causing diffusion). For longer sand waves, wave energy dispersion became increasingly important and the maximum in H_b moved updrift of the crest. In addition, the relative importance of the gradients in H_b increased for longer sand waves and therefore Q_{max} also moved updrift of the crest, which resulted into sand wave growth.

On the other hand, it was found that the alongshore gradients in Q decrease monotonically for increasing wavelengths. As a result the sand wave growth rate tends to zero for large wavelengths and this explains the occurrence of an optimal wavelength for sand wave growth. For default conditions the minimum wavelength was about 2 km and the optimal wavelength was about 3 km. A linear model was used to confirm the mechanism of wavelength selection and it was shown that the optimal wavelength for sand wave formation is inversely proportional to the mean slope of the active profile. The relation with the wave period was less clear but in general the optimal wavelength increased for higher wave periods.

7. How do the predictions of the Q2D-Morfo model compare to previous modelling studies and to what extent do the simplifications and approximations of the previous studies affect their predictions?

   First, we compare the approach and results of this thesis with the studies of Ashton *et al.* (2001); Ashton & Murray (2006*a*,*b*), which we refer to as the Ashton&Murray approach. The present study reproduces the basic high angle wave mechanism as presented by the Ashton&Murray approach and it confirms that wave energy dispersion is essential for the development of HAWI. However, due to the implicit assumption that shoreline perturbations extend into the bathymetry up to the wave base, the Ashton&Murray approach strongly overestimates the potential for shoreline instability. In this thesis it has been proposed that it is more reasonable to assume that the maximum cross-shore extent is the depth of closure and this depth is much smaller than the depth at the wave base. Because the critical angle for HAWI is now required at the depth of closure, the range of deep water wave angles that leads to instability is much smaller (for default simulations 61° - 90° compared to 42° - 90° for Ashton&Murray). It was also demonstrated that the magnitude of the net positive diffusion produced by the low angle wave range is bigger than the magnitude of the net negative diffusion produced by the high angle wave range. Therefore the dimensionless stability index, that Ashton & Murray (2006*b*) used to measure the balance between positive diffusion and negative diffusion on natural coasts, over predicts the potential for instability. Furthermore, the Ashton&Murray approach does not take into account the curvature of the bathymetric lines and it therefore does not describe wave focusing. The present study shows that wave

focusing at the crest of an undulation competes with wave energy dispersion and that it reduces instability. Wave focusing has also been shown to be essential for the occurrence of a minimal length scale for HAWI and this explains why the Ashton&Murray approach does not predict a minimal length scale.

Second, we compare the approach and results of this thesis to Falqués & Calvete (2005). The present model is an extension of the linear model of the later study. The most obvious improvement is the ability to predict non-linear behaviour and the evolution of large amplitude sand waves instead of only the initial tendency. Both models use a finite cross-shore extent of the perturbation but in Falqués & Calvete (2005) it was fixed while in the present model the extent is dynamic and coupled to the cross-shore transport and wave conditions. Falqués & Calvete (2005) recognized that shoreline instability did not develop for a limited cross-shore extent but they did not relate this to the wave incidence angle at this depth and simply concluded that the 45° criterion for deep water waves was merely a lower bound and that HAWI in general requires higher wave angles at deep water. The model of Falqués & Calvete (2005) uses the same formulations for wave transformation and refraction and the model also includes the effect of the curvature of the bathymetric lines. Both models predict a minimal and optimal wave length for HAWI and the curve of the growth rate versus wavelength was very similar for both studies. However, a relatively large cross-shore extent had to be used in the linear model to obtain a similar range of wavelengths. The 2D approach of the present study gave more insight in the physical mechanisms behind the wavelength selection but the linear model was better suited for the exploration of parametric trends. In both studies it was found that instability was favored by short wave periods. However, in contrast to the present study, Falqués & Calvete (2005) found that instability was favored by low wave heights. This discrepancy comes from the fact that Falqués & Calvete (2005) used a fixed cross-shore extent of the perturbations, which was independent of the wave height.

8. How do the predictions of the Q2D-Morfo model compare to existing observations of shoreline sand waves?

   Observations of sand waves from existing literature and from satellite images of the southwest coast of Africa show great similarity to the generic model results and they suggest that HAWI can indeed be the main mechanism behind sand wave formation on many sites. Large scale shoreline sand waves are in general found on coasts with an oblique wave incidence and they are more pronounced if the fraction of high angle waves is very high. The typical wavelengths are in the same range as the model predictions, the migration rates and the time scale are similar and the characteristic asymmetrical planview shape, with erosion at the updrift flank and deposition at the crest and the downdrift flank, could be recognized in many observations.

   However, some uncertainties remain on the role of HAWI in the formation and dynamics of the observed sand waves. Some of the observed wavelengths are at the lower end of the model predictions and some studies suggested that alongshore irregularities in the nearshore bar system might play a role in the formation of these sand waves. Even though the spatial and time scales of the nearshore bar dynamics is in general shorter than that of the shoreline sand waves, there might

be a confluence of bar dynamics and HAWI at intermediate length scales. In other studies it remained unclear if the fraction of high angle waves is big enough for spontaneous sand wave formation. The average wave climate at an offshore location merely gives an indication of the potential for HAWI on the coast. In order to confirm HAWI as a plausible mechanism for sand wave formation, the wave incidence angles should be determined at the most offshore extent of the sand waves and the fraction of high angle waves at this water depth should be relatively high. A limited cross-shore extent would rule out HAWI as mechanism for sand wave formation. Unfortunately, most studies lack information on the submerged bathymetry of the sand waves.

In line with previous studies, this thesis confirms that high angle wave instability is a plausible mechanism for the formation of shoreline sand waves and even if high angle wave incidence is not dominant on a coast, the mechanism can describe the persistence and migration of shoreline perturbations originating from other processes. The model provides some improvements to previous modelling studies. The conditions under which shoreline instability can lead to the formation of shoreline sand waves were refined and were shown to be more restrictive. More insight into the physical mechanisms behind high angle wave instability and wavelength selection was provided. However, the model has some limitations which should be addressed in future research. Some suggestions for model improvements were given in section 6.5.1 and include: i) solving the limitation on large gradients in the shoreline position, which would allow for the description of sand waves with bigger amplitudes and the exploration of finite amplitude behaviour of the sand waves (saturation of growth), ii) changing the concept of a predefined equilibrium cross-shore profile so that the cross-shore transport would be perpendicular to the bathymetric lines instead of the y-axis, iii) validate the predictions of the wave module with a more realistic wave model, iv) validating the alongshore sediment transport predictions obtained with the CERC formula by computing the alongshore transport directly from the alongshore component of the current field and v) including a more process-based description of the cross-shore transport.

The model predictions are in qualitative agreement with observations but there are no direct observations of the physical processes behind high angle wave instability. This is the consequence of the large spatial and temporal scale involved. Variability of the driving parameters in time and space makes measurements difficult and masks long term trends. Further investigation on high angle wave instability should focus on more complete observations of the morphology of shoreline sand waves, their evolution and the conditions under which this takes place. This can be used to validate model predictions and to rule out other processes. Observations should ideally contain: i) long time series of the shoreline position and cross-shore profiles, ii) time series of wave conditions, iii) data of the submerged bathymetry of shoreline sand waves and iv) time series of the morphology of the nearshore bar system (if present).

Bibliography

Alves, Albano Ribeiro 2009 Long term erosional hot spots in the southern Brazilian coast. *J.Geophys.Res.* **114** (C02020), doi:10.1029/2008JC004933.

Ashton, A. & Murray, A. B. 2006*a* High-angle wave instability and emergent shoreline shapes: 1. modeling of sand waves, flying spits, and capes. *J.Geophys.Res.* **111**, F04011,doi:10.1029/2005JF000422.

Ashton, A. & Murray, A. B. 2006*b* High-angle wave instability and emergent shoreline shapes: 2. wave climate analysis and comparisons to nature. *J.Geophys.Res.* **111**, F04012,doi:10.1029/2005JF000423.

Ashton, A., Murray, A. B. & Arnault, O. 2001 Formation of coastline features by large-scale instabilities induced by high-angle waves. *Nature* **414**, 296–300.

Ashton, A., Murray, A. B. & Ruessink, G. B. 2003 Initial tests of a possible explanation for alongshore sandwaves on the dutch coast. In *Proc. 3rd IAHR symposium on River, Coastal and Estuarine Morphodynamics,* vol. 1 (ed. A. Sánchez-Arcilla & A. Bateman), pp. 320–330. Barcelona, Spain.

Ashton, A. D., Murray, A. B., Littlewood, R., Lewis, D. A. & Hong, P. 2009 Fetch-limited self-organization of elongate water bodies. *Geology* **37**, 187–190.

Bailard, J. A. 1981 An energetics total load sediment transport model for a plane sloping beach. *J. Geophys. Res.* **86** (C11), 10938–10954.

Barbaro, G., Malara, G., Martino, M. C. & Arena, F. 2010 Analytical development of a one-line model for the analysis of shoreline change by wind generated waves. *Open Ocean Eng J* **3**, 108–115.

Battjes, J. A. 1975 Modeling of turbulence in the surfzone. In *Proc. Symp. Model. Tech.*, pp. 1050–1061. Am. Soc. of Civ. Eng., New York.

Bender, C. J. & Dean, R. G. 2004 Potential shoreline changes induced by three-dimentional bathymetric anomalies with gradual transitions in depth. *Coast. Eng.* **51**, 1143–1161.

Benedet, L. & List, J. H. 2008 Evaluation of the physical process controlling beach changes adjacent to nearshore dredge pits. *Coast. Eng.* **55**, 1224–1236.

Booij, N., Ris, R. C. & Holthuijsen, L. H. 1999 A third-generation wave model for coastal regions: 1. Model description and validation. *J. Geophys. Res.* **104** (C4), 7649–7666.

Bosman, D. E. & Joubert, J. R. 2008 *Report on wave, wind and water level conditions at Walvis Bay*. Technical Report Namibian Port Authority.

Bruun, P. 1954 Migrating sand waves or sand humps, with special reference to investigations carried out on the Danish North Sea Coast. In *Coastal Eng. 1954*, pp. 269–295. Am. Soc. of Civ. Eng.

Caballeria, M., Falqués, A. & van den Berg, N. 2011 Potential instabilities of catalan coastline induced by high-angle waves. In *River, Coastal and Estuarine Morphodynamics: RCEM 2011*. Cd-rom.

Capobianco, M., Hanson, H., Larson, M., Steetzel, H., Stive, M.J.F., Chateluse, Y., Aarninkhof, S. & Karambas, T. 2002 Nourishment design and evaluation: applicability of model concepts. *Coastal Eng.* **47**, 113–135.

Coco, G. & Murray, A. Brad 2007 Patterns in the sand: From forcing templates to self-organization. *Geomorphology* **91** (271-290).

Cooper, J.A.G. & Pilkey, O.H. 2004 Longshore drift: Trapped in an expected universe. *J. Sediment. Res.* **74**, 599–606.

Davidson-Arnott, R. G. D. & van Heyningen, A. 2003 Migration and sedimentology of longshore sandwaves, Long Point, Lake Erie, Canada. *Sedimentology* **50**, 1123–1137.

Dean, R. G. 2002 *Beach nourishment. Theory and practice*. Singapore: World Scientific.

van Duin, M. J. P., Wiersma, N. R., Walstra, D. J. R., van Rijn, L. C. & Stive, M. J. F. 2004 Nourishing the shoreface: observations and hindcasting of the Egmond case, The Netherlands. *Coast. Eng.* **51**, 813–837.

van Eeden, F., Smith, G. & van Tonder, A. 2008 *Walvis Bay setback Line*. Technical Report WSP Africa Coastal Engineers.

Elfrink, B., Prestedge, G., Rocha, C. B. M. & Juhl, J. 2003 Shoreline evolution due to highly oblique incident waves at Walvis bay, Namibia. In *Coastal Sediments'03* (ed. R.A. Davis, A.H. Jr. Sallenger & P. Howd). CD-rom.

Falqués, A. 2003 On the diffusivity in coastline dynamics. *Geophys. Res. Lett.* **30** (21), 2119, doi:10.1029/2003GL017760.

Falqués, A. 2006 Wave driven alongshore sediment transport and stability of the Dutch coastline. *Coastal Eng.* **53**, 243–254.

Falqués, A. & Calvete, D. 2005 Large scale dynamics of sandy coastlines. Diffusivity and instability. *J. Geophys. Res.* **110** (C03007), doi:10.1029/2004JC002587.

Falqués, A., Calvete, D. & Ribas, F. 2011 Shoreline instability due to very oblique wave incidence: Some remarks on the physics. *J. Coastal Res.* **27** (2), 291–295.

Falqués, A., Garnier, R., Ojeda, E., Ribas, F. & Guillén, J. 2008 Q2D-morfo: a medium to long term model for beach morphodynamics. In *River, Coastal and Estuarine Morphodynamics: RCEM 2007,* vol. 1 (ed. Dohmen-Jansen & Hulscher), pp. 71–78. London: Taylor and Francis Group.

Falqués, A., van den Berg, N., Ribas, F. & Caballeria, M. 2011a Modelling shoreline sand waves. application to the coast of namibia. In *River, Coastal and Estuarine Morphodynamics: RCEM 2011*. Cd-rom.

Federici, B. & Seminara, G. 2003 On the convective nature of bar instability. *J. Fluid Mech.* **487**, 125–145.

Gravens, M. B. 1999 Periodic shoreline morphology, Fire Island, New York. In *Coastal Sediments'99* (ed. N.C. Kraus & W.G. McDougal), pp. 1613–1626. World Scientific.

Grijm, W. 1960 Theoretical forms of shorelines. In *Coastal Eng. 1960*, pp. 197–202. Am. Soc. of Civ. Eng.

Grove, R. S., Sonu, C. J. & Dykstra, D. H. 1987 Fate of a massive sediment injection on a smooth shoreline at san onofre, california. In *Coastal Sediments 1987*, pp. 531–538. Am. Soc. of Civ. Eng.

Grunnet, N. M. & Ruessink, B. G. 2004 Morphodynamic response of nearshore bars to a shoreface nourishment. *Coastal Eng.* **52**, 119–137.

Guillen, J., Stive, M. J. F. & Capobianco, M. 1999 Shoreline evolution of the Holland Coast on a decadal scale. *Earth Surf. Process. Landforms* **24**, 517–536.

Hallermeier, R. J. 1978 Uses for a calculated limit depth to beach erosion. In *Coastal Eng. 1978*, pp. 1493–1512. Am. Soc. of Civ. Eng.

Hartog, W. M., Benedet, L., Walstra, D. R., van Koningsveld, M., Stive, M. J. F. & Finkl, C. W. 2008 Mechanisms that influence the performance of beach nourishment: A case study in delray beach, florida, u.s.a. *J. Coastal Res.* **24**, 1304–1319.

Hinton, C. & Nicholls, R. J. 1998 Spatial and temporal behaviour of depth of closure. In *Coastal Eng. 1998*, pp. 2913–2925. Am. Soc. of Civ. Eng.

Holthuijsen, L. H. 2007 *Waves in Oceanic and Coastal Waters*. Cambridge, U.K.: Cambridge Univ. Press.

Inman, D. L. 1987 Accretion and erosion waves on beaches. *Shore and Beach* **55** (3/4), 61–66.

Inman, D. L., Elwany, M. H. S., Khafagy, A. A. & Golik, A. 1992 Nile delta profiles and migrating sand blankets. In *Coastal Eng. 1992*, pp. 3273–3284. Am. Soc. of Civ. Eng.

Kaergaard, K., Fredsoe, J. & Knudsen, S. B. 2011 Coastline undulations on the West Coast of Denemark: Offshore extent, relation to breaker bars and transported sediment volume. *Coastal Eng.* In press.

Kirby, J. T. & Dalrymple, R. A. 1994 Combined refraction/diffraction model REF/DIF1, Version 2.5. Res. Report CACR-94-22. Center for Applied Coastal Research, Univ. of Delaware.

Komar, P. D. 1998 *Beach Processes and Sedimentation*, 2nd edn. Englewood Cliffs, N.J.: Prentice Hall.

Larson, M. & Kraus, N. C. 1991 Mathematical modeling of the fate of beach fill. *Coastal Eng.* **16**, 83–114.

Leont'ev, I. O., Ryabchuk, D. V., Sergeev, A. Y. & Sukhacheva, L. L. 2011 On the genesis of some bottom and coastal features in the Eastern Gulf of Finland. *Oceanology* **51** (4), 688–698.

List, J. H. & Ashton, A. D. 2007 A circulation modeling approach for evaluating the conditions for shoreline instabilities. In *Coastal Sediments 2007*, pp. 327–340. Am. Soc. of Civ. Eng.

List, J. H., Benedet, L., Hanes, D. M. & Ruggiero, P 2008 Understanding differences between delft3d and emperical predictions of alongshore sediment transport gradients. In *Coastal Eng. 2008*, pp. 1864–1875. World Scientific.

List, J. H., Hanes, D. M. & Ruggiero, P. 2006 Predicting longshore gradients in alongshore transport: comparing the cerc formula to delft3d. In *Coastal Eng. 2006*, pp. 3370–3380. World Scientific.

Medellín, G., Falqués, A., Medina, R. & González, M. 2009 Sand waves on a low-energy beach at el 'puntal' spit, Spain: Linear Stability Analysis. *J. Geophys. Res.* **114** (C03022), doi:10.1029/2007JC004426.

Medellín, G., Medina, R., Falqués, A. & González, M. 2008 Coastline sand waves on a low energy beach at 'El Puntal' spit, Spain. *Mar. Geol.* **250**, 143–156.

Ozasa, H. & Brampton, A. H. 1980 Mathematical modelling of beaches backed by seawalls. *Coastal Eng.* **4**, 47–63.

Pelnard-Considère, R. 1956 Essai de theorie de l'evolution des formes de rivage en plages de sable et de galets. In *4th Journees de l'Hydraulique, Les Energies de la Mer, Paris*, , vol. III(1), pp. 289–298. Société Hydrotechnique de France.

Plant, N. G., Ruessink, B. G. & Wijnberg, K. M. 2001 Morphologic properties derived from a simple cross-shore sediment transport model. *J. Geophys. Res.* **106** (C1), 945–962.

Pringle, A. 1985 Holderness coast erosion and the significance of ords. *Earth Surface Processes and Landforms* **10**, 107–124.

Ruessink, B. G. & Jeuken, M. C. J. L. 2002 Dunefoot dynamics along the dutch coast. *Earth Surface Processes and Landforms* **27**, 1043–1056.

Ryabchuk, D., Leont'yev, I., Sergeev, A., Nesterova, E., Sukhacheva, L. & Zhamoida, V. 2011 The morphology of sand spits and the genesis of longshore sand waves on the coast of the eastern Gulf of Finland. *Baltica* **24** (1), 13–24.

Short, A. D. 1999 *Handbook of Beach and Shoreface Morphodynamics*. Chichester: Wiley.

Slott, J. M., Murray, A. B., Ashton, A. D. & Crowley, T. J. 2006 Coastline responses to changing storm patterns. *Geophys. Res. Lett.* **33** (18), L18404.

Smith, G. D. 1985 *Numerical Solution of Partial Differential Equations: Finite Difference methods*. Oxford, U.K.: Oxford Univ. Press.

Sonu, C. J. 1968 Collective movement of sediment in littoral environment. In *Coastal Eng. 1968*, pp. 373–400. Am. Soc. of Civ. Eng.

Soulsby, R. L. 1997 *Dynamics of Marine Sands*. London, U.K.: Thomas Telford.

Stewart, C. J. & Davidson-Arnott, R. G. D. 1988 Morphology, formation and migration of longshore sandwaves; Long Point, Lake Erie, Canada. *Mar. Geol.* **81**, 63–77.

Stive, M. J. F., Aarninkhof, S. G. J., Hamm, L., H., Hanson, Larson, M., Wijnberg, K. M., Nicholls, R. J. & Capobianco, M. 2002 Variability of shore and shoreline evolution. *Coastal Eng.* **47**, 211–235.

Thevenot, M. M. & Kraus, N. C. 1995 Longshore sandwaves at Southampton Beach, New York: observations and numerical simulation of their movement. *Mar. Geology* **126**, 249–269.

Uguccioni, L., Deigaard, R. & Fredsoe, J. 2006 Instability of a coastline with very oblique wave incidence. In *Coastal Eng. 2006*, pp. 3542–3553. World Scientific.

van den Berg, N., Falqués, A. & Ribas, F. 2011*a* Long-term evolution of nourished beaches under high angle wave conditions. *J. Marine Systems* **88**, 102–112.

van den Berg, N., Falqués, A. & Ribas, F. 2011*b* Modelling large scale shoreline sand waves under oblique wave incidence. *J. Geophys. Res.* Under review.

van den Berg, N., Falqués, A., Ribas, F. & Caballeria, M. 2011*c* On the wavelength of self-organized shoreline sand waves. *J. Geophys. Res.* Submitted.

van Enckevort, I. M. J., Ruessink, B. G., Coco, G., Suzuki, K., Turner, I L., Plant, N. G. & Holman, R. A. 2004 Observations of nearshore crescentic sandbars. *J. Geophys. Res.* **109** (C06028), doi:10.1029/2003JC002214.

Verhagen, H. J. 1989 Sand waves along the dutch coast. *Coastal Eng.* **13**, 129–147.

Wang, J. D. & LeMehaute, B. 1980 Criterion for stability of shoreline planform. In *Coastal Eng.*, pp. 1295–1305. Am. Soc. of Civ. Eng.

Wijnberg, K. M., Aarninkhof, S. G. F. & Spanhoff, R. 2006 Response of a shoreline sand wave to beach nourishment. In *Coastal Eng. 2006*, pp. 4205–4217. Am. Soc. of Civ. Eng.

Wilkinson, M. J., Blaha, J. E. & Noli, D. 1989 A new lagoon on the Namibian coast of South Africa: sand spit growth documented from sts-29 shuttle photography. *Geocarto International* **4**, 63–66.

Yoyoki, H., Larson, M. & Hanson, H. 2002 Rhythmic features along Sylt Island, Germany. *Tech. Rep.*. Water Resources Engineering, Lund Univ., Lund, Sweden.

Zenkovitch, V. P. 1959 On the genesis of cuspate spits along lagoon shores. *J. Geol.* **67**, 269–277.